BIOACTIVE PEPTIDE NANOFIBERS FOR BONE TISSUE REGENERATION

A DISSERTATION SUBMITTED TO

THE GRADUATE SCHOOL OF ENGINEERING AND SCIENCE

OF BILKENT UNIVERSITY

IN PARTIAL FULFILLMENT OF THE REQUIREMENTS FOR

THE DEGREE OF

DOCTOR OF PHILOSOPHY

IN

MATERIALS SCIENCE AND NANOTECHNOLOGY

By

GÜLİSTAN TANSIK

June 2017

BIOACTIVE PEPTIDE NANOFIBERS FOR BONE TISSUE REGENERATION

By Gülistan Tansık
June 2017

We certify that we have read this dissertation and that in our opinion it is fully adequate, in scope and in quality, as a dissertation for the degree of Doctor of Philosophy.

Ayşe Begüm Tekinay (Advisor)

Mustafa Özgür Güler (Co-advisor)

Çağdaş Devrim Son

Aykutlu Dana

Tamer Uyar

Ufuk Gündüz

Approved for the Graduate School of Engineering and Science:

Ezhan Karaşan

Director of the Graduate School

ABSTRACT

BIOACTIVE PEPTIDE NANOFIBERS FOR BONE TISSUE REGENERATION

Gülistan Tansık

Ph.D. in Materials Science and Nanotechnology

Advisor: Ayşe Begüm Tekinay

Co-Advisor: Mustafa Özgür Güler

June, 2017

Replacement and repair of bone tissue that is lost due to fractures, tumor resection, degenerative diseases and infections still remain major clinical challenges. Autografting, allografting and xenografting are the current strategies for the treatment of bone defects. However, these strategies cause problems such as immunological response and disease transmission in clinical applications. To overcome these limitations, regeneration of new bone can be induced by the use of synthetic bioactive materials. One of the most promising strategies is to develop synthetic scaffolds mimicking the functional components of the extracellular matrix (ECM).

Biomineralization is mineralization carried out by living organisms. Glycosaminoglycans have crucial roles in biomineralization and enhance the functions of growth factors involved in biomineralization. Success in bone regeneration studies requires a thorough understanding of the necessary conditions for triggering biomineralization during the bone tissue formation process. In this study, the effect of bioactive and biocompatible peptide nanofibers on osteogenic differentiation,

biomineralization and bone tissue regeneration are investigated under *in vitro* and *in vivo* conditions. In the first chapter, bone tissue composition, the clinical need for bone regeneration and general principles in bone tissue engineering are discussed. Bone tissue regeneration strategies are also highlighted in this part, with emphasis on peptide amphiphiles and self-assembly behavior. In the second chapter, a fully synthetic, extracellular matrix-mimetic peptide nanofiber system is described for enhancing the biomineralization and regeneration of bone tissue. This nanostructural environment forms artificial intracellular networks and supports biomineralization by providing cell-material and protein-material interactions. In the third chapter, effect of osteoinductive peptide nanofibers on osteogenic differentiation of rat mesenchymal stem cells (MSCs) were investigated. In the fourth chapter, the natural biomineralization process in bone tissue was mimicked on peptide nanofibers and the effect of this system on the osteogenic differentiation of osteoblast-like cells was investigated. In the fifth chapter, a dentin-mimetic peptide amphiphile (SpDSp-PA) molecule that is capable of emulating the structure and function of dentin phosphoprotein was designed and its capacity to support the deposition of hydroxyapatite and survival and biomineralization of osteoblast-like cells was evaluated.

Keywords: Bone regeneration, biomineralization, peptide amphiphiles, mesenchymal stem cell, extracellular matrix

ÖZET

BİYOAKTİF PEPTİT NANOFİBERLERİN KEMİK REJENERASYONU İÇİN KULLANILMASI

Gülistan Tansık

Malzeme Bilimi ve Nanoteknoloji, Doktora

Tez Danışmanı: Ayşe Begüm Tekinay

Tez Eşdanışmanı: Mustafa Özgür Güler

Haziran, 2017

Günümüzde kemik hastalıklarında, kırıklarda, enfeksiyonlarda veya tümorlü dokuların cerrahi olarak alınmasından sonra oluşan boşluklarda, kemik doku rejenerasyonunun ve tamirinin sağlanmasında klinik aşamada zorluklar yaşanmaktadır. Kemik hasarlarının tedavisinde allograft, otograft ya da xenograft kaynaklı yapıları kullanmak güncel tedavi yöntemleridir. Ancak, bu yapıların kullanılması immunolojik reaksiyonlara ya da hastalık bulaşmasına sebep olabilmektedir. Yeni sentetik biyomalzemelerin kemik doku hasarlarının rejenerasyonu amaçlı kullanılması ile bu sorunlar ortadan kaldırılabilir. Bu bağlamda, hücrelerin ekstraselüler matris yapısının fonksiyonel yapıları taklit edilerek hazırlanan sentetik iskelelerin kullanılması etkili bir tedavi yaklaşımı vadetmektedir. Biyomineralizasyon, canlı organizmaların gerçekleştirdiği mineralizasyon işlemidir. Glikozaminoglikanlarin biyomineralizasyonda da önemli olduğu ve biyomineralizasyonda görevli büyüme faktörlerinin işlevini arttırdığı bilinmektedir. Kemik doku oluşumu sürecinde biyomineralizasyonun tetiklenmesi için gerekli koşulların çalışılması kemik doku

yenilenmesi uygulamalarının başarısı için önemlidir. Bu tez çalışmasında, sentetik biyoaktif peptit nanofiberlerden oluşan yapay hücrelerarası iskelelerin osteojenik farklılaşmaya, biyomineralizasyona ve kemik rejenerasyonuna olan etkileri *in vitro* ve *in vivo* koşullarda incelenmiştir. İlk kısımda, kemik dokusunun yapısı, kemik rejenerasyonu gerektiren klinik vakalar ve kemik doku mühendisliğinin prensipleri hakkında bilgi verilmiştir. Ayrıca, kemik rejenerasyonu stratejilerinden bahsedilerek, peptit amfifil molekülleri ve kendiliğinden bir araya toplanma özellikleri üzerinde durulmuştur. İkinci kısımda, kemik doku oluşumunda biyomineralizasyonun biyomimetik malzemeler kullanılarak hızlandırılması hedeflenmiştir. Bu amaçla peptit nanofiberlerden oluşan, hücrelerarası matrisi taklit eden sentetik malzemeler kullanılmıştır. Bu nanoyapılardan oluşan ortam, yapay hücrelerarası yapıyı oluşturmuş ve hem malzeme-hücre hem de malzeme-protein etkileşimleri sağlayarak biyomineralizasyon mekanizmasına destek olmuştur. Üçüncü kısımda, osteoindüktif peptit amfifil nanoyapılar üzerindeki kök hücrelerin osteojenik farklılaşması araştırılmıştır. Bu kapsamda, peptit nanofiberler üzerinde kemik hücresine doğru farklılaşan mezenkimal kök hücrelerin belirli zamanlardaki osteojenik farklılaşması incelenmiştir. Dördüncü bölümde, kemik dokusunun doğal ortamında görülen biyomineralizasyon mekanizması sentetik peptit nanofiberler üzerinde taklit edilmiş ve bu sistemin osteoblast benzeri hücrelerin osteojenik farklılaşması üzerindeki etkileri incelenmiştir. Beşinci kısımda, dentin fosfoprotein yapısını ve fonksiyonunu taklit etmesi amacıyla dentin mimetik peptit amfifil molekülü (SpDSp-PA) tasarlanmıştır. Ayrıca, bu sistemin hidroksiapatit birikimi ve osteoblast benzeri hücrelerin biyomineralizasyon kapasiteleri üzerindeki etkileri incelenmiştir.

Anahtar kelimeler: Kemik rejenerasyonu, biyomineralizasyon, peptit amfifil, mezenkimal kök hücre, hücrelerarası iskele

Acknowledgement

I would like to express my deepest appreciation to my thesis advisors Prof. Ayşe Begüm Tekinay and Prof. Mustafa Özgür Güler for their scientific knowledge, guidance, encouragement and support throughout my PhD thesis studies. I would like to thank Prof. Aykutlu Dana for his scientific support during my studies. I would also like to acknowledge my jury members for their contributions to my thesis.

I would like to express my special thanks to Dr. Gulcihan Gulseren, Mustafa Beter, Ahmet Emin Topal and Egemen Deniz Eren for their fruitful collaboration.

I would like to acknowledge my previous and present lab and office members Dr. Hakan Ceylan, Melike Sever, Nuray Gündüz, Dr. Melis Şardan, Dr. Göksu Çınar, Aygül Zengin, Meryem Hatip, Dr. Büşra Mammadov, Dr. Ruslan Garifullin, Dr. M. Aref Khalily, Nurcan Haştar, İdil Uyan, Dr. Rashad Mammadov, Dr. Özlem Erol, Dr. Ashif Shaikh, Dr. Handan Acar, Dr. Aslı Çelebioğlu, Dr. Ayşe Özdemir, Özüm Şehnaz Günel, Ceren Garip Yaşa, Hatice Kübra Kara, Çağla Eren, Öncay Yaşa, Hepi Hari Susapto, Şehmus Tohumeken, Zeynep Orhan, İbrahim Çelik, Gökhan Günay, Seren Hamsici, Merve Şen, Canelif Yılmaz, Fatih Yergöz, Oğuz Tuncay, Burak Demircan, Dr. Zeynep Aytaç, Dr.Yelda Ertaş, Dr. Aydan Yeltik, Göksemin Fatma Şengül and Tuğçe Önür, for creating such a warm working environment. I would like to thank Alper Devrim Özkan for reading my thesis and suggesting corrections.

I would like to thank Mrs. Zeynep Erdoğan for her technical contribution to my thesis. I also thank to Suna Temiz who has always given me positive energy with her cheerful laughs.

I would like to acknowledge The Scientific and Technological Research Council of Turkey (TÜBİTAK BIDEB-2211C, 112T042 and 113S552) for funding my PhD research.

I would like to thank Mustafa Beter, Özge Uysal and Begüm Dikeçoğlu for their warm personality and good friendship. I am thankful to my dearest friends Dr. Berna Şentürk, Dr. Gülcihan Gülseren, Elif Arslan, Melis Göktaş, Yasin Tümtaş and Didem Mumcuoğlu. I enjoyed my time in UNAM with their worthy friendship. I would like to extend my special thanks to Burcu Özsoy and Canan Kurşungöz, who are always with me during those years.

My sincere thanks also goes to my special tangueras and tanguero; Ayşegül Hacısalihoğlu, Hıdır Askar, Mevlüde Tigel, Selen Berk, Gizem Altunok, Vildan Şener for all the fun we have had during the milongas and especially Dr. Aysel Kızıltay for her invaluable support during the period of thesis writing.

I am deeply grateful to Zeynep Aybaş Kavalcı and my aunt Suheyla Demirel for their love and support during my studies.

I would like to express my most sincere gratitude to my family, my mother Cahide Tansık and my super-brother Ali Erdem Tansık for their endless love, motivation and encouragement. I would not be where I am today without their help and support. Last but not least, I would like to express my most heartfelt thanks to my father for his love, care, support, motivation and unquestionable belief in me during his life. I dedicate this thesis to my beloved father, Mehmet Tansık.

Contents

List of Figures

List of Tables

Abbreviations

AFM	Atomic force microscopy
ALP	Alkaline phosphatase
ANOVA	Analysis of variance
BMP	Bone morphogenetic protein
BSA	Bovine serum albumin
CD	Circular dichroism
DCM	Dichloromethane
DIEA	*N*,*N*-diisopropylethylamine
DMEM	Dulbecco's modified Eagle's medium
DMF	N,N-Dimethylformamide
ECM	Extracellular matrix
ESI	Electrospray ionization
FBS	Fetal bovine serum
FGF	Fibroblast growth factor
Fmoc	9-Fluorenylmethoxycarbonyl
FTIR	Fourier transform infrared spectroscopy
GAG	Glycosaminoglycan
GAPDH	Glyceraldehyde 3-phosphate dehydrogenase
GF	Growth factor
HA	Hydroxyapatite
HBTU	*N*,*N*,*N*′,*N*′-Tetramethyl-O-(1*H*-benzotriazole-1-yl) uronium hexafluorophosphate
H&E	Hematoxylin and eosin
HPLC	High pressure liquid chromatography
IGF	Insulin-like growth factor
IM	Intramuscular
LC-MS	Liquid chromatography-mass spectroscopy
Micro-CT	Micro Computed Tomography
MSC	Mesenchymal stem cell
PA	Peptide amphiphile

PBS	Phosphate buffered saline
PDGF	Platelet-derived growth factor
rMSC	Rat mesenchymal stem cell
qRT-PCR	Quantitative real-time polymerase chain reaction
QTOF	Quadrapole time of flight
SD	Standard deviation
SEM	Standard error of mean
SEM	Scanning electron microscopy
TCP	Tissue culture plate
TEM	Transmission electron microscopy
TFA	Trifluoroacetic acid
TIS	Triisopropyl silane
TGF-β	Transforming growth factor-β
UV	Ultraviolet
VEGF	Vascular endothelial growth factor

Chapter 1

1. Introduction

1.1 Bone Tissue

Bone is a dynamic and highly vascularized tissue characterized by its rigidity, strength and ability to support the frame of the body [1, 2]. There are 206 different bones making up the skeleton, ranging from the long bones found in the limbs, short bones in the wrist and ankle, and flat bones in the sternum and skull, to irregular bones such as the pelvis and vertebrae [1]. The bones of the skeleton protect the vital organs, provide an environment for hematopoiesis within the marrow, serve as a reservoir of growth factors and cytokines, provide maintenance of acid-base balance and act as a mineral reservoir for calcium homeostasis [2]. Bone remodels throughout the lifetime of an individual by the removal of old, microdamaged bone and its replacement with new, mechanically stronger bone to help preserve bone strength [2, 3].

1.1.1 Hierarchical Structure of Bone

Bone has a hierarchical structure that includes macroscale, microscale, sub-microscale, nanoscale, and sub-nanoscale level organizations (Figure 1.1). The macroscale level of bone can be classified as compact bone (cortical bone) and trabecular bone (cancellous bone) [4]. The cortical bone is dense, solid, and surrounds the marrow space, while the trabecular bone is composed of a honeycomb-like network of trabecular plate rods interspersed in the bone marrow compartment [5]. Cortical bone is covered by an outer periosteal surface (periosteum), which is a fibrous connective tissue sheath surrounding the outer cortical surface of bone, except at the joints of long bones. The periosteum has an important role in fracture repair,

appositional growth, protection, nourishment and bone formation. It contains osteoblasts, osteoclasts, blood vessels and nerve fibers. Endosteum, the inner endosteal surface of the bone, is a membranous structure covering the inner surface of all bones and surrounds the blood vessel canals (Volkmann's canals) that are present in bone [5]. Cortical bone can have a thickness between several tenths of a millimetre to several millimetres or even centimetres [6].

Cancellous bone is supported by struts, the thickness of which is typically between 100 and 300 μm [6]. In this bone type, the most prominent structures seen at the nanoscale are mineralized collagen fibers with diameters of *c.* 100 nm [7]. The fundamental structural unit of fibrils consists of 300 nm-long and 1.5 nm-thick collagen molecules, which are deposited by osteoblasts into the extracellular space and then aggregate into fibrils through a self-assembling process. Adjacent collagen molecules are staggered in their long axis by 67 nm and generate a characteristic pattern of gap zones with 35 nm lengths and overlap zones with 32 nm lengths within the fibril [8]. Bone mineral crystals occur at regular intervals along the fibrils with an approximate repeat distance of 67 nm, corresponding to the distance by which adjacent collagen molecules are staggered [9].

1.1.2 Bone Cells

A balance between the activities of bone-forming osteoblasts and bone-resorbing osteoclasts is necessary to maintain the mature skeleton of mammals, including humans (Figure 1.2) [10].

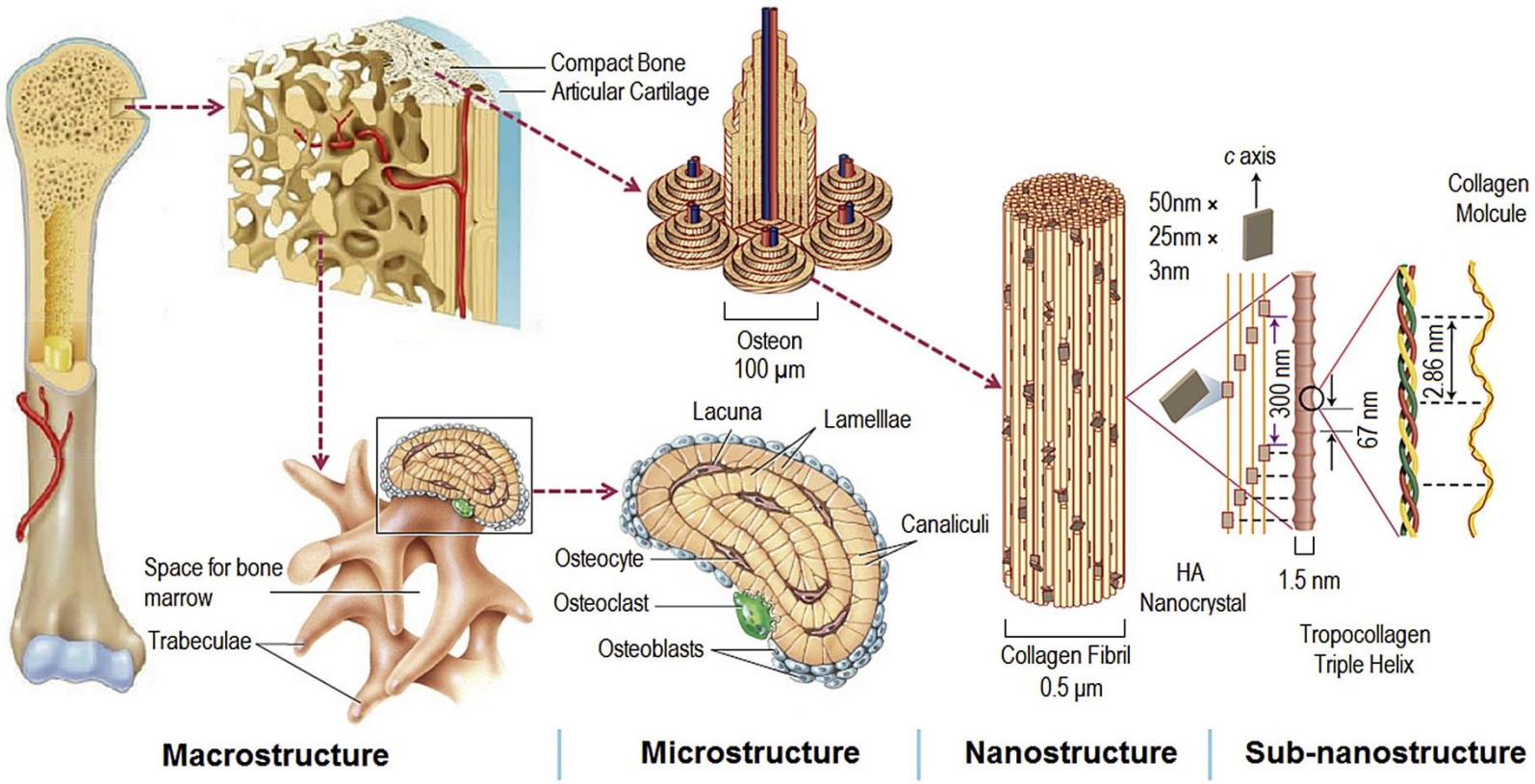

Figure 1.1 Hierarchical structural organization of bone. (Reproduced from Ref. 4 with permission from Elsevier Publishing Group)

1.1.2.1 Osteoblasts

Osteoblasts are the bone-making cells that produce a unique combination of extracellular proteins, such as osteocalcin, alkaline phosphatase and a large amount of type I collagen. When type I collagen is first deposited and but not yet mineralized, the extracellular matrix is described as osteoid. This preliminary arrangement can be subsequently mineralized through the accumulation of calcium phosphate in the form of hydroxyapatite. Osteoblasts are polarized cells with cellular membranes that are basally in direct contact with the bone surface, and extend a multitude of cytoplasmic processes into the newly deposited osteoid [11]. Osteoblasts possess a strongly basophilic cytoplasm, abundant mitochondria and a large Golgi apparatus, all of which enable these cells to produce large amounts of extracellular proteins [12].

The differentiation process of osteoblasts is divided into three stages, which are mesenchymal progenitors, preosteoblasts and osteoblasts. Osteoblasts are often characterized by the expression of osteocalcin; however, molecular markers for the mesenchymal progenitors are not very clear [10]. The “preosteoblast” moniker is applied to all cells transitioning from progenitors to mature osteoblasts. These cells are usually known to express the transcription factor runx2 or, at a more advanced stage of differentiation, both runx2 and osterix [10].

1.1.2.2 Osteocytes

A subset of osteoblasts can become osteocytes upon being entrapped within the bone matrix, while the remaining osteoblasts undergo apoptosis or become inactive bone-lining cells [13]. Osteocytes constitute 95% of cells in the mature bone tissue and function within syncytial networks in cooperation with each other, osteoblasts and/or

lining cells on the bone surface. Osteocytes are important regulators of bone remodelling in response to both mechanical and hormonal signals.

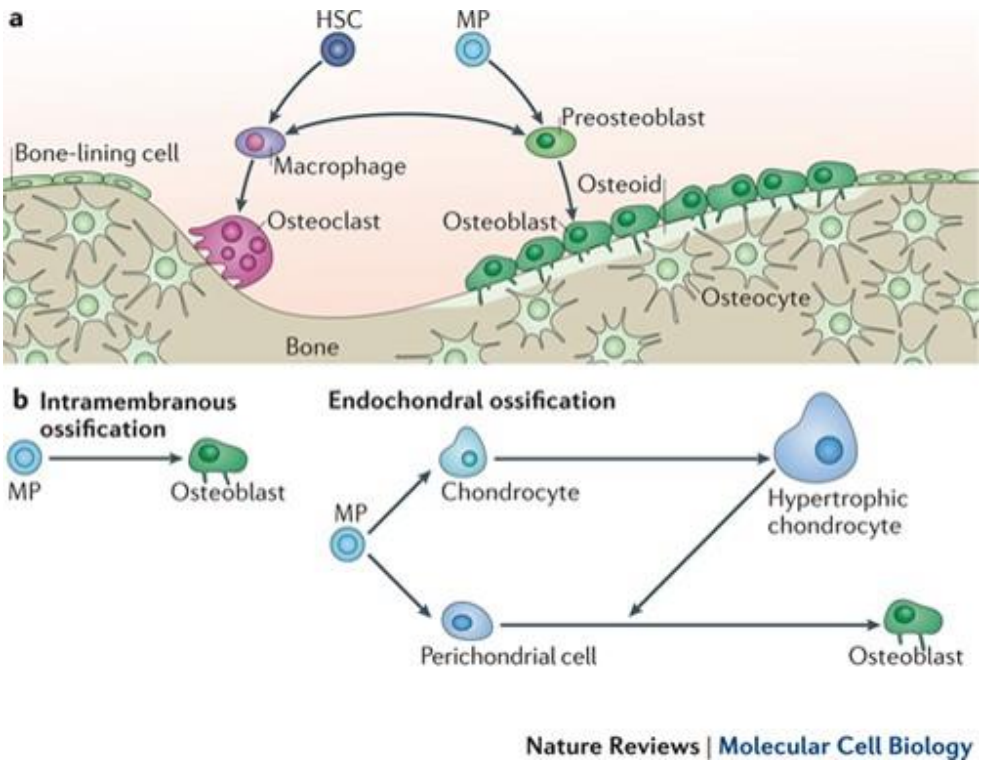

Figure 1.2 a) Bone homeostasis is achieved by osteoclasts (which are responsible for bone resorption) and osteoblasts (which are responsible for bone formation). b) Osteoblasts can differentiate from mesenchymal progenitors through two processes, intramembranous or endochondral ossification. (Adapted from Ref. 10 with permission from Nature Publishing Group)

1.1.2.3 Osteoclasts

Osteoclasts are multinucleated cells responsible for bone resorption (Figure 1.2) and are derived from mononuclear precursor cells of the monocyte/macrophage lineage [14]. Two cytokines are known to play crucial roles for osteoclast formation: RANKL

and macrophage CSF (M-CSF). These factors are produced mainly by marrow stromal cells and osteoblasts in membrane-bound and soluble forms [15]. The presence of stromal cells and osteoblasts in bone marrow is required for osteoclastogenesis [15]. RANKL belongs to the TNF superfamily and is critical for osteoclast formation. M-CSF functions in the proliferation, survival, and differentiation of osteoclast precursors, as well as osteoclast survival and the cytoskeletal rearrangements required for bone resorption [16].

1.1.3 Bone Extracellular Matrix

Cells of connective tissues are surrounded by an extracellular matrix (ECM), which is a dynamic network of molecules secreted by cells. ECM binds cells, acts as a scaffold for them, modulates their survival, development, shape and migratory behavior, and also serves as a reservoir for growth factors and cytokines (Figure 1.3) [17]. The organic phase of bone ECM consists of collagenous proteins (90%), mainly of type I collagen, and noncollagenous proteins including osteocalcin, osteonectin, osteopontin, fibronectin and bone sialoprotein II, bone morphogenetic proteins (BMPs), and growth factors [18, 19]. Hydroxyapatite crystals form the inorganic phase of bone ECM [18].

1.1.3.1 Bone Matrix Proteins

85 to 90% of the bone matrix is composed of collagenous proteins. The most abundant protein in bone matrix is type I collagen [20], in addition to trace amounts of type III, type V and Fibril-Associated Collagens with Interrupted Triple Helices (FACIT) collagens at certain stages of bone formation. FACIT collagens are a group of nonfibrillar collagens serving as molecular bridges that are important for the organization and stability of extracellular matrices. This protein family contains collagens IX, XII, XIV, XIX, XX, and XXI [21].

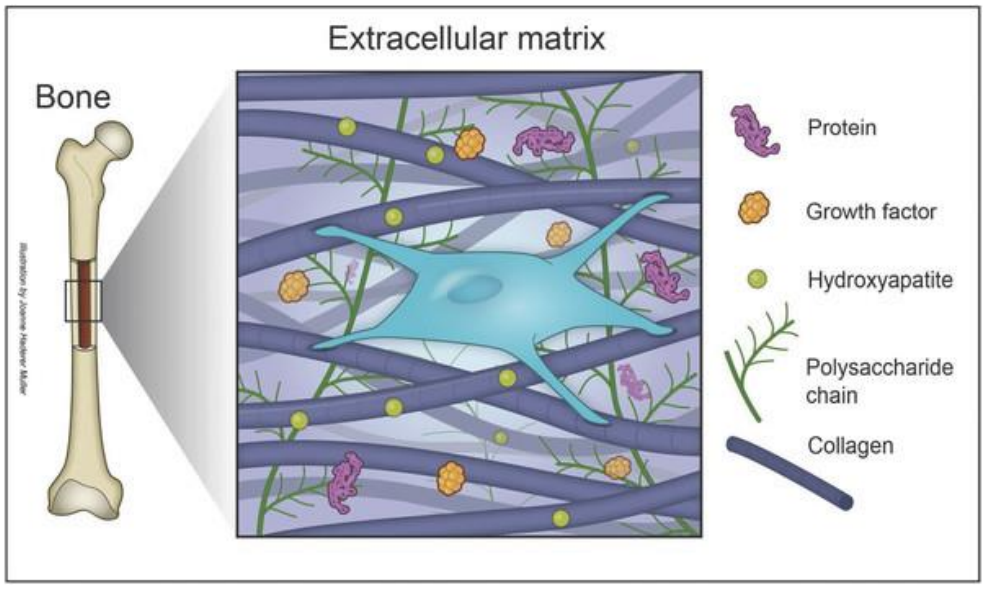

Figure 1.3 The extracellular matrix (ECM) of bone. (Adapted from Ref. 19 with permission from John Wiley and Sons Publishing Group)

Bone protein is composed of 10 to 15% noncollagenous proteins. During the last two decades, a number of noncollagenous proteins, such as osteocalcin, matrix gla-protein, osteonectin, osteopontin, and bone sialoprotein have been isolated from bone tissue and characterized [22-30]. The functions of each of the bone proteins are not well understood at present, and many seem to serve multiple functions such as regulation of bone mineral deposition and turnover and regulation of bone cell activity. For example, osteocalcin was previously shown to function as a promoter or initiator of calcium deposition, and therefore accepted as a marker of bone formation. On the other hand, it was also shown that osteocalcin knockout mice had a high bone mass phenotype, which suggests that osteocalcin normally inhibits bone formation. Osteocalcin is currently accepted as a marker of bone turnover rather than a specific marker of bone formation because serum osteocalcin is derived from both matrix release by osteoclast activity and osteoblast synthesis [21]. The main glycosylated

protein present in bone is alkaline phosphatase (ALP), which is bound to osteoblast surfaces by a phosphoinositol linkage and is also found free within the mineralized matrix. ALP hydrolyzes pyrophosphate and provides inorganic phosphate groups to promote mineralization [31]. The most abundant noncollagenous protein in bone is osteonectin, which accounts for approximately 2% of total protein in developing bone. It has roles in osteoblast growth and/or proliferation and matrix mineralization [21]. Osteopontin is involved in mineral deposition and growth, perhaps as an inhibitor [32, 33]. Bone sialoprotein has been thought to be involved in hydroxyapatite nucleation [32].

1.1.3.2 Glycosaminoglycans (GAGs) in Bone Tissue

Glycosaminoglycans (GAGs) have an essential role in tissue organisation through their interactions with a diverse range of proteins, growth factors and other chemokines. All GAGs are present in the body as proteoglycans, and are therefore covalently cross-linked to a protein core, except for the unsulfated hyaluronic acid and the highly sulfated heparin [34, 35].

PGs are categorized according to their sugar composition as keratan sulfate(s), chondroitin sulfate(s), dermatan sulfate(s), and heparan sulfate(s) (Figure 1.4) [35, 36]. Hyaluronic acid is not sulfated and not attached to a protein backbone [36-38]. Proteoglycans can also be classified according to their function and tissue distribution: aggrecan and versican, for example, are large secreted proteoglycans, while decorin and lumican are small leucine-rich proteoglycans, and perlecan is a basement membrane proteoglycan. In addition, syndecans are cell-surface-associated proteoglycans, whereas serglycin is an intracellular proteoglycan. The molecular

diversity of proteoglycans provides structural basis for a multitude of biological functions [37].

GAGs are linear polysaccharides composed of disaccharide repeat units, one of which is a hexuronic acid, glucuronic acid or iduronic acid, and the other is a hexosamine, N-acetylglucosamine (GlcNAc) or N-acetylgalactosamine [39]. Their biosynthesis is a complex nontemplate-driven process carried out by several enzymes that assemble the GAG polymer and then sulfate it at specific positions. Synthesis of heparan sulfates and chondroitin sulfates take place in the Golgi, where the individual GAG chains are *O*-linked to a core protein [40-42]. On the other hand, synthesis of keratan sulfate can involve either *N*-linking or *O*-linking to the core protein of the proteoglycan [40, 43]. Hyaluronic acid is not synthesized in the Golgi from the core protein, but instead requires an integral plasma membrane synthase, which secretes the nascent chain immediately [40, 44].

GAGs are highly negatively charged molecules, with extended conformations that provide high viscosity to the solution. These polysaccharides are located mainly on the surface of cells or in the ECM. The high viscosity of GAGs also results in low compressibility, which makes these molecules ideal for serving as lubricating fluid in the joints [45]. GAGs are present in an environment containing a variety of proteins, such as growth factors, cytokines, morphogens, and enzymes. Generally, they exert their biological activities through the localisation, stabilisation, activation or inactivation of interacting proteins [46]. GAGs play crucial roles in mediating the formation of protein complexes such as growth factor-receptor or enzyme-inhibitor associations on the cell surface and in the ECM. Cell signalling events are iniated or inhibited through a network of signals that are transduced through the formation of

ternary complexes of ligand, receptor, and proteoglycan. Thus, proteins and enzymes can be potentially sequestered by GAGs and presented to the appropriate site for activation [47]. GAGs can also function in maintaining morphogen gradients across a cell or tissue, which is crucial for a range of developmental processes [48]. Graded affinities between different GAG sequences and proteins may lead to the establishment and maintenance of a gradient in the concentration of growth factors or morphogens.

Alongside collagens, proteoglycans are the major constituents of the organic matrix of bone and play crucial roles in many bone processes, including the organization of the bone ECM and regulation of collagen fibrillogenesis. Proteoglycans also show selective patterns of reactivity with several constituents such as cytokines and growth factors, which modulates their bio-availability and biological activity in the bone tissue [49]. Different proteoglycan families are present in the bone matrix, including small leucine-rich proteoglycans (the most abundant), heparan sulphate proteoglycans, aggrecan and hyaluronic acid, all of which are responsible for exerting specific functions [49].

1.1.3.3 Growth Factors

The main growth factors affecting the functions of skeleton are bone morphogenetic proteins (BMPs), transforming growth factor-β (TGF-β), fibroblast growth factor (FGF), platelet-derived growth factor (PDGF), vascular endothelial growth factor (VEGF) and insulin-like growth factors (IGFs) (Table 1.1). In general, growth factors that are found embedded within the bone matrix or secreted by bone are considered to be major players during the bone repair process.

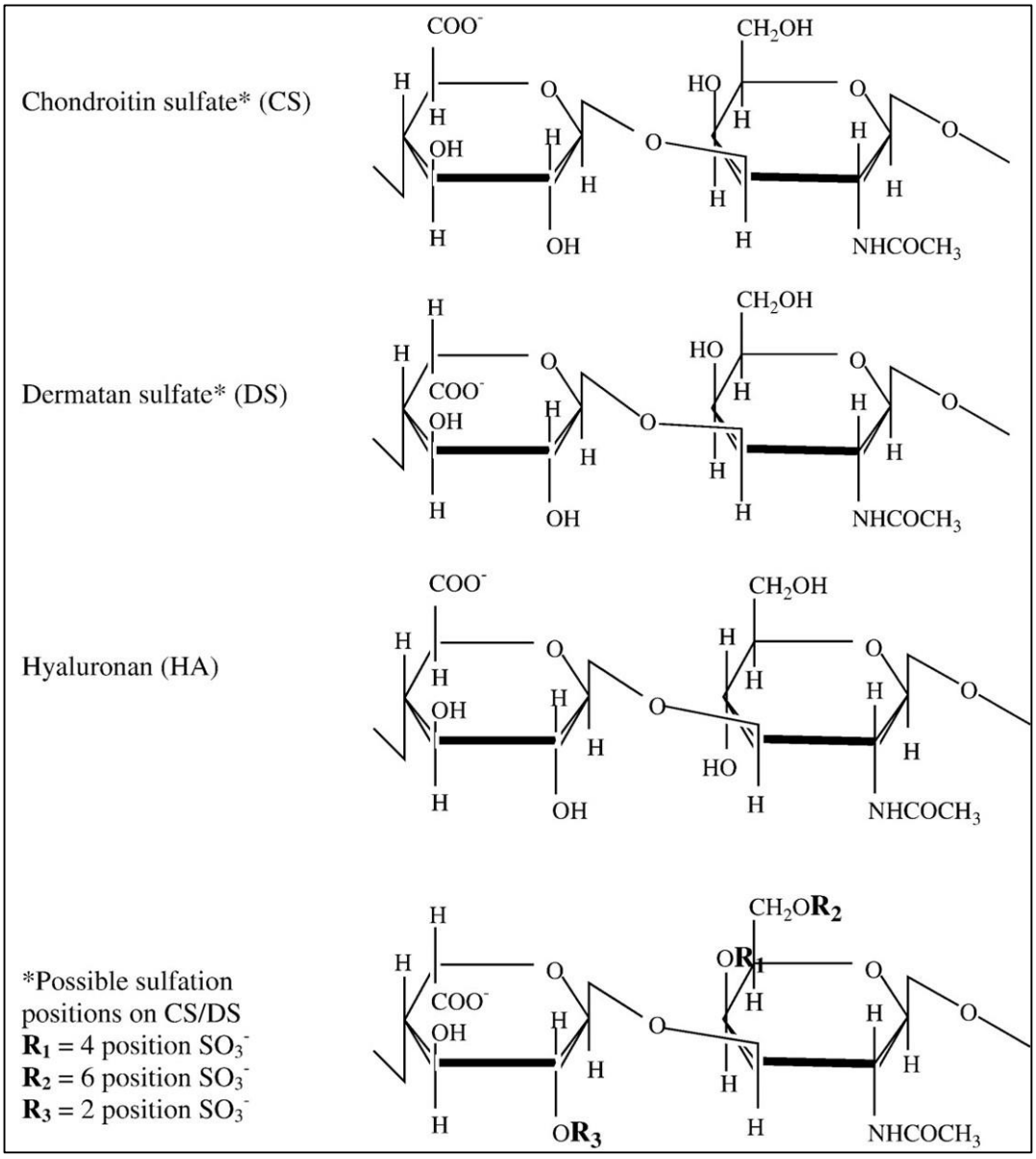

Figure 1.4 Repeating disaccharide units and possible sulfation positions of glycosaminoglycan chains. (Adapted from Ref. 35 with permission from Elsevier Publishing Group).

Immediately after bone injury, clot formation is observed and platelet α-granules release TGF-β, PDGF, VEGF and IGF [50]. FGF, PDGF and TGF-β are secreted by macrophages and other inflammatory cells subsequent to the inflammatory reaction. BMPs, PDGF, FGF and VEGF enhance the migration of osteoprogenitors, while PDGF and FGF stimulate the proliferation of periosteum-derived cells during the early stages of bone repair [51]. TGF-β, IGFs, BMP-6, BMP-2 and BMP-7 modulate the proliferation and differentiation of osteoprogenitor cells, whereas VEGF and FGF-2 regulate vascular ingrowth in the healing bone [50].

1.1.4 Bone Matrix Mineralization

Bone contains of 50 to 70% mineral, 20 to 40% organic matrix, 5 to 10% water, and 3% lipids. The mineral content of bone is mostly hydroxyapatite [$Ca_{10}(PO_4)_6(OH)_2$], with small amounts of carbonate, magnesium, and acid phosphate. In contrast to geological hydroxyapatite crystals, bone hydroxyapatite crystals are very small, measuring around 200 Å in their largest dimension. This small, poorly crystalline, carbonate-substituted structure makes these crystals more soluble than geologic hydroxyapatite crystals, which allow them to support the mineral metabolism [21]. Expression of ALP and several noncollagenous proteins such as osteocalcin, osteopontin, and bone sialoprotein mainly occurs during matrix maturation. It is assumed that the amount and size of hydroxyapatite crystals are regulated by these calcium- and phosphate-binding proteins [21].

The mechanical rigidity and load-bearing strength of bone are provided by bone minerals, while its elasticity and flexibility are derived from the organic matrix. Between the ends of collagen fibers, there are “hole” zones in which bone mineral is initially deposited [52].

Table 1.1 Main growth factors acting on bone repair. (Reproduced from Ref. 50 with permission from Springer Publishing Group).

GF	Cell source	Biological effect	Action on bone
BMP	Osteoprogenitor cell, osteoblast, Chondro-osteogenesis, Migration of osteoprogenitors, chondrocyte, endothelial cell (BMP-2)	Chondro-osteogenesis, osteoinduction (BMP-2)	Migration of osteoprogenitors, induction of proliferation, differentiation and matrix synthesis
FGF	Macrophage, monocyte, BMSC, chondrocyte, osteoblast, endothelial cell	Angiogenesis, proliferation of fibroblast, and smooth muscle cells of vessels	Chondrocyte maturation (FGF-1). Osteoblast proliferation and differentiation, inhibition of apoptosis of immature osteoblasts, induction of apoptosis of mature osteocytes, bone resorption (FGF-2)
IGF	Osteoblast, chondrocyte, hepatocyte, endothelial cell	Regulation of growth hormone effects	Osteoblast proliferation and bone matrix synthesis, bone resorption
PDGF	Platelet, osteoblast, endothelial cell, monocyte, macrophage	Proliferation of connective tissue cells, monocyte/macrophage and smooth muscle cell chemotaxis, Angiogenesis	Osteoprogenitor migration, proliferation and differentiation
TGF-β	Platelet, osteoblast, BMSC, chondrocyte, endothelial cell, fibroblast, macrophage	Immunosuppression, angiogenesis, stimulation of cell growth, differentiation and ECM synthesis	Undifferentiated mesenchymal cell proliferation, osteoblast precursor recruiting; osteoblast and chondrocyte differentiation (but inhibition of terminal differentiation), bone matrix production, recruitment of osteoclast precursors
VEGF	Osteoblast, platelet	Angiogenesis	Conversion of cartilage into bone, osteoblast proliferation and differentiation

Initiation of mineralization may be promoted by extracellular matrix vesicles in bone, as it is in calcifying cartilage and mineralizing tendon [53]. During this process, chondrocytes and osteoblasts synthesize matrix extracellular vesicles, which act as a protected microenvironment in which calcium and phosphate concentrations can increase sufficiently to precipitate crystal formation. Matrix extracellular vesicles have a nucleational core composed of proteins and a complex of acidic phospholipids, calcium, and inorganic phosphate, which is sufficient to precipitate hydroxyapatite crystals. As bone matures, hydroxyapatite crystals enlarge by crystal growth and aggregation and also reduce their level of impurities. By increasing local concentrations of calcium and/or phosphorus, bone matrix macromolecules may facilitate initial crystal nucleation. Dentin matrix protein 1 and bone sialoprotein are the main mineralization promoters. In addition, ALP also regulates the mineralization process by increasing local phosphorus concentrations, removing phosphate-containing inhibitors of hydroxyapatite crystal growth, or modifying phosphoproteins to control their ability to act as nucleators [21]. Vitamin D also indirectly stimulates the mineralization of unmineralized bone matrix. In fact, 1,25-dihydroxyvitamin D [1,25-(OH)2D] (which is produced by kidneys after absorption) and vitamin D (which is derived from precursors in skin) are responsible for maintaining serum calcium and phosphorus in adequate concentrations to allow the passive mineralization of unmineralized bone. Furthermore, serum 1,25-(OH)2D also promotes the differentiation of osteoblasts and stimulates osteoblast expression of bone-specific ALP, osteocalcin, osteonectin, OPG, and a variety of other cytokines [21].

1.1.5 Bone Formation

1.1.5.1 Intramembranous (Mesenchymal) Ossification

The direct conversion of mesenchymal tissue into bone is called intramembranous ossification, which is one of the two major modes of bone formation during the fetal development of the mammalian skeletal system. This process occurs mainly during the formation of the flat bones of the skull, but is also observed in the mandible, maxilla, and clavicles. In addition, intramembranous ossification is an essential process during the natural healing of bone fractures and the rudimentary formation of bones of the head. The steps in intramembranous ossification are the formation of an ossification center, calcification, formation of trabeculae and development of periosteum [5].

1.1.5.2 Intracartilaginous (Endochondral) Ossification

During endochondral ossification, cartilage tissue is formed by aggregated mesenchymal cells and this cartilage is later replaced by bone. Most bones in the body are ossified by this process, which is also responsible for mediating the vertical growth of long bones. The steps in endochondral ossification are the development of a cartilage model, growth of the cartilage model, development of the primary ossification center, development of the secondary ossification center, and the formation of articular cartilage and epiphyseal plate [5].

1.1.6 Clinical Need for Bone Regeneration

Bone does not function properly under disease states such as osteogenesis imperfecta, osteoarthritis, osteomyelitis, and osteoporosis. In addition to these diseases; traumatic injury, orthopedic surgeries and primary tumor resection may lead to bone defects or voids [54]. The large bone defects observed after these situations lack the template for an orchestrated regeneration and require surgical intervention [1]. Transplanting

autologous bone, in which the host bone is removed from another site (typically from the pelvis or iliac crest) and used to fill the defect, has been the gold standard for the treatment of bone defects. However, this method is limited by donor site morbidity, pain, paresthesia, prolonged hospitalization and rehabilitation, increased risk of deep infection, hematoma, inflammation, and restricted availability [55, 56]. The most commonly used alternative to bone autografts is the allografting of bone tissue from other humans (typically postmortem donations). Allografts may be provided from viable (alive) or sterilized non-viable sources, and have been approved by the FDA for many applications. However, allografts are also subject to immunological reactions and may possibly transmit infectious diseases [57, 58]. Patients requiring urgent bone repair or replacement may also consider a xenograft, which comes from nonhuman species [59]. Bone xenografts are now widely considered to be unsuitable for transplantation due to the risk of disease or virus transmission, infection, toxicity associated with sterilization, immunogenicity, and host rejection [60, 61].

1.1.7 General Principles in Bone Tissue Engineering

Because of the limitations of the current strategies for filling bone defects and subsequent repair, there is an expanding need for bone reconstruction that is paired with a growth of interest in the discipline of bone substitutes and tissue engineering [62]. The fundamental principle behind tissue engineering is the combination of engineering principles with the body's natural biological response to tissue damage, and a range of multifunctional bioactive scaffolds have been developed through this approach. Ideal synthetic scaffolds should present a physiochemical biomimetic environment, biodegrade as native tissue integrates, and actively promote or prevent desirable and undesirable physiological responses, respectively [63, 64]. To address

these biomimetic requirements, successful bone reconstruction must simultaneously promote osteoproduction, osteoinduction, osteoconduction, mechanical stimulation, and vascularization [62].

1.1.8 Bone Tissue Regeneration Strategies

Promising bone tissue engineering strategies such as cell transplantation, acellular scaffolds, gene therapy, stem cell therapy, and growth factor delivery have been applied to encourage the growth of new bone [65-68]. The majority of bone tissue engineering processes involve a combination of these strategies. However, implantation of cellular or acellular scaffolds have emerged as the most promising approaches.

Mesenchymal stem cells (MSCs) are pluripotent cells that are capable of differentiation into a number of cell types. Differentiation of MSCs can be driven towards bone-forming cells under the influence of chemicals such as dexamethasone, ascorbic acid, and β-glycerol phosphate. In many studies, it has been shown that transplanted scaffolds seeded with MSCs enhance osteogenic capacity [69-71].

In order to support the rapid development of a transplant-ready cellular scaffold, different novel *ex vivo* culture techniques have been investigated to accelerate the cellular production of ECM. Growth factor delivery, bioreactor systems, and gene therapy are the main *ex vivo* culture techniques used in bone tissue engineering.

Growth factors such as PDGF, BMP, IGF and TGF-β have important roles in osteoinduction and osteoconduction [50]. In *ex vivo* conditions, the delivery of growth factors can be performed by simply adding them to the culture media or encapsulating them in a biodegradable scaffold. However, since growth factors have short half-lives

and high doses are required for their delivery, alternative technologies are required for enhancing MSC performance in *in vivo* bone scaffolds [72].

Similar to growth factor delivery, gene delivery approaches aim to encourage native MSCs to migrate into the scaffold, proliferate, differentiate, and begin ECM production by increasing the local concentration of osteoinductive and osteoconductive cues for surrounding cells *in vivo*. Gene therapy strategies have been extensively tested and proven in animal studies, and hold great potential for the future of bone tissue engineering [73].

Bioreactor systems have also been designed to enhance the *in vitro* performance of osteogenic cells before implantation. The dynamic and mechanical 3D environments found in *in vivo* conditions are simulated by these bioreactors, which also provide cells with all the necessary nutrients and biological cues to survive, proliferate, differentiate, and produce ECM while embedded in a scaffold matrix [74, 75]. However, bioreactor systems are limited by the fact that MSCs cultured *ex vivo* lose their phenotypic behavior (such as osteodifferentiation and bone forming capacity) once implanted *in vivo.* In addition, MSCs are found in low concentrations in bone marrow and exhibit a low capacity for proliferation, which further complicates *ex vivo* culturing efforts [70, 76-78].

Implantation of an acellular scaffold immediately after injury or bone removal is the second main tissue engineering approach. It is more critical in this strategy to design a scaffold that mimicks the native bone tissue and recruits local MSCs into its matrix. Such a scaffold should also support and promote osteodifferentiation and provide a biodegradable matrix for enhancing ECM production for MSCs, allowing the material

to eventually reintegrate into the surrounding native tissue [66, 79-81]. This strategy is more advantegous than other repair approaches in that acellular scaffolds are much easier to sterilize, have longer shelf-lives, and exhibit little to no potential for infection or immunogenicity.

1.1.8.1 Biomaterials for Bone Repair

Advances in material design have led to the replacement of bio-inert scaffolds in tissue engineering with bioactive matrices that readily integrate with biological molecules or cells and regenerate tissues [64, 82]. In the case of bone, materials should preferably be capable of *osteoinduction* (promoting the differentiation of progenitor cells into an osteoblastic lineage), *osteoconduction* (supporting bone growth and encouraging the ingrowth of surrounding bone), and *osseointegration* (integrating into the surrounding bone).

1.1.8.2 Polymers

Polymers can be natural or synthetic. Natural biodegradable polymers such as type-I collagen, fibrin, hyaluronic acid and chitosan are interesting candidates for tissue engineering and exhibit good biocompatibility and osteoconductive properties. However, they have several shortcomings including very low mechanical stability, immunogenicity, the potential risk of disease transmission and sourcing and handling issues.

Biodegradable synthetic polymers, such as polyanhydrides, polypropylene fumarate, polycaprolactones, polyphosphazenes, polylactide, polyglycolide, and associated copolymers (polylactide-co-glycolide) offer a versatile alternative to their natural counterparts [83-85]. These polymers can be generated using techniques such as salt

leaching [86], gas foaming [87], phase separation [88-90], supercritical fluid processing [91], microsphere sintering, and three-dimensional printing [92] to generate a range of three-dimensional scaffolds with different porosities and surface characteristics. Different polymers possess different physical attributes, mechanical properties, degradation times, and modes of degradation. These different properties can be more or less preferable depending on the intended application of the matrix. For example, surface-eroding polymers like polyanhydrides are more suitable to deliver loaded factors and therapeutic substances than polymers that undergo bulk degradation, such as polylactide-coglycolide and polycaprolactone [62]. Poly(lactic acid) (PLA), poly(glycolic acid) (PGA) and poly(lactic-coglycolide) (PLGA) and their copolymers are well-known aliphatic polymer types that are frequently used in the field of bone tissue engineering. Most commonly used subtypes of these polymers are the D-PLA PDLA and L-PLA (PLLA) forms of PLA, and blends of D, L-PLA (PDLLA), PLA, PGA and PLGA. These variants are especially popular in bone fixation devices, sutures, drug carriers and bioregeneration scaffolds. Moreover, high molecular weight aliphatic polyesters, poly(L-lactide), PLA, and PCL are also utilized for similar regeneration applications [93].

Hydrogels such as polyethylene glycol or alginate-based scaffolds can be delivered in a minimally invasive manner and gelled *in situ* (e.g. photocrosslinked or ionically) to provide a three-dimensional cellular microenvironment with high water content.

Chemical biofunctionalization and cell encapsulation and delivery are relatively straightforward for hydrogels [94, 95]. Many of their applications in bone have also been explored [96-98].

1.1.8.3 Ceramics

A ceramic is a material made from an inorganic, non-metallic material. Ceramics typically have crystalline structures and possess a high compressive strength and low ductility, which provides them with high resistance to deformation but also imparts them with a tendency to fracture under stress. Calcium phosphates, calcium sulfates, and bioactive glass are typical ceramic matrices used for bone regeneration. Calcium phosphates are especially suitable for use as matrices, because the inorganic component of bone is composed of the ceramic calcium hydroxyapatite. Calcium phosphate and bioactive glass are also considered to be biomimetic, since they stimulate the formation, precipitation, and deposition of calcium phosphate from solutions, enhancing their bone-matrix interface strength [62].

1.1.8.4 Metals

Metallic scaffolds such as porous titanium or tantalum are the main class of biomaterials that are used in clinical settings. Porous metals exhibit a 3-dimensional interconnected pore structure, which is comparable to trabecular bone. In addition, titanium and tantalum are biocompatible, highly corrosion-resistant, durable and not biodegradable, with an elastic modulus very similar to that of the trabecular bone. Furthermore, they can be prepared in many different shapes and textures without affecting their biocompatibility. However, metals are naturally covered with an oxide layer that renders them highly bioinert and interferes with their integration to the surrounding tissue. Furthermore, titanium has higher stiffness compared to bone, which can cause problems associated with stress-shielding and subsequent implant loosening [62]. Nevertheless, metallic scaffolds are commonly employed to coat the

surface of the prosthetic implants to promote bone ingrowth and secondary implant stability [99, 100].

1.1.8.5 Composites

Composites are combinations of distinct material types that may exhibit a broad range of novel characteristics. As such, composites of well-established implant materials can be used to optimize their properties and increase their biointegration. For example, bioactive ceramics such as calcium phosphates have been combined with polymers to improve the mechanical properties of the latter. In addition, polymers are added to the ceramics to reduce their overall brittleness, increase their bioactivity and allow the controlled delivery of growth factors and therapeutic substances [62]. For example, after 4 weeks of implantation in a mouse calvarial defect, a mineralized PLGA polymer construct showed bone mineral growth, while nonmineralized scaffolds did not induce any mineralization [101]. Polymers can also form composite biomolecules: For example, PLLA mixed with collagen I and simulated body fluid closely mimicked the mineral-nucleating surface of bone [102].

1.1.8.6 Peptide Based Scaffolds

Ideal scaffolds for bone regeneration and biomineralization should meet rigid requirements in mechanical tolerance, biocompatibility, and biodegradability [103]. In bone regeneration strategies, inert and mechanically supportive metals and alloys have been widely used as bone implants. Although metallic implants and surface modification techniques are promising tools to accelerate the bone healing process, such surfaces lack the ability to attract osteogenic cells in the initial step of osseointegration. In order to induce adequate cell attachment and differentiation during bone repair, implant surfaces should be modified through biochemical methods, such

as the incorporation of growth factors or ECM proteins. Integrin recognition parts of bone matrix proteins such as collagen and fibronectin are short peptide sequences and their interaction with integrins and other surface receptors triggers critical downstream processes such as adhesion and signaling. Therefore, peptide amphiphiles (PAs) with short bioactive peptide sequences are promising candidates as scaffolds to induce bone tissue growth and biomineralization.

1.1.8.6.1 Peptide Amphiphiles

Peptide amphiphiles (PAs) are peptide-based molecules that self-assemble into high-aspect-ratio nanostructures under certain ranges of pH, temperature and ionic strength. These molecules consist of a hydrophobic alkyl tail or lipid chain, which is attached to a hydrophilic peptide sequence forming the PA head group [104-106]. The amphiphilic nature of the PAs allows them to present hydrophilic peptide signals on their surfaces, maximizing their presentation to cell receptors. Thus, PA systems are of great interest in many biomedical applications such as tissue engineering and regenerative medicine due to their highly bioactive nanostructures [107].

In aqueous solutions, the aggregation of hydrophobic tails drives self-assembly and results in the presentation of bioactive peptides on the surface of the nanostructure [104, 108-110]. The hydrophobic alkyl chains are screened from the aqueous environment, precipitating the aggregation of PA molecules [106, 111]. Briefly, hydrophobic interactions of the alkyl tails, hydrogen bonding among the middle peptide segments, and electrostatic repulsions between the charged amino acids elicit the forces that direct the self-assembly of PAs in water. Hydrophobic interactions and hydrogen bonding are attractive forces that induce the aggregation of PA molecules, while electrostatic repulsions from the charged components promote the disassociation

of PA molecules [107]. The peptide epitope usually has a biologically derived motif playing an important role in biological processes such as signal transduction, cell adhesion in the ECM, proliferation and cell mobility [106, 110, 112].

In general, bioactive short peptides are cell-binding epitopes such as RGDS, IKVAV and YIGSR. Among them, the RGDS sequence is typically used to direct cell attachment. The RGD motif is found in fibronectin, osteopontin and sialoprotein [113, 114]. In the literature, it has been shown that bone marrow derived stem cells adhere on RGDS-containing peptide amphiphile (PA) surfaces and, when these stem cells were encapsulated into PAs and the coassembled system was injected *in vivo*, RGDS-containing PA gels promoted cell viability significantly better than the epitope-free control group [115].

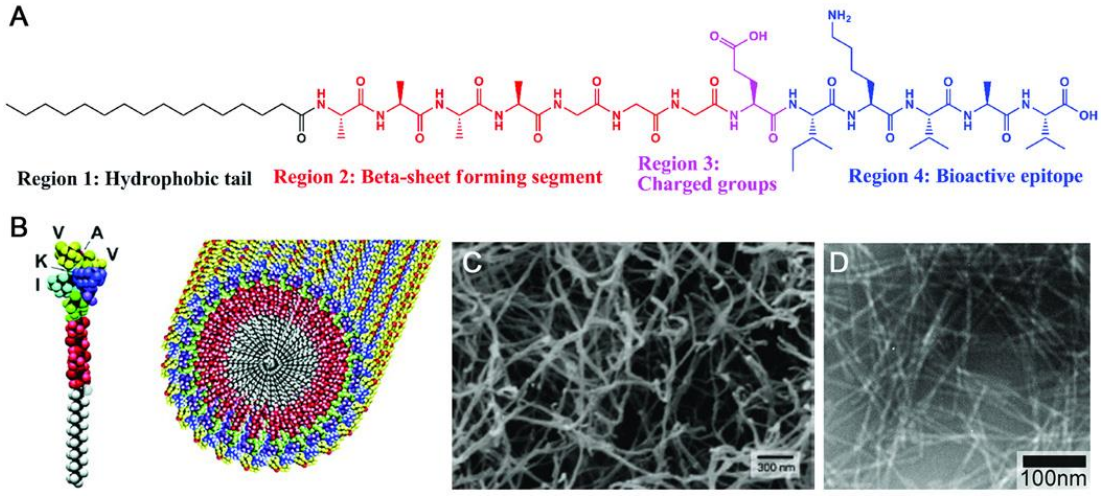

Figure 1.5 Structure of a representative PA. (Adapted from Ref. 107 with permission from John Wiley and Sons Publishing Group)

Bioactive short peptide sequences derived from collagen I, which is the primary component of bone, are potential targets for induction of bone tissue remodeling. DGEA is the best-studied collagen I epitope and it is found in the α1 helix of collagen. Osteoinductive characteristics of DGEA have been used intensively for bone regeneration studies. For instance, DGEA peptide-coated hydroxyapatite surfaces enhanced the differentiation of MSCs into osteogenic lineage [116]. However, in some cases bioactivity alone is not enough for adequate regeneration, and more than one PA component may be required for optimal results. For instance, it was shown that CGGDGEAG sequence cannot mediate the adhesion of rat calvarial osteoblasts onto peptide surfaces [117]. In order to eliminate this problem and enhance osteoinductive potential of DGEA-PA; RGDS-PA, and S-PA peptides were used with different combinations. Histochemical staining and gene expression results showed that the RGDS-PA/DGEA-PA combination strongly upregulated osteogenic differentiation [118]. Peptide sequences can be also used as growth factor binding units on gel scaffolds for attracting growth factors to a desired location. Bone morphogenetic protein-2 (BMP-2), which is a well-known bone differentiation regulation factor, has significant roles during osteogenesis and was targeted for this purpose. In the literature, it was shown that BMP receptor-binding peptides with osteopromotive domains, DWIVA and A_4G_3EDWIVA, were adequate for maintaining bone regeneration process [119]. In the ECM, BMP-2 can also interact with glycosaminoglycans (GAGs) and sulfated GAG mimetic peptide-BMP interaction was utilized for the promotion of osteoblast maturation and mineralization of osteogenic cells. In a study by Webber *et al*., osteogenic activity and mineralization of osteoblastic cells were promoted by the

GAG-mimicking ability of the peptide nanofibers and their interaction with BMP-2 [120].

Another peptide sequence used to enhance tissue regeneration is RADA16-I. Horii *et al*. reported that RADA16-I could be linked to variable bioactive signal inducing short peptides such as ALK (ALKRQGRTLYGF) osteogenic growth motif, DGR (DGRGDSVAYG) osteopontin based cell adhesion sequence and PGR (PRGDSGYRGDS) two repeat RGD adhesion sequence to enhance osteogenic differentiation and support [121]. In addition, it was shown that KRSR, a peptide sequence found in the heparin-binding proteins of the ECM, promotes the selective adhesion of osteoblasts while inhibiting the adhesion of fibroblasts [122, 123]. Furthermore, when a titanium alloy (Ti6Al4V) surface was functionalized with KRSR-PA and DOPA-conjugated PA, the combination of these two biomimetic sequences effectively induced osteogenic differentiation [124].

Chapter 2

2. Bone Regeneration Through Induction of Biomineralization by Glycosaminoglycan Mimetic Peptide Nanofiber Gel

This chapter of thesis was published in the following article [125]; Reproduced from "A glycosaminoglycan mimetic peptide nanofiber gel as an osteoinductive scaffold"*;* Tansik, G.; Kilic, E.; Beter, M.; Demiralp, B.; Şendur Kızıltas, G.; Can, N; Ozkan, H; Ergul, E; Guler, M. O.; Tekinay, A. B., *Biomaterials Science,* 2016, 4, 1328 - 1339, with permission from the Royal Society of Chemistry.

2.1 Introduction

Bone tissue defects can occur as a result of trauma, organic bone diseases, infectious diseases, and surgeries. The treatment of bone defects is a major reconstructive challenge in the field of orthopedics [126]. While the gold standard of clinical care is the autograft, the use of autografts, xenografts and allografts is limited due to their lack of availability, the risk of infections, donor site morbidity, and the potential of transplant rejection [127]. These problems can be overcome by using scaffolds made of synthetic or natural biomaterials promoting the migration, proliferation, and differentiation of bone cells [64, 128]. Advances in nanotechnology and tissue engineering offer promising options for the regeneration and replacement of damaged bone [129].

Supramolecular peptide nanofiber systems are used as synthetic scaffolds in regenerative medicine applications because of their tailorable properties and ability to mimic ECM proteins [130-133]. Peptide nanofibers are attractive for regeneration of bone defects, because bone is a composite consisting of a protein-based soft template (*i.e.*, a mixture of collagen, non-collagenous proteins (laminin, fibronectin, vitronectin) and water) and hard inorganic components (hydroxyapatite (HA), $Ca_{10}(PO_4)_6(OH)_2$) [134, 135]. The 70% of the bone inorganic matrix is composed of HA crystals, which are typically 30 – 50 nm long and 1.5 – 4 nm thick [136]. Other protein components in the bone ECM are also in the nanometer scale, and the adhesion, proliferation and differentiation of resident mesenchymal stem cells (MSCs), osteoblasts, osteoclasts and fibroblasts are known to be affected by this self-assembled nanostructured ECM. Bone tissue contains less than 1% glycosaminoglycans (GAGs) [137, 138] consisting of about 90% chondroitin-4-sulfate and small amounts of hyaluronic acid, chondroitin-6-sulfate, and dermatan sulfate [139]. GAGs have significant regulatory roles in the development and regeneration of bone tissue. They exhibit complex effects on the behavior of bone cells at all stages of their differentiation, and facilitate the attraction and adhesion of precursor cells, their subsequent differentiation and their interactions with other proteins [140]. Sulfated GAGs, which are rich in negatively charged sulfate groups, are important for bone formation due to their ability to interact with growth factors such as FGF, BMPs, TGF-β1 and IGF-II, which are involved in regulating the osteoblastic cells. Sulfated GAGs work by binding to the positively charged amino groups of various proteins and growth factors, thus increasing their local availability [141, 142].

GAG mimetic peptide nanofibers were previously shown to interact with several growth factors, including vascular endothelial growth factor (VEGF), fibroblast growth factor-2 (FGF-2) and hepatocyte growth factor (HGF) [143]. In addition, it was demonstrated that glycosaminoglycan mimetic peptide nanofibers are able to interact with bone morphogenetic protein-2 (BMP-2), which is a critical growth factor for osteogenic activity [144]. The GAG mimicking ability of the peptide nanofibers and their interaction with BMP-2 promoted osteogenic activity and mineralization by osteoblastic cells [144]. Since MSCs have self-renewing capabilities and multi-lineage differentiation potential [145], there is currently a strong need for the fabrication of a biomaterial scaffold that is able to support and direct these cells towards the osteoblastic lineage. In this part of the thesis, GAG-mimetic peptide nanofibers were shown to provide a suitable microenvironment for the osteogenic differentiation of rat mesenchymal stem cells (rMSCs). It was also demonstrated that these nanofibers enhance bone regeneration and biomineralization in a rabbit tibial bone defect model (Figure 2.1).

2.2 Experimental Section

2.2.1 Materials

4-(2′,4′-dimethoxyphenyl-Fmoc-aminomethyl)-phenoxyacetamido-norleucyl-MBHA resin (Rink amide MBHA resin), Fmoc-Asp(OtBu)-Wang resin, all protected amino acids, lauric acid, 2-(1H-benzotriazol-1-yl)-1,1,3,3-tetramethyluroniumhexafluorophosphate (HBTU), and diisopropylethylamine (DIEA) were purchased from Nova-Biochem, ABCR, or Sigma-Aldrich. Calcein-AM and other cell culture materials were purchased from Invitrogen. All other chemicals and materials used in this study were purchased from Thermo Scientific or Sigma-Aldrich.

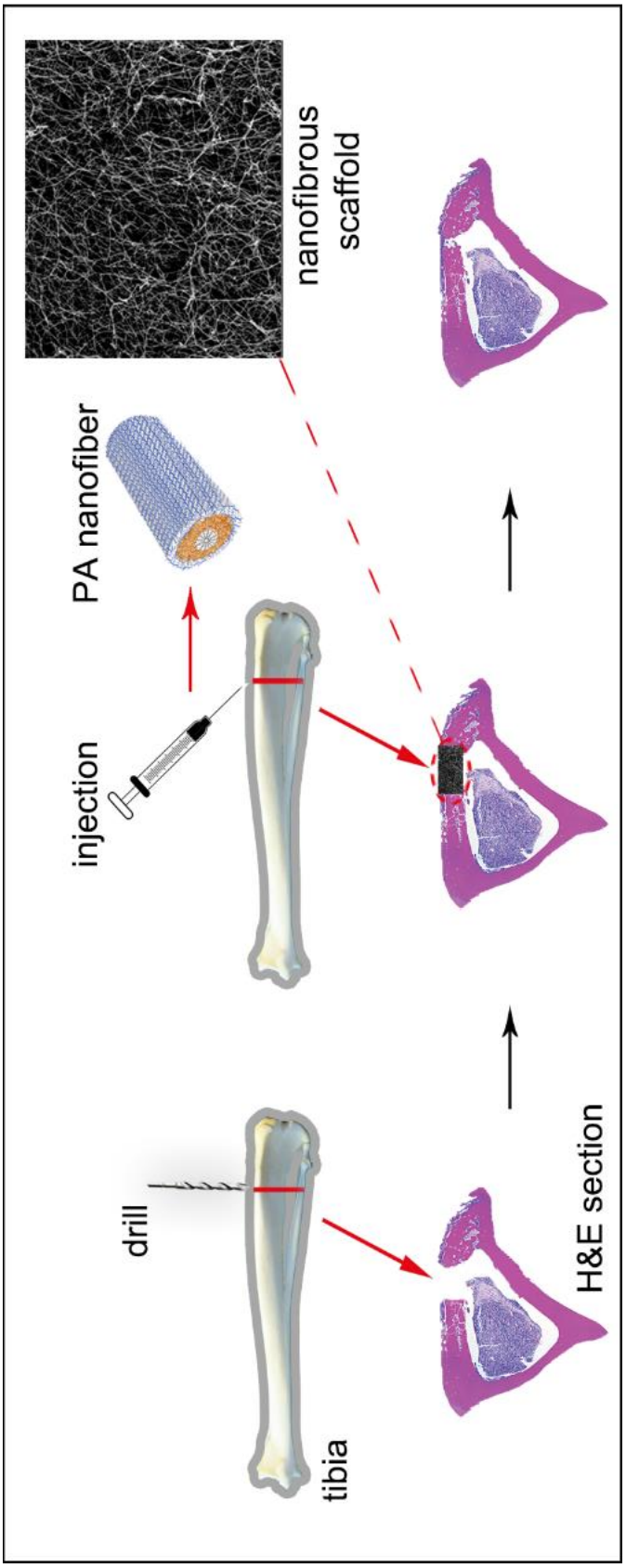

Figure 2.1 Schematic representation of the rabbit tibia bone tissue regeneration model.

2.2.2 Synthesis of Peptide Amphiphile (PA) Molecules

Fmoc solid phase peptide synthesis method was used to synthesize Lauryl-Val-Val-Ala-Gly-Lys-Am (K-PA), Lauryl-Val-Val-Ala-Gly-Glu (E-PA), and Lauryl-Val-Val-Ala-Gly-Glu-Gly-Asp (Lys-p-sulfobenzoate)-Ser-Am (GAG-PA). Rink amide MBHA resin (Novabiochem) was used as the solid support for K-PA and GAG-PA, while Fmoc-Glu(OtBu)-Wang resin (100-200 mesh) served as solid support for E-PA. Amino acid couplings were carried out with 2 molar equivalents of Fmoc protected amino acid, 1.95 molar equivalents of HBTU, and 3 molar equivalents of DIEA for 3 h. The removal of the Fmoc protecting group on the N^{α}-amino group of the peptide was performed with addition of 20% piperidine in dimethylformamide (DMF) solution for 20 min. In order to block the remaining free amine groups after amino acid coupling, 10% acetic anhydride in DMF solution was used. The resin was washed by using DMF and dichloromethane (DCM) after each step. To synthesize GAG-PA, a p-sulfobenzoic acid residue was added to the side-chain of lysine. A lysine residue with 4-methytrityl (Mtt) side-chain protecting group was used for selective deprotection of amine groups. In order to remove Mtt, resin was shaked for 5 min with trifluoroacetic acid (TFA):triisopropylsilane (TIS):H_2O:DCM at a ratio of 5:2.5:2.5:90. The cleavage of PAs and protecting groups from the resin was carried out with a mixture of TFA:TIS:H_2O at a ratio of 95:2.5:2.5 for 2.5 h. Excess TFA was removed by rotary evaporation, and PAs were precipitated using ice-cold diethyl ether at −20 °C overnight. The precipitate was then collected by centrifugation, dissolved in ultrapure water and frozen at −80 °C overnight. The frozen samples were lyophilized for 4 days. The identity and purity of peptide amphiphiles were assessed by LC-MS (Agilent 6530−1200 Q-TOF) analysis.

Mass spectra were obtained with an Agilent LC-MS equipped with Agilent 6530 Q-TOF with an ESI source and Zorbax Extend-C18 2.1 mm × 50 mm column for basic conditions and Zorbax SB-C8 4.6 mm × 100 mm column for acidic conditions. A gradient of water (0.1% formic acid or 0.1% NH_4OH) and acetonitrile (0.1% formic acid or 0.1% NH_4OH) was used as the mobile phase. To purify the peptides, an Agilent preparative reverse-phase HPLC system equipped with Zorbax Extend-C18 21.2 mm × 150 mm column was used for basic conditions, and Zorbax SB-C8 21.2 mm × 150 mm column was used for acidic conditions. A gradient of water (0.1% TFA or 0.1% NH_4OH) and acetonitrile (0.1% TFA or 0.1% NH_4OH) was used as the mobile phase. Positively charged PAs were treated with 0.1 M HCl solution and lyophilized to remove residual TFA.

2.2.3 Scanning Electron Microscope (SEM) Imaging of PA Nanofiber Networks

SEM was used to observe the nanofiber networks formed by PAs. Samples were prepared on silicon wafer by mixing oppositely charged PA solutions (10 mM) in a final volume of 60 µL. Briefly, GAG-PA and E-PA were mixed with K-PA at 1:3, and 1:2 ratios to stabilize all net charges. 15 min after gelation occurs, samples were dehydrated by sequential treatment with 20%, 40%, 60%, 80% and 100% v/v ethanol. After ethanol gradient exchange, critical-point drying was performed by using Autosamdri-815B critical point dryer (Tousimis). The dried samples were coated with 4 nm Au-Pd before imaging and images were taken by using FEI Quanta 200 FEG scanning electron microscope at high vacuum mode with 5 keV beam energy.

2.2.4 Circular Dichroism (CD)

CD samples were prepared by using 3 x 10^{-2} mM GAG-PA / 9 x 10^{-2} mM K-PA and 3 x 10^{-2} mM E-PA / 6 x 10^{-2} mM K-PA mixtures, respectively. JASCO J815 CD spectrometer was used at room temperature. CD spectra of peptide solutions were measured in a range of 300 nm to 190 nm, with a data interval and data pitch of 0.1 nm, a scanning speed of 100 nm min^{-1}, and all measurements representing three accumulations. Digital Integration Time (DIT) was selected as 1 s, band width as 1 nm, and the sensitivity was as standard.

2.2.5 Fourier Transform Infrared (FT-IR) Spectroscopy

FT-IR spectroscopy was used to obtain information about the secondary structures of PAs. Briefly, 10 mM gels formed on Petri dishes were frozen in liquid nitrogen and kept at -80 °C overnight. Following the freeze drying process, dried samples were used to form pellets with KBr (100 mg KBr/1 mg dried sample) and absorbance analysis was performed with a Bruker VERTEX 70 FT-IR Spectrometer in 4000-400 cm^{-1} range.

2.2.6 Cell Culture and Maintenance

The rMSCs (Invitrogen, passage number 7) were used in all cell culture experiments, including viability, calcium deposition and gene expression analyses. Cells were cultured in 75 cm^2 flasks at a density of 3×10^3 cells per cm^2 at 37 °C in a humidified incubator and supplied with 5% CO_2. The rMSCs were maintained in DMEM (low glucose) with L-glutamine supplemented with 10% fetal bovine serum (FBS) and 1% penicillin/streptomycin. All cell culture experiments were carried out after the cells reached 90% confluency. The culture medium was changed every 3–4 days. Cells were

seeded under the same conditions used for their maintenance. For mineralization experiment and gene expression analysis, the seeded cell medium was replaced with osteogenic medium (DMEM with 10% FBS supplemented with 10 mM β-glycerophosphate, 50 μg mL^{-1} ascorbic acid and 10 nM dexamethasone) after reaching confluency.

2.2.7 Tissue Culture Plate Coating

Tissue culture plate surfaces were coated with peptides at a concentration of 1 mM. To neutralize charges, GAG-PA and E-PA were mixed with K-PA at 1:3 and 1:2 volume ratios, respectively. After coating, plates were placed in a fume hood overnight for drying, and sterilized with UV light for 1 h prior to cell culture experiments.

2.2.8 Viability Assay

The viability of rMSCs incubated on PA coated and uncoated tissue culture plates (TCP) was studied by Live/Dead Assay (Invitrogen). Briefly, cells were seeded on PA-coated and uncoated 96-well tissue culture plates at a density of 5 x 10^3 cells/well. After 12, 24, 48, and 72 h of incubation, cell medium was discarded; cells were washed with phosphate buffered saline (PBS) and then incubated with 2 μM calcein-AM and 2 μM EthD-1 in PBS for 30 min at room temperature. After incubation, images were taken at three random points per well with a fluorescent microscope (Zeiss, Axio Scope A1) at 10x magnification. All samples were analyzed in triplicate. Live and dead cells were counted by using Image J and the number of live cells was calculated for each sample.

2.2.9 Actin Staining of rMSCs on PA Nanofiber Coated Surfaces

Glass coverslips were coated with PAs, and cells were seeded on top of the coated and uncoated surfaces at a density of 3×10^3 cells/cm^2. At predetermined culture durations, cells were fixed with 4% formaldehyde for 15 min and permeabilized with 0.1% Triton-X for 10 min at room temperature. Samples were incubated with 3% (w/v) bovine serum albumin (BSA)/PBS for blocking for 30 min. Actin filaments of the cells were initially stained with 1:500 diluted FITC-conjugated phalloidin (Thermo Fisher) in 3% (w/v) BSA/PBS for 20 min.

After serial washing steps, samples were stained with 1:1000 diluted TO-PRO-3 (Thermo Fisher) in PBS for 20 min for the visualization of nuclei. Coverslips were mounted with Prolong Gold Antifade Reagent (Invitrogen). Cytoskeletal organization of cells was observed using a Zeiss LSM 510 confocal microscope. Images were taken at 20x magnifications.

2.2.10 SEM Imaging of rMSCs on PA Nanofiber Coated Surfaces

The morphology and spreading of mesenchymal stem cells were examined by SEM imaging by using an ETD detector at high vacuum mode at 5 keV beam energy. For this purpose, glass coverslips were coated with PAs, and cells were seeded on top of the coated and uncoated surfaces at a density of 3×10^3 cells/cm^2. Three and fourteen days after incubation, cells were rinsed with PBS and fixed with 2% gluteraldehyde/PBS and 1 wt % OsO_4 for 1 h each, respectively. Fixed cells were washed with water and then dehydrated sequentially in 20%, 40%, 60%, 80%, and 100% ethanol. Samples were critical point dried with Autosamdri-815B Tousimis and coated with 5 nm Au−Pd before imaging.

2.2.11 Alkaline Phosphatase (ALP) Activity Assay

In order to measure the ALP activity of rMSCs, degradation of *p*-nitrophenol due to endogenous ALP activity was quantified after 7 and 14 days of culture in osteogenic medium. Briefly, cells were seeded on PA nanofiber-coated and uncoated TCP surfaces at a density of 3 x 10^3 cells per cm^2 and the cell medium was replaced with osteogenic medium after cells reached confluency. Cells were rinsed with PBS at predetermined time points. M-PER protein extraction kit (Thermo) with 5% protease inhibitor solution was used to extract the proteins. Supernatants containing the protein fraction were removed after centrifugation at 14,000 g for 10 min.

Pierce BCA protein assay (Thermo) was performed to quantify the amount of protein obtained from the cells as described in the manufacturer's protocol. To measure ALP activity, 50 µL of the protein sample was incubated with 150 µL of *p*-nitrophenol phosphate substrate in 96-well plates for 30 min on a shaker. Serial dilutions of *p*-nitrophenol in 0.25 M NaOH solution were used as standards. Finally, the optical density of the samples was determined at 405 nm using a Spectramax M5 microplate reader and ALP results were normalized to the total amount of protein at each time point tested.

2.2.12 Detection of Mineralization by Alizarin Red Staining

Calcium deposition on the surface of hydrogels was measured on days 14 and 28 using Alizarin red staining. Briefly, rMSCs were seeded on PA coated and bare tissue culture plates at a density of 3 x 10^3 cells per cm^2 in DMEM medium containing 10% FBS and 1% penicilin-streptomycin. Cells were cultured in this medium until they reached confluency, and the medium was then replaced with fresh osteogenic medium. This medium was replenished every 3–4 days over the course of experiments. At

predetermined time intervals, cells were fixed with ice-cold ethanol for 1 h and stained with 40 mM Alizarin-red S for 30 min on a shaker. Afterwards, samples were washed 4-5 times with double distilled water to get rid of non-specific Alizarin-red binding. Calcium nodules were imaged in PBS under light microscopy. In order to quantify deposited calcium, PBS was discarded and the samples were incubated in 10% cetylpyridinium chloride for 30 min at room temperature. At the end of the incubation period, the solution was transferred to 96-well plates and absorbance measurements were performed at 562 nm.

2.2.13 Gene Expression Analysis

For gene expression studies, surfaces of tissue culture plates were coated with each PA mixture and placed in a fume hood for drying overnight. rMSCs were seeded at a density of 3 x 10^3 cells per cm^2. After cells reached confluency, their media were replaced with osteogenic medium. Gene expression profiles of Runx2, collagen I and osteopontin were evaluated by quantitative RT-PCR (qRT-PCR) analysis.

Table 2.1 Primers used for qRT-PCR expression analysis

Gene	Primer Sequence:Forward/Reverse
Gapdh	5’-GTGCCAGCCTCGTCTCATA-3’
	5’-AACTTGCCGTGGGTAGAGTC-3’
Runx2	5'-GGACGAGGCAAGAGTTTCACT-3'
	5'-CCCTAAATCACTGAGGCGGT-3'
Collagen I	5’-TGACTGGAAGAGCGGAGAGT-3’
	5’-GGTCATGCTCTCTCCAAACC-3’
Osteopontin	5’-AGTTTGGCAGCTCAGAGGAG-3’
	5’-TGCTTGGAAGAGTTTCTTGCTT-3’

RNA isolation from rMSCs seeded on PA nanofibers and bare surfaces was performed by using TRIzol (Invitrogen) according to the manufacturer's instructions after 7 and 14 days of incubation. Yield and purity of extracted RNA were assessed by Nanodrop 2000 (Thermo Scientific). Samples were diluted to a concentration of 100 ng/μL prior to their use. Primers for PCR amplification of Runx2, collagen I, osteopontin and Gapdh are shown in Table 1. cDNA synthesis from RNA and qRT-PCR was performed using SuperScript III Platinum SYBR Green One-Step qRT-PCR Kit according to the manufacturer's instructions. mRNA levels were calculated and normalized to GAPDH according to comparative Ct method for each target gene.

2.2.14 *In Vivo* Experiments

In vivo experiments were carried out with 4 young adult New Zealand rabbits per group weighing between 2.8 and 3.2 kg. All animal studies were approved by Gülhane Military Medical Academy Animal Studies Ethical Committee, and all experiments were conducted in accordance with the NIH Guide for Care and Use of Laboratory Animals.

2.2.14.1 Surgical Procedure

GAG-PA and K-PA molecules were dissolved in ddH_2O at a concentration of 10 mM and sterilized under UV light for 1 h. Rabbits were anesthetized with an intramuscular injection (IM) of 35 mg/kg of ketamine hydrochloride and 5 mg/kg of xylazine hydrochloride. The region of operation was shaved and aseptically prepared for operation. Under general anesthesia, a proximal tibial metaphyseal surgical defect (2 mm in diameter) was made on the right tibia of animals by using a surgical drill and PA solutions were injected into the tibial defects. Defect entrances were sutured (Vicryl 4−0 absorbable suture) after PA injections. In the physiological saline sham

group, right tibial defects were formed in a similar fashion and sutured following the injection of physiological saline. IM antibiotics were given to each rabbit for 3 days following the operation. All the tibias were examined clinically at regular intervals for any sign of inflammation or infection for the duration of the study. GAG-PA/K-PA (n = 4) and physiological saline (n = 4) injected tibiae were surgically removed after 4 weeks for bone morphometric analysis and histology characterization. All rabbits were sacrificed with an intravenous injection of 100 mg kg^{-1} sodium pentobarbital. Tibiae were fixed with 10% formalin for 48 h and stored in 70% EtOH for Micro-CT measurements.

2.2.14.2 Micro Computed Tomography (Micro-CT) Analysis

Micro-CT scans were performed to quantify new bone formation and mineral density within the defect. The distal metaphyseal regions of all tibiae were scanned at 81 kV and 124 µA using a Skyscan1172 Micro-CT scanner. Specimens were scanned using a 0.25 mm aluminium-copper filter and under 305 ms exposure time. For each specimen, a series of 660 projection images were obtained with a rotation step of 0.7 three-frame averages and a total rotation of 360°. Each scan was preceded by flat field correction for a specific zoom and image format. A stack of two-dimensional X-ray shadow projections was reconstructed using NRecon software v1.6.9.4 (Skyscan) and morphometrically analyzed using CTAn software v1.14.4.1 (Skyscan). During reconstruction, dynamic image range, post-alignment value, beam hardening and ring-artifact reduction were optimized for each experimental set. The defect region was manually identified in each bone and defined as the general volume of interest (VOI).

2.2.14.3 Histological Analysis

For histological investigation, tibiae samples were decalcified with 14% EDTA solution and then embedded in paraffin. Tissues were sectioned with a Leica microtome at a 5 µm thickness. Sections were deparaffinised in xylene and rehydrated in serial ethanol solutions for hematoxyline and eosin (H&E) staining**.** Slides were assessed at 5X objective magnification for area analysis by using Image-J software. 1 mm x 2 mm sized area including defect site as central is drawn. Quantification was carried out by measuring the pink area percentage in defined site of the bone defect area for every sample. For Masson's Trichrome staining, paraffin embedded slides were fixed in Bouin's solution.

After incubation in Weigert's Iron Hematoxylin Solution, the slides were stained with Biebrich Scarlet-Acid Fuchsin and Aniline blue and dehydrated in ethanol and xylene. Samples were washed extensively between each staining. The collagen fibers were stained blue and nuclei were stained black under this staining protocol. For Alcian blue staining, sections were stained for 30 min with Alcian blue solution (1 g of Alcian blue 8GX (Sigma, UK) dissolved in 3% glacial acetic acid (Sigma, UK)), washed in running tap water for 2 min and counterstained with nuclear fast red stain (Sigma, UK) for 5 min. Finally, slides were washed for 1 min in running tap water. All sections were imaged under microscopy.

2.2.15 Statistical Analysis

All quantitative values are presented as mean ± SEM (standard error of mean), and all experiments were performed with at least three replicates. Two-way analysis of variance (ANOVA) was used for the statistical analysis of viability tests, quantification of mineral deposition and gene expression studies. Quantification of cortical bone

formation results were analyzed using Mann-Whitney *U*-test. A *p* value of less than 0.05 was considered statistically significant. All statistical tests were performed using Graph-pad Prism v5.0.

2.3 Results and Discussion

2.3.1 Characterization of Peptide Amphiphile (PA) Molecules and Self-Assembled PA Nanofibers

Scaffolds that mimic the structure and function of ECM components are able to improve cellular responses and show great promise in tissue engineering applications. Heparan sulfate is an important component of the bone ECM and assists in bone formation by providing structural support and controlling the presentation of growth factors to cell surface receptors [146, 147]. This ability of heparan sulfate makes it an attractive therapeutic agent for the treatment of bone defects, as heparan sulfate is able to bind and present growth factors such as FGF and BMP that play critical roles in defect healing following fracture haematoma. However, the *in vivo* delivery of heparan sulfate is not a well-controlled process. Consequently, we designed a synthetic scaffold, which mimics the structural and biochemical properties of sulfated glycosaminoglycans, and tested the efficiency of this system to assist in bone regeneration using an *in vivo* tibial bone defect model. The ability of self-assembled peptide amphiphile (PA) nanofibers to mimic natural ECM renders them attractive for regenerative medicine applications. PA nanofibers can be modified to meet the needs of a broad variety of tissues through the optimization of their functional peptide sequences. The PA molecules self-assemble into 1D nanostructures consisting of a fatty acid or a hydrophobic moiety linked to a hydrophilic peptide sequence. High-aspect-ratio cylindrical nanofibers are observed when the peptide sequence includes

amino acids with high β-sheet propensity. Screening of charged groups (by pH or ionic strength changes) results in a self-supporting gel formation, which is formed by a network of nanofibers with an enmeshed solvent [148].

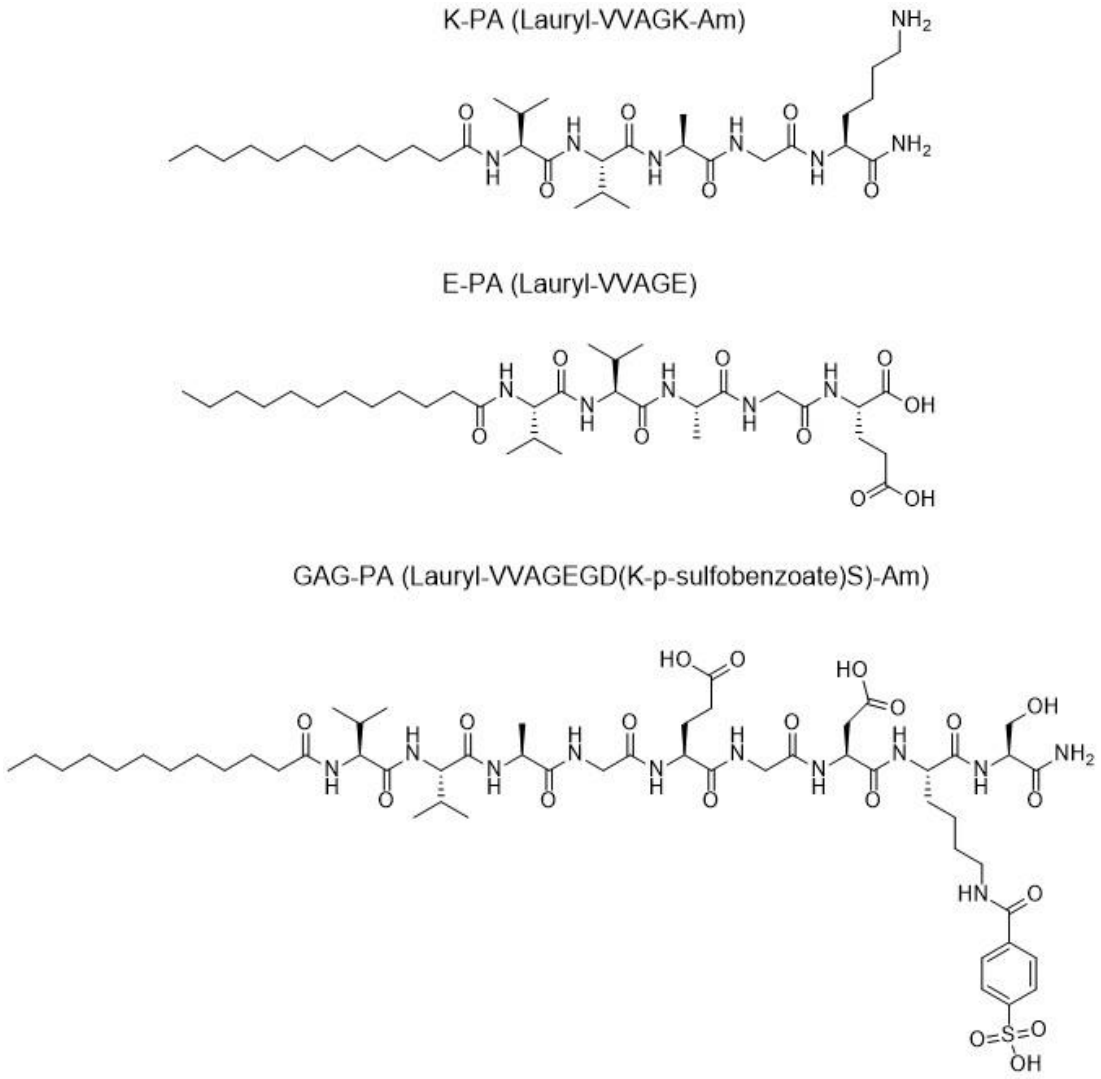

Figure 2.2 Chemical structures of the PA molecules

Hydrophobic collapse of alkyl groups and β-sheet formation between peptide molecules result in the formation of nanofibers in aqueous solutions, and short bioactive amino acid sequences can be presented at high densities on the surface of these nanofibers. In this study, glycosaminoglycan-mimetic and control peptide amphiphile (PA) molecules were synthesized using solid phase peptide synthesis method. GAG-PA (lauryl-VVAGEGD(K-p-sulfobenzoate)S)-Am) was used to mimic sulfated glycosaminoglycans (GAGs) by presenting functional groups such as sulfonate, hydroxyl and carboxylate moieties, while E-PA (lauryl-VVAGE) was used to present carboxylate groups and had no sulfonate groups [144]. K-PA, a positively charged molecule was used in order to induce nanofiber formation together with negatively charged PAs through electrostatic interactions (Figure 2.2). GAG-PA and E-PA molecules form nanofibers through self-assembly when mixed with K-PA. All peptide amphiphile molecules were characterized with LC-MS and purified by preparative HPLC (Figures 2.3-2.5). For charge neutralization, GAG-PA was mixed with K-PA at a 1:3 ratio to form GAG-PA/K-PA nanofibers, while E-PA and K-PA were mixed at a 1:2 ratio to form E-PA/K-PA nanofibers. Porous nanofiber networks were formed upon mixing oppositely charged PA molecules, as demonstrated by SEM images (Figure 2.6). CD spectra were acquired to explore the secondary structures of self-assembled PA networks, and suggest that the β-sheet structure with a chiral absorbance maximum at around 200 nm and minimum at around 220 nm, is the predominant secondary structure for both GAG-mimetic nanofibers and control nanofibers (Figure 2.7).

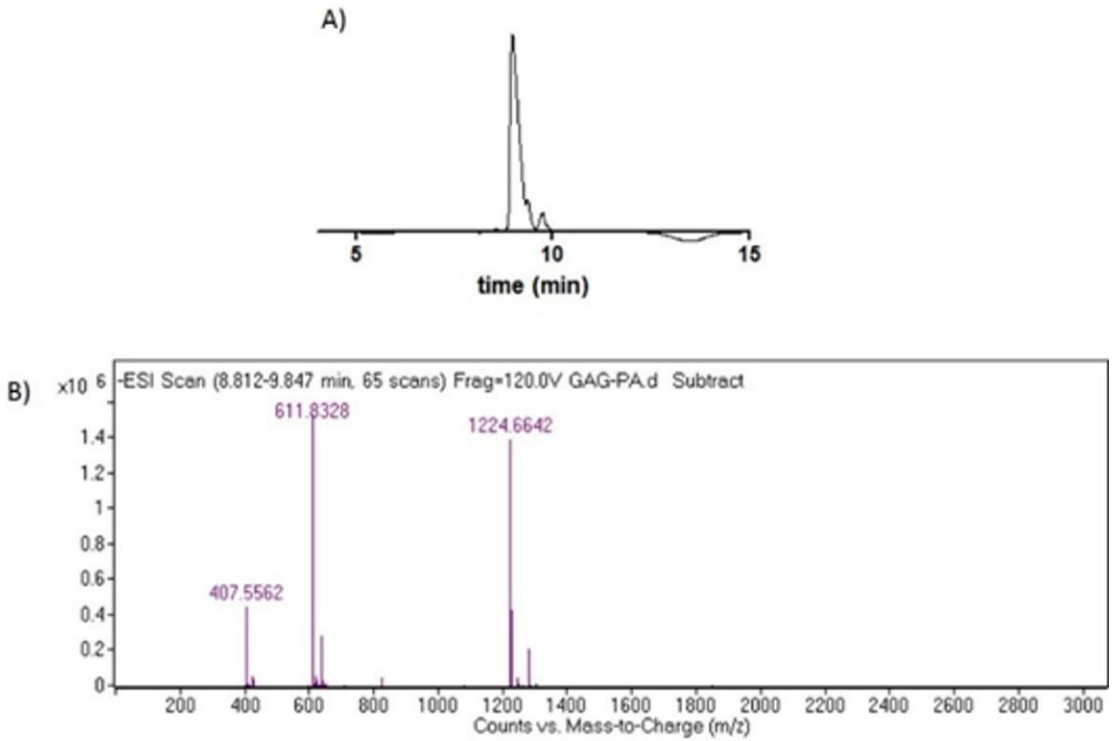

Figure 2.3 Liquid chromatogram and mass spectrum of GAG-PA. (A) RP-HPLC chromatogram of GAG-PA, the change of response units with respect to time at 220 nm. (B) Mass spectrometry of GAG-PA. $[M-H]^-$ (calculated): 1225.59, $[M-H]^-$(observed): 1224.66, $[M-2H]^{-2/2}$ (calculated): 611.79, $[M-2H]^{-2/2}$ (observed): 611.83, $[M-3H]^{-3/3}$ (calculated): 407.53, $[M-3H]^{-3/3}$ (observed): 407.55.

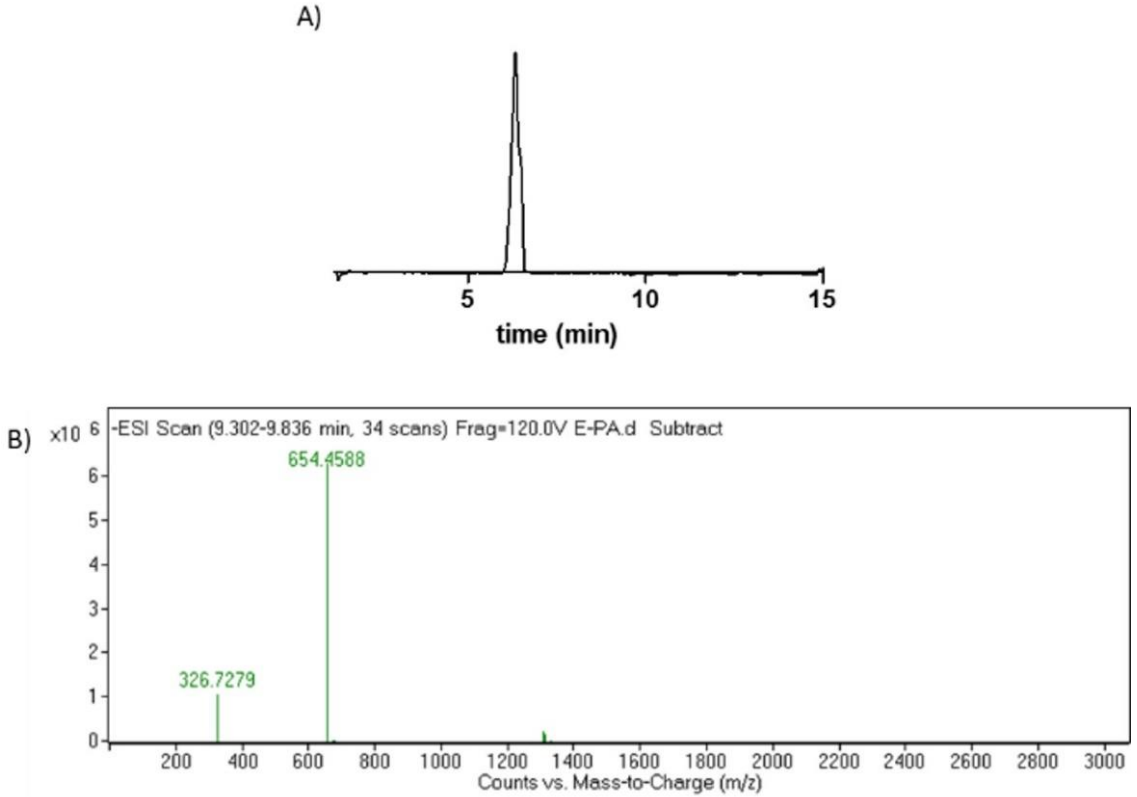

Figure 2.4 Liquid chromatogram and mass spectrum of E-PA. A) RP-HPLC chromatogram of E-PA, the change of response units with respect to time at 220 nm. (B) Mass spectrometry of E-PA. $[M-H]^-$ (calculated): 655.42, $[M-H]^-$ (observed): 654.45, $[M-2H]^{-2}/2$ (calculated): 326.71, $[M-2H]^{-\ 2/2}$ (observed): 326.72.

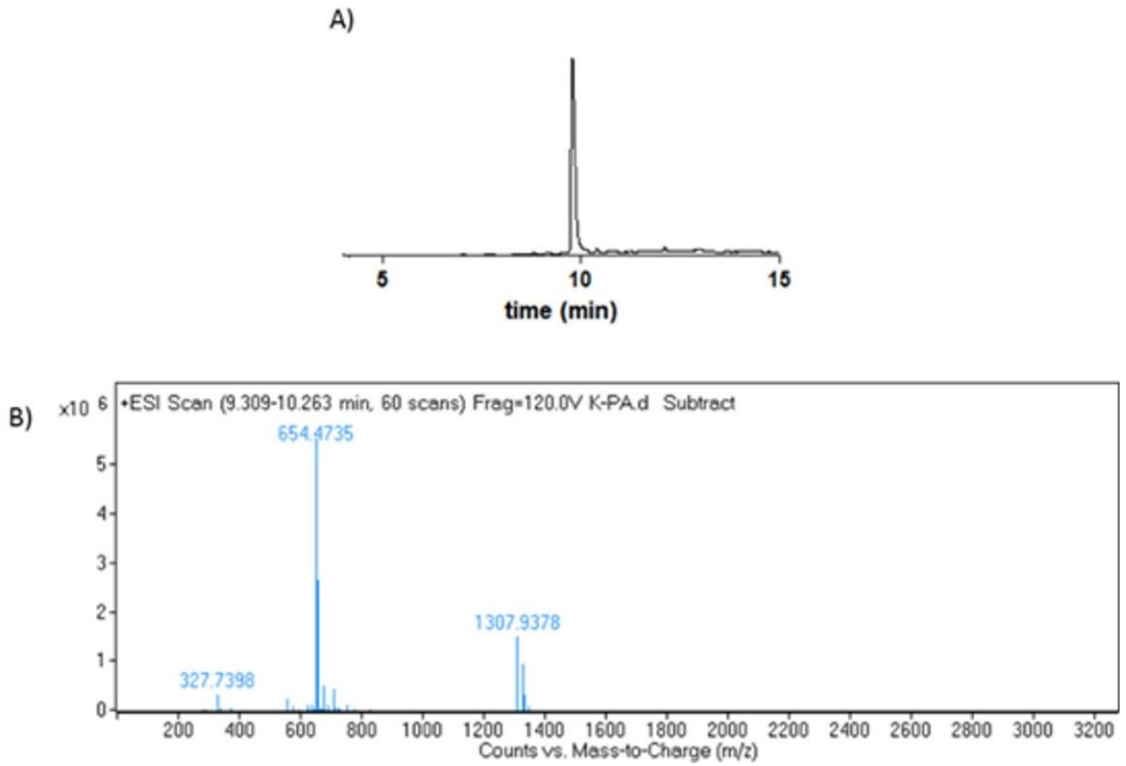

Figure 2.5 Liquid chromatogram and mass spectrum of K-PA. (A) RP-HPLC chromatogram of K-PA, the change of response units with respect to time at 220 nm. (B) Mass spectrometry of K-PA. $[M+H]^+$ (calculated):653.48, $[M+H]^+$(observed): 654.47, $[2M+H]^+$(calculated): 1307.96, $[2M+H]^+$ (observed): 1307.93, $[M+2H]^{+2}/2$ (calculated): 327.74, $[M+2H]^{+2}/2$ (observed): 327.73.

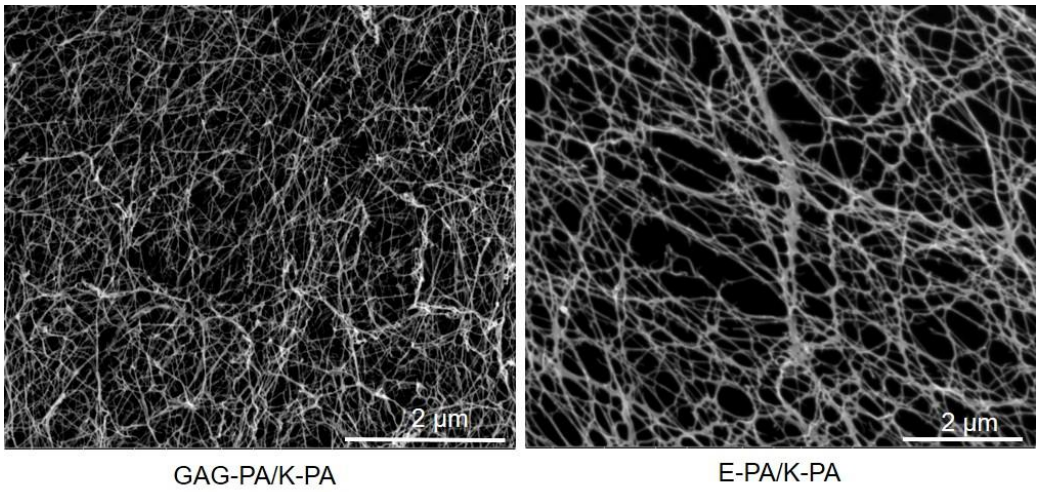

Figure 2.6 SEM images show the nanofibrous network.

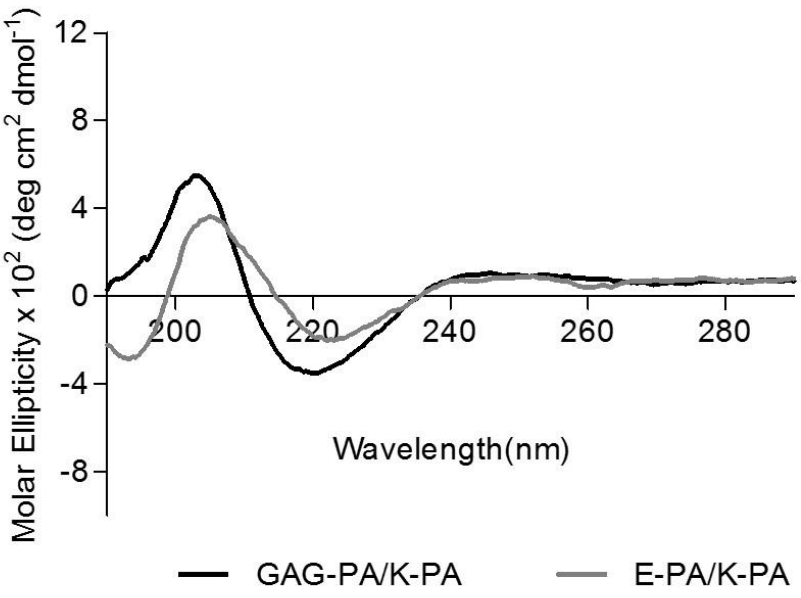

Figure 2.7 Circular dichroism spectra of the PA samples, demonstrating a predominance of β-sheet in the PA nanofibers.

FT-IR spectra of all PAs exhibit amide I, amide II and amide A bands. Amide I band is uniquely useful for analysis of protein secondary structural composition and conformational changes [149]. The bands in the regions of 1640-1620 cm^{-1} and 1695-1690 cm^{-1} have been assigned to β-sheet [150, 151]. In our study, all peptide nanofibers had amide I peaks located between 1630–1640 cm^{-1} region (Figure 2.8), indicating a β -sheet organization and validating our CD results (Figure 2.7).

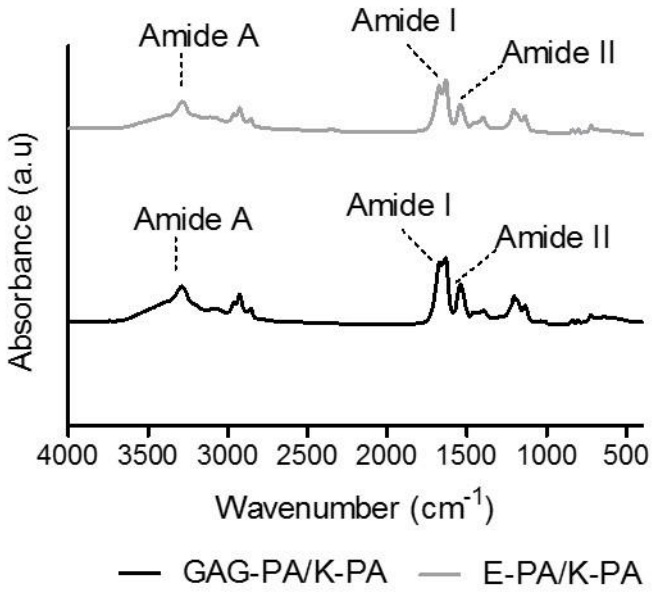

Figure 2.8 FTIR spectra of PA nanofibers. Both peptides displayed amide I peaks located in 1630–1640 cm^{-1} region, suggesting β-sheet formation.

2.3.2 Cell Behavior and Viability on PA nanofibers

The effect of GAG-mimetic peptide nanofibers on the viability of rMSCs was tested by calcein AM staining at varying time points (24, 48 and 72 h). The rMSCs were viable on all surfaces over the three day period. We did not observe any significant difference in the viability of cells on different peptide nanofiber scaffolds and bare

glass surface at varying time points (Figures 2.9 and 2.10). These results showed that peptide nanofibers provide a biocompatible environment.

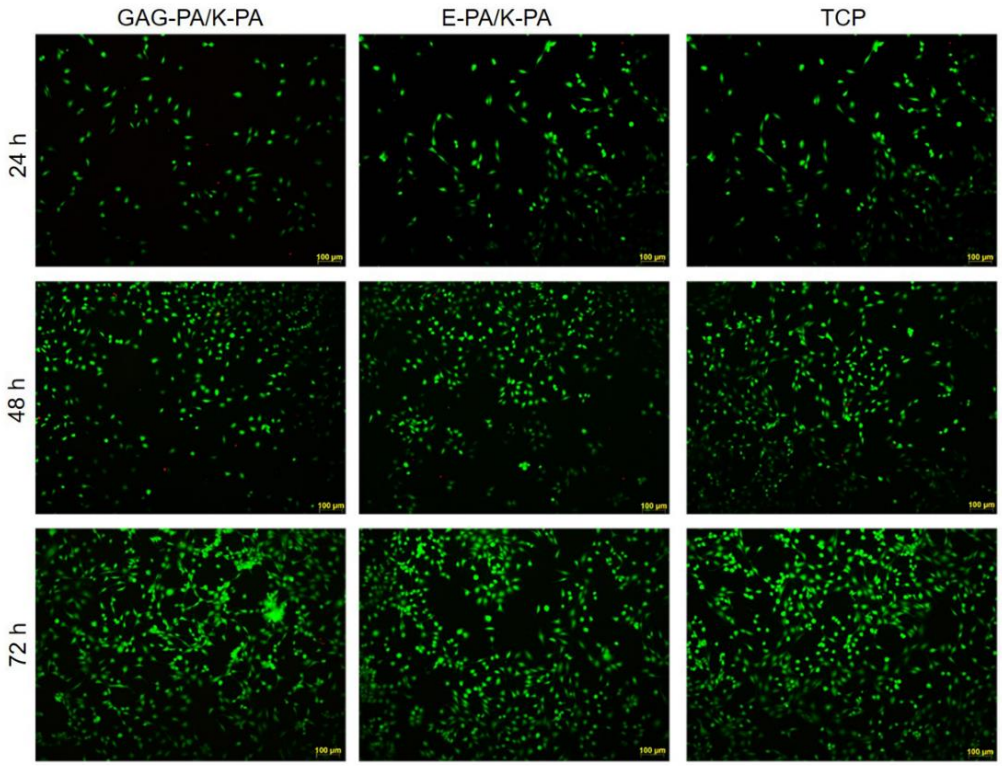

Figure 2.9 Viability of rMSCs cultured on peptide nanofibers and TCP, analyzed by calcein/ethidium homodimer live−dead assay.

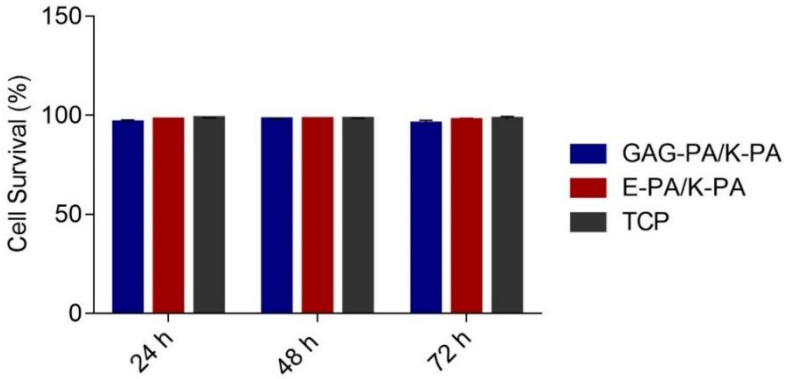

Figure 2.10 Viability of rMSCs cultured on peptide nanofibers and uncoated surface (TCP), analyzed by calcein ethidium homodimer live−dead assay.

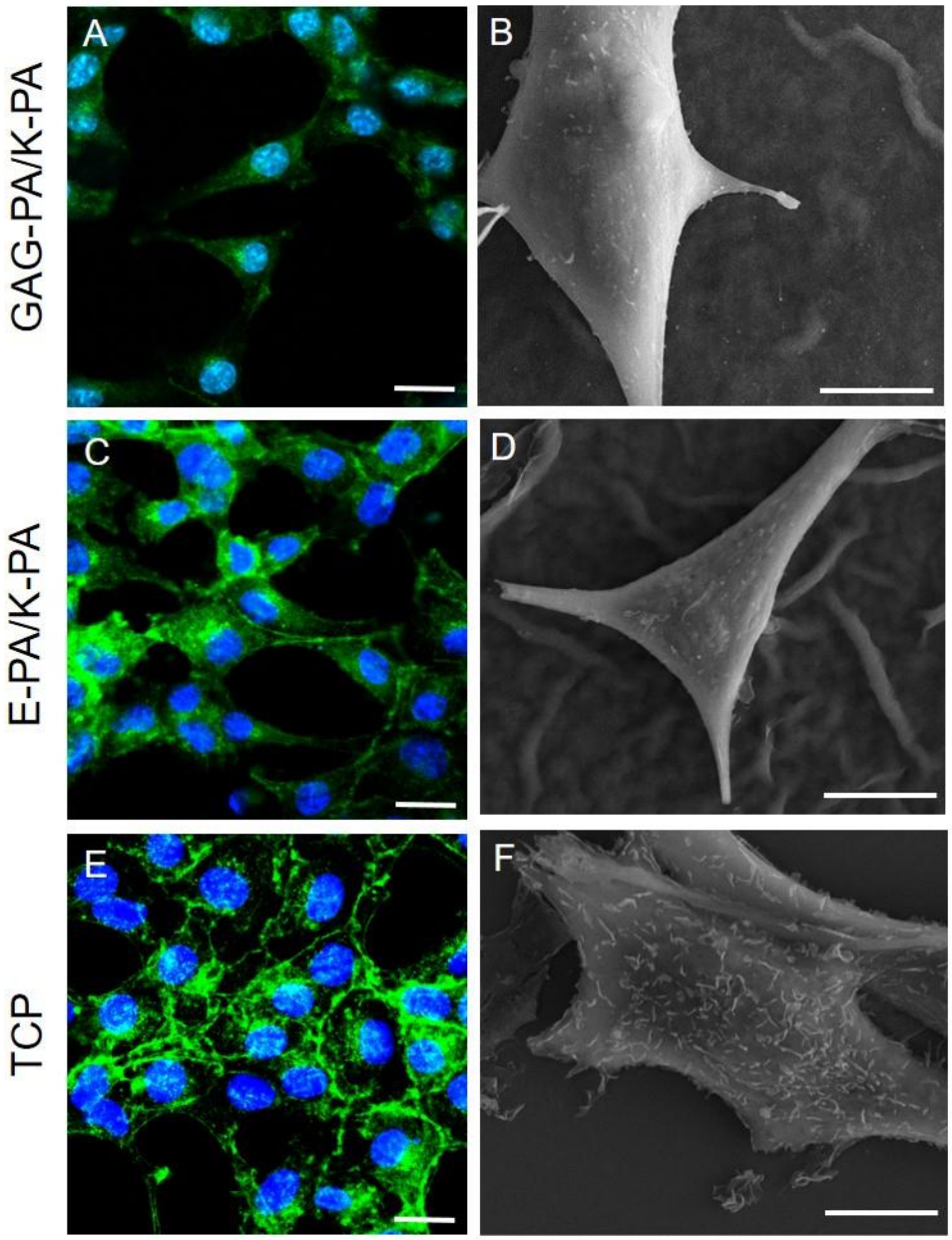

Figure 2.11 Morphology of rMSCs on PA nanofibers and TCP after 3 days of incubation. Actin filaments stained with phalloidin (green) and nuclei stained with TO-PRO-3 (blue) (A, C, and E). Scale bars are 20 μm. SEM images of rMSCs on PA nanofibers and TCP (B, D, and F). Scale bars are 5 μm.

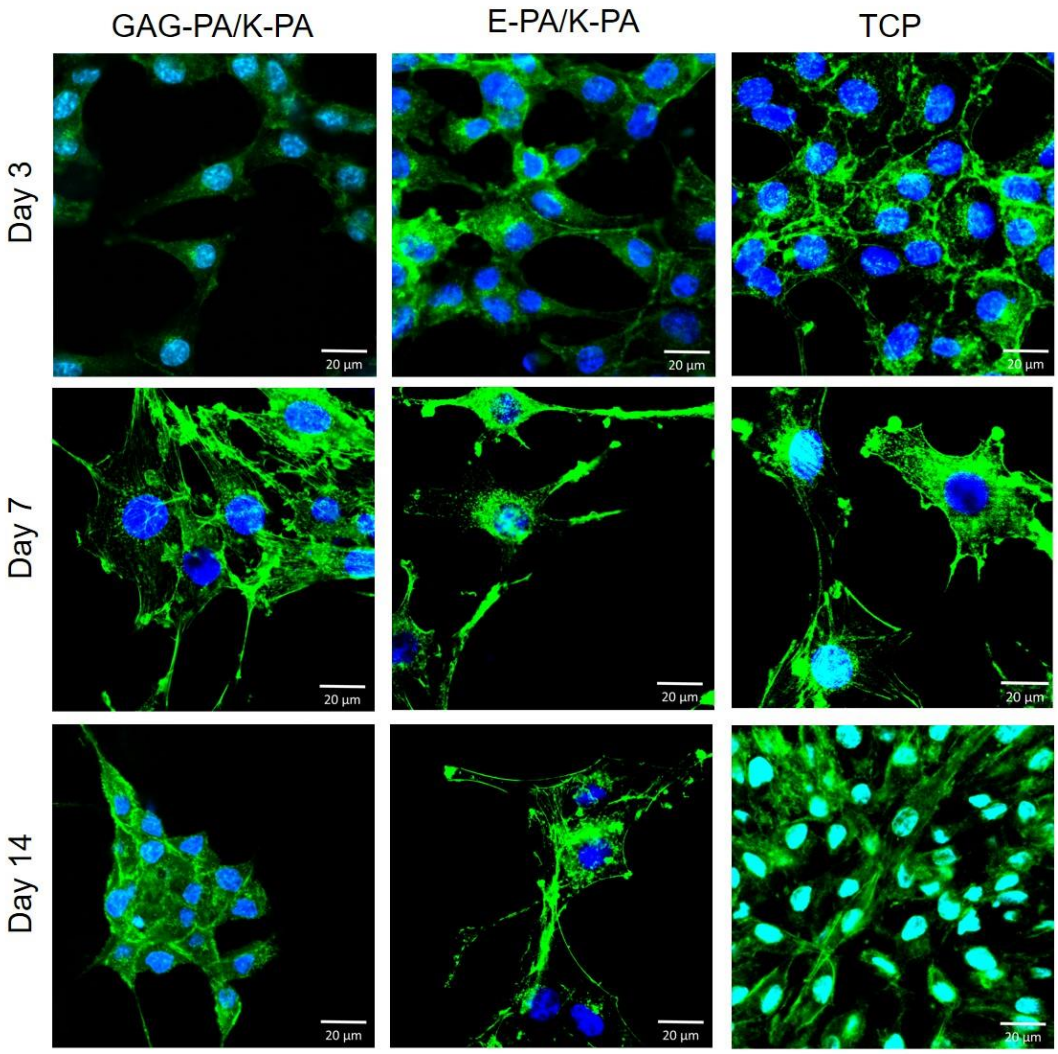

Figure 2.12 F-Actin filaments stained with phalloidin (green) showing actin networks formed by rMSCs on PA nanofibers and TCP. Nuclei were stained with TO-PRO-3 reagent (blue). Scale bars are 20 µm.

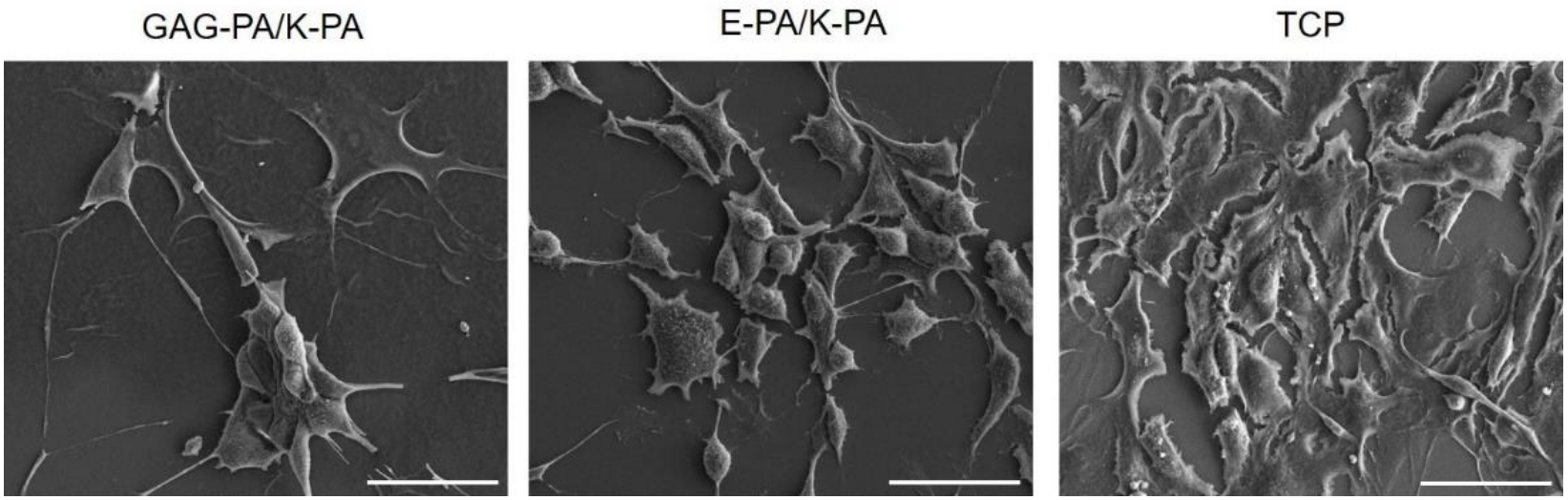

Figure 2.13 SEM images of rMSCs cultured on GAG-PA/K-PA, E-PA/K-PA nanofibers and TCP at 14 days after cell seeding. Scale bars are 40 μm.

SEM imaging and actin staining revealed that rMSCs had spread and showed the characteristic fibroblast-like phenotype of MSCs (*i.e.* a spindle-like morphology) after 3 days of incubation on PA nanofibers [152] (Figure 2.11). Phalloidin staining showed that cells adhere on PA nanofibers and form cytoskeletal attachments. From day 7 onward, cells on GAG-PA/K-PA nanofibers were found to cluster together and form bone like nodules, which is one of the indicators of osteogenic differentiation [153] (Figures 2.12 and 2.13). In contrast to our GAG-PA/K-PA observations, no clustering or nodule formation was present on E-PA/K-PA or TCP.

2.3.3 Alkaline Phosphatase Activity and Mineralization on Bioactive Peptide Nanofibers

Osteoblasts are the cells responsible for secreting organic and mineral matrices during new bone formation *in vivo*. MSCs express characteristic markers during their differentiation into the osteoblastic lineage, which can be quantified to determine the extent of the differentiation process. Previously, we showed that heparin mimetic peptide nanofibers are able to bind BMP-2 better than E-PA/K-PA nanofibers, which may promote bone repair by increasing the local concentration of growth factors secreted by osteoblasts [144]. A considerable difference was observed between the ALP activity of Saos-2 cells on GAG-PA/K-PA and E-PA/K-PA nanofibers, which is possibly due to the differentiative capacity of bioactive and non-bioactive PA networks to bind and present growth factors such as BMP-2.

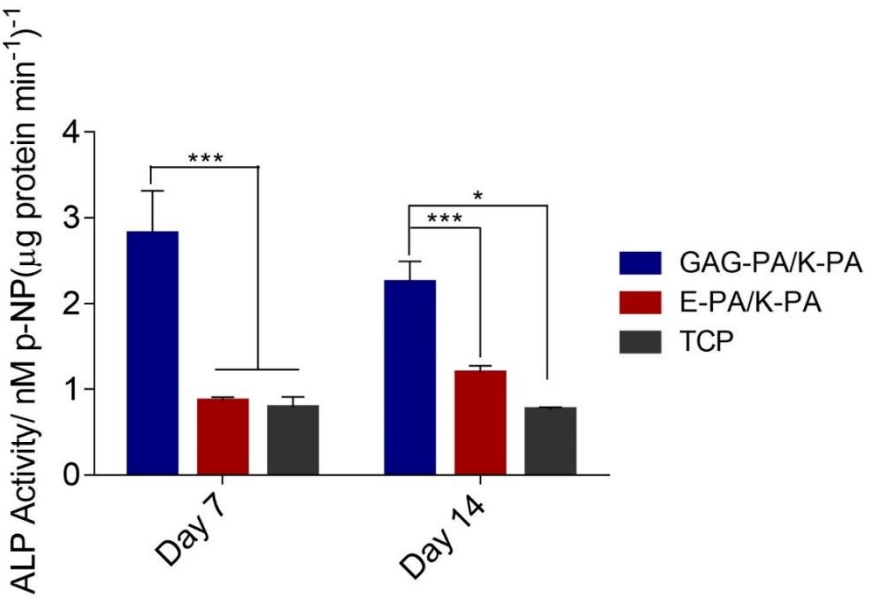

Figure 2.14 Impact of GAG mimetic peptide nanofibers on alkaline phosphatase activity on days 7 and 14, *$p < 0.05$, ***$p < 0.001$.

The osteogenic differentiation of MSCs occurs in three stages *in vitro* [154]. A peak in the number of cells is seen in the first stage (days one to four). This is followed by early cell differentiation from days 5 to 14, which involves the transcription and protein expression of alkaline phosphatase (ALP), an enzyme that promotes mineralization by providing inorganic phosphate [31, 154, 155]. Therefore, we tested the ALP activity of rMSCs cultured on GAG-PA/K-PA, E-PA/K-PA and TCP surfaces after 7 and 14 days of incubation in osteogenic medium. Maximum ALP activity was observed on day 7 for GAG-PA/K-PA, and was found to have decreased at day 14 (Figure 2.14).

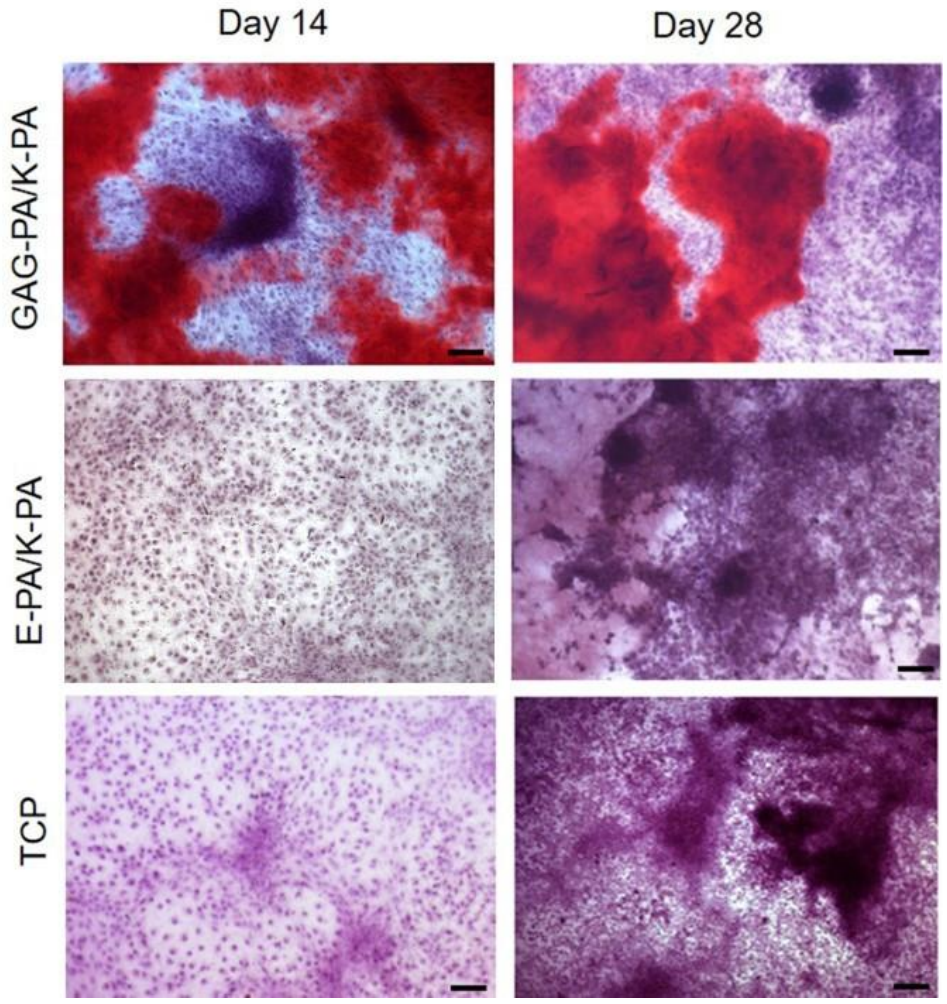

Figure 2.15 Biomineralization on peptide nanofibers and TCP on days 14 and 28 as demonstrated by Alizarin red staining. Scale bars are100 µm.

ALP activity starts to decline after this stage, and the final phase of osteogenic differentiation comprises the deposition of calcium and phosphate from days 15 to 28 [154, 156]. These calcium deposits can specifically be stained using Alizarin red S, which chelates Ca^{2+} and is a commonly used dye for the evaluation of bone mineralization [156, 157]. Cells cultured on GAG-mimetic peptide nanofibers in the presence of osteogenic supplements showed matrix mineralization with intense Alizarin red staining (Figures 2.15 and 2.16), in contrast to control cultures, which stained negatively for Alizarin red.

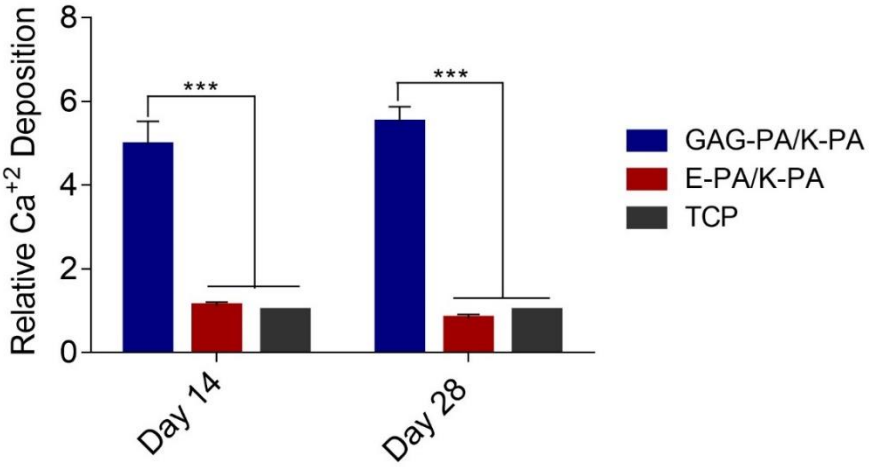

Figure 2.16 Quantification of relative calcium deposition on peptide nanofibers and TCP on days 14 and 28, ***$p < 0.001$.

2.3.4 Gene Expression Profiles of Osteogenic Markers

MSCs cultured in osteogenic media express markers also known to be expressed by bone-forming osteoblasts [158]. To understand whether the GAG mimetic peptide nanofiber systems were able to direct the differentiation of rMSCs towards the osteogenic lineage, gene expression profiles of cells cultured on peptide nanofiber network coated and bare surfaces were analyzed and quantified.

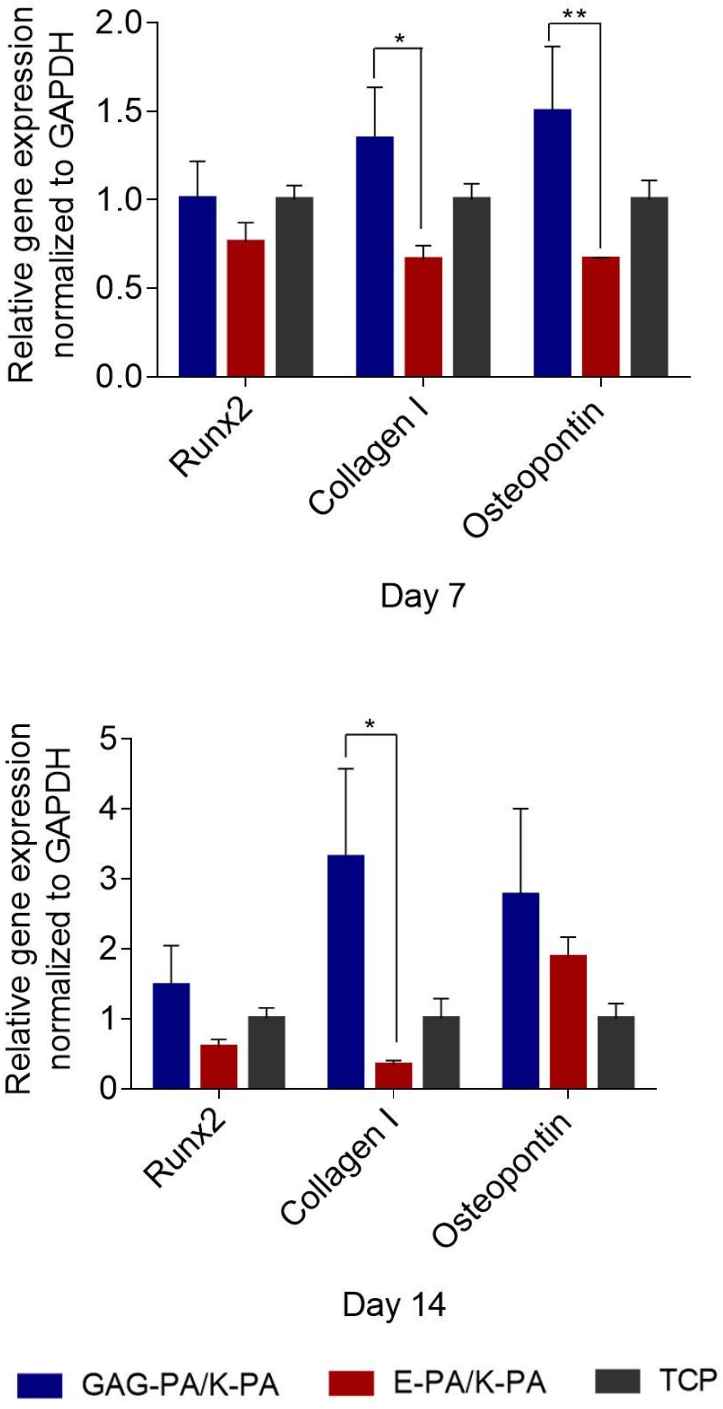

Figure 2.17 Gene expression analysis of Runx2, collagen-I, and osteopontin on days 7 and 14. Expression level of each gene was normalized against TCP and GAPDH was used as internal control, *$p < 0.05$, **$p < 0.01$.

Expressions of the osteogenic markers Runt-related transcription factor 2 (Runx2), type I collagen (collagen I) and osteopontin were examined at the mRNA level on days 7 and 14 (Figure 2.17). Runx2 is often referred to as the master switch of osteogenic differentiation [159] and its expression is usually analyzed during the early phases of osteogenic differentiation. The expression of Runx2 was upregulated by ~1.2 and 1.5 folds, when rMSCs were cultured on GAG-PA/K-PA compared to cells on TCP surfaces on days 7 and 14, respectively. This value was also upregulated by ~1.3 and 2.5 folds compared to cells on E-PA/K-PA surfaces on days 7 and 14, respectively. The major organic component of bone ECM is type I collagen, which is secreted at an early stage of osteogenic differentiation, providing a scaffold for mineral deposition [160, 161]. Osteopontin is a highly phosphorylated sialoprotein that is a prominent component of the mineralized extracellular matrices of bones [162]. Osteopontin expression was tested as a third osteogenic marker and found to be upregulated by ~1.5 and 2.8 folds for rMSCs cultured on GAG-PA/K-PA compared to cells on TCP surfaces on days 7 and 14, respectively. This value was also significantly upregulated by ~2.3 folds compared to cells on E-PA/K-PA surfaces on day 7, and 1.5 folds on day 14. Studies on the temporal expression of osteopontin during the formation of bone *in vitro* and during the formation of intramembranous and endochondral bone *in vivo* have revealed a biphasic pattern in which osteopontin is produced early in the differentiation of bone cells, with higher levels expressed after mineralization has been initiated [162]. More differences observed on day 7 is therefore consistent with previous studies. Mineralization can be initiated by the matrix vesicles budding from the plasma membrane of osteoblasts, which creates an environment suitable for the crystallization of calcium and phosphate [163]. Collagen can act as a template for this

process, and may also initiate and propagate mineralization independent of the matrix vesicles [164]. In addition, this protein plays an important role in cell adhesion, proliferation, and differentiation into osteoblast phenotype. Collagen I expression was significantly upregulated in cells when they were cultured on GAG-PA/K-PA compared to TCP, exhibiting an enhancement of ~1.3 and 3.3 folds on day 7 and 14. This value was also upregulated by ~2 and 10 folds compared to cells on E-PA/K-PA surfaces on days 7 and 14, respectively.

During ossification, MSCs proliferate while staying in close proximity, which results in the formation of dense cellular aggregations or primary bone nodules. The MSCs in these nodules start to differentiate into osteoprogenitor cells and finally osteoblasts [153]. MSCs on GAG-PA/K-PA gels start to aggregate from day 7 onwards and form bone nodules at day 14, as shown by phalloidin staining and SEM imaging (Figures 2.12 and 2.13).

MSCs have no extracellular calcium deposits, while differentiated osteoblasts are known to extensively deposit calcium crystals under both *in vivo* and *in vitro* conditions. Calcium deposits are therefore an indication of MSC to osteoblast differentiation and *in vitro* bone formation. In this study, the cells cultured on GAG-mimetic peptide nanofibers in the presence of osteogenic supplements showed higher matrix mineralization, suggesting that they were committed to the osteogenic lineage. On the other hand, the non-bioactive (E-PA/K-PA) peptide nanofiber group did not enhance differentiation into the osteogenic lineage. These results are consistent with our previous studies, in which GAG-mimetic peptide nanofibers were more effective in inducing osteogenic differentiation compared to the E-PA/K-PA group [144]. In addition, ALP activity was considerably higher in the GAG-PA treated group compared

to non-bioactive controls, and rMSCs undergoing differentiation on the GAG-PA nanofibers have revealed significant differences in the osteogenic gene expression profiles when compared to the E-PA group (Figure 2.17), suggesting that the GAG-mimetic nanofiber scaffold had altered the differentiation pattern of the stem cells. This may be due to their ability to recruit growth factors such as BMP to increase mRNA levels of downstream marker genes [165]. In addition, GAGs may facilitate osteoblast differentiation through Erk phosphorylation and Runx2 activity.

2.3.5 *In Vivo* Bone Regeneration Model

An ideal bone substitute should be tested both *in vitro* and *in vivo* prior to its evaluation in human beings to ensure its safety and effectiveness [166]. Tibial bone defect models are commonly used to study regeneration in long bones [167, 168]. Rabbits are one of the most commonly used animal models, and rank first among all animals used for musculoskeletal research [169]. After testing our system *in vitro*, we checked the regeneration ability of GAG-mimetic peptide nanofibers using a rabbit tibial defect model. The non-bioactive (E-PA/K-PA) peptide nanofiber group did not enhance differentiation into the osteogenic lineage. Therefore, E-PA/K-PA group was not utilized in *in vivo* studies.

2.3.5.1 Quantification of Bone Formation by Micro-CT

We reconstructed three-dimensional images from Micro-CT data of GAG-PA gel treated group and physiological saline treated group for analyzing new bone formation (Figure 2.18). The reconstructed 3-dimensional images showed that the GAG-PA gel treated group had more abundant cortical bone formation than the physiological saline treated group.

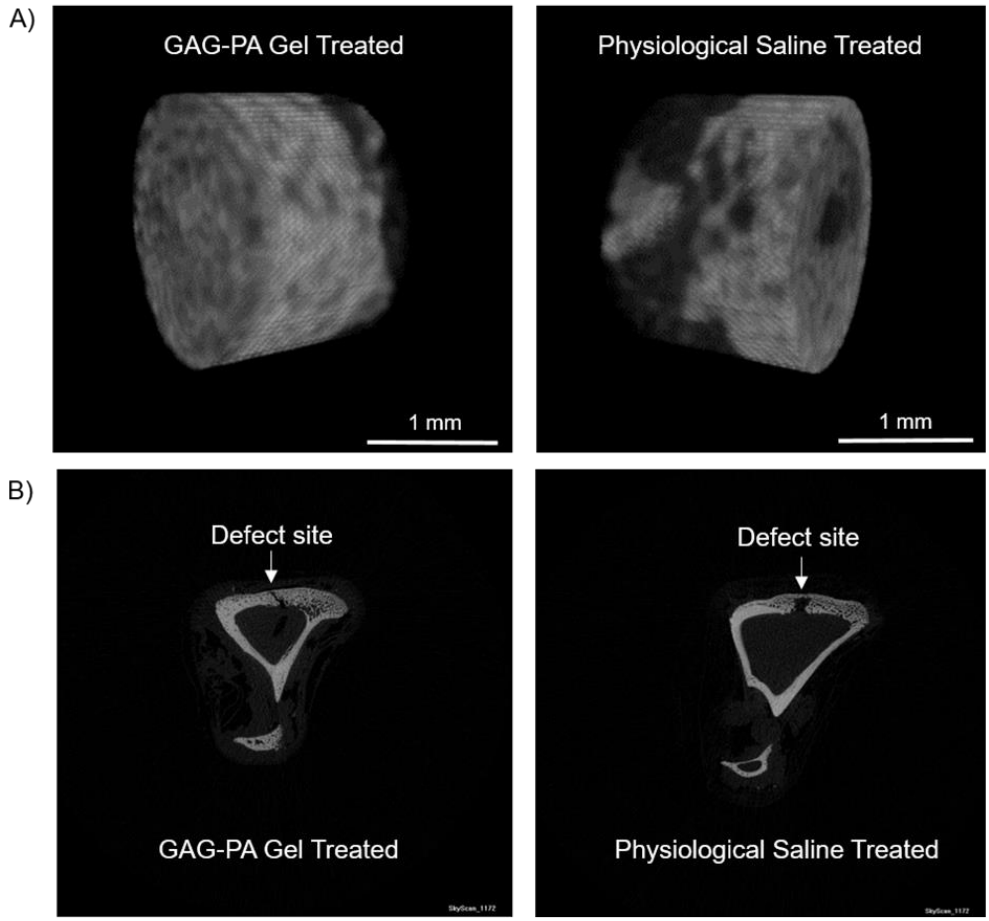

Figure 2.18 Representative Micro-CT images after 4 weeks of GAG-PA gel treatment. A) Three-dimensional reconstruction images of one voxel of interest showing newly formed bone (Grey color: the newly formed bone, black color: total defect volume). B) Nrecon images showing defect site.

In addition, bone volume to total volume ratio (BV/TV), which indicates the portion of mineralized tissue, was assessed. In fact, GAG-PA gel treated group has a statistically higher BV/TV than the physiological saline treated group (Figure 2.19A). BV/TV (%) value for gel treated group was ~53%, while it was ~19% for physiological saline treated group.

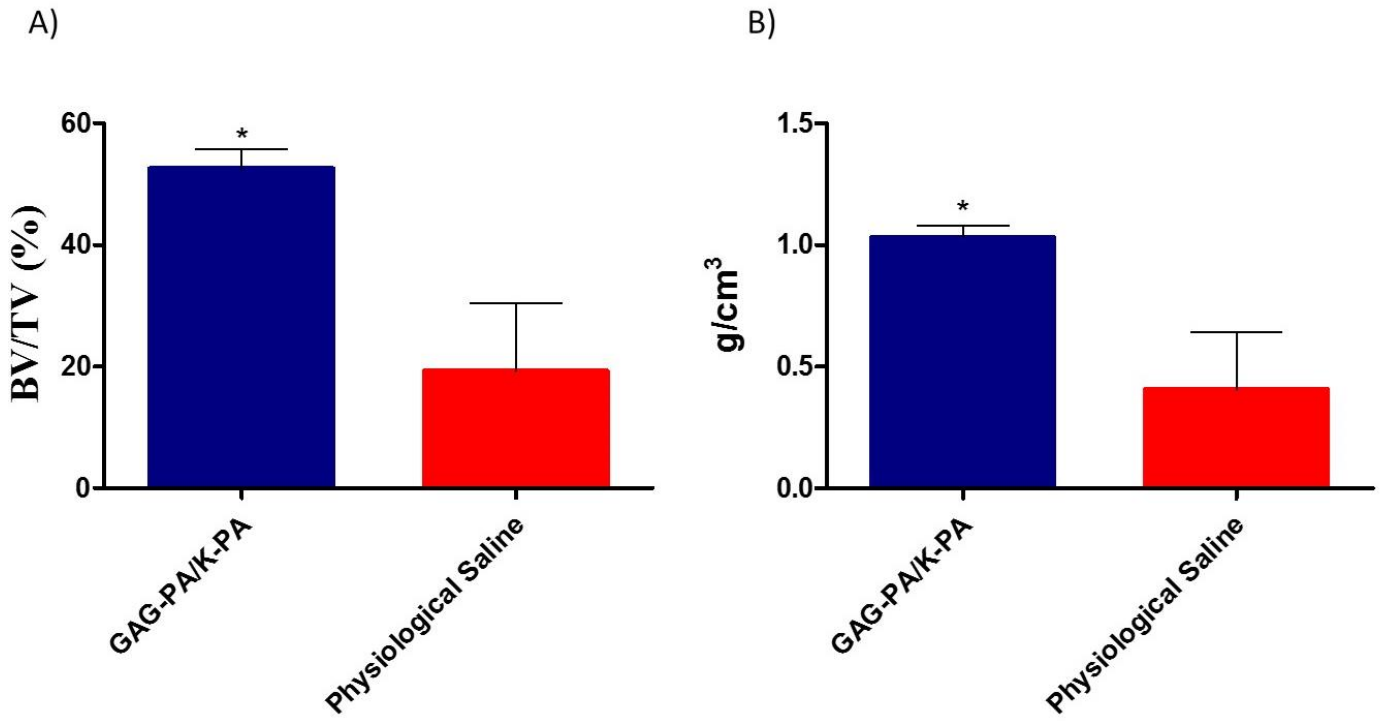

Figure 2.19 Newly formed cortical bone analysis at the defect site of rabbit tibia after 4 weeks of GAG-PA gel treatment. (A) BV/TV (%). (B) BMD of cortical bone, $*p < 0.05$.

Bone mineral density (BMD) can be defined as the volumetric density of calcium hydroxyapatite in a biological tissue in terms of $g.cm^{-3}$. In this study, Micro-CT quantifications have demonstrated that the animals receiving the GAG-PA gel treatment showed significantly higher BMD scores (~1.03 $g.cm^{-3}$), representing a 2.5 folds increase in BMD score compared to the physiological saline treated group (~ 0.41 $g.cm^{-3}$) (Figure 2.19B).

Fracture healing is a regenerative process consisting of several phases, each involving the formation of a different type of tissue [170]. In the first phase, the inflammatory response facilitates the formation of a hematoma and granulation tissue. The second phase is characterized by the formation of a soft callus that consists of cartilaginous or chondroid tissue, while the third phase involves the ossification of the soft callus to form a hard or bony callus consisting primarily of woven bone tissue. Lastly, the final stage comprises remodeling phase, in which woven bone is gradually replaced by lamellar bone tissue. Although these four phases are temporally sequential, the healing process is not spatially uniform. Therefore, at any given time during healing, the fracture callus is composed of a highly heterogeneous mixture of tissues [171].

The regenerated tissue in GAG-PA gel-treated bone defects was predominated by cortical bone and had a greater mineral density compared to physiological saline treated sham group, as shown by Micro-CT studies. It is therefore likely that the bioactive peptide matrix is able to increase the rate of bone mineralization and maturation. The rapid maturation rate of GAG-PA gel-treated tibial bone defects may be attributed to the ability of GAG-mimetic peptide nanofibers to enhance osteogenic differentiation, as our *in vitro* studies suggest that GAG-mimetic peptide nanofibers induce significantly higher calcium deposition, osteogenic marker gene expression and

ALP activity in rMSCs. As Micro-CT analysis of bone tissue does not give full insight into cellular composition dynamics and the biochemical characteristics of newly formed bone, histological stainings were also performed to further characterize the repair process.

2.3.5.2 Histological Evaluation of Regenerated Bone

Histological analyses were performed to investigate the regeneration process in tibial bone defects following GAG-PA gel and saline (control) treatment. The morphology of the damaged area and the formation of new bone ECM after surgery were examined by H&E staining. During bone healing, the soft, avascular cartilaginous callus is infiltrated by blood vessels and converted into woven bone, which is then gradually replaced by mature cortical bone [170]. In our study, physiological saline-treated defects mostly exhibited woven bone formation with vascular invasion, with minor presence of lamellar bone formation (Figure 2.20).

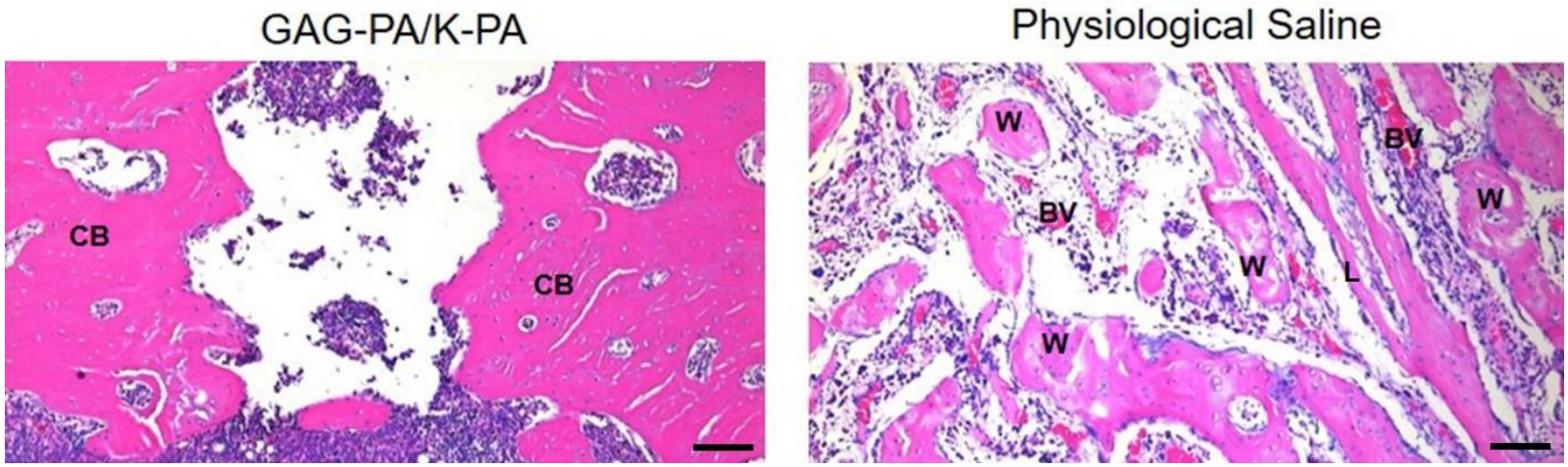

Figure 2.20 Histological evaluation of rabbit tibial defects after 4 weeks of hydrogel treatment. Tissue sections of GAG-PA gel and physiological saline control groups were stained with H&E, scale bars are 100 µm. (CB: Cortical bone, W: Woven bone, L: Lamellar bone, BV: Blood vessel).

On the other hand, GAG-PA gel treatment largely enhanced healing process resulting in the formation of cortical bone (Figures 2.19A and 2.20). Bone regeneration was also quantitatively evaluated by determining the percentage of regenerated area with respect to the original defect area using H&E results (Figure 2.21).

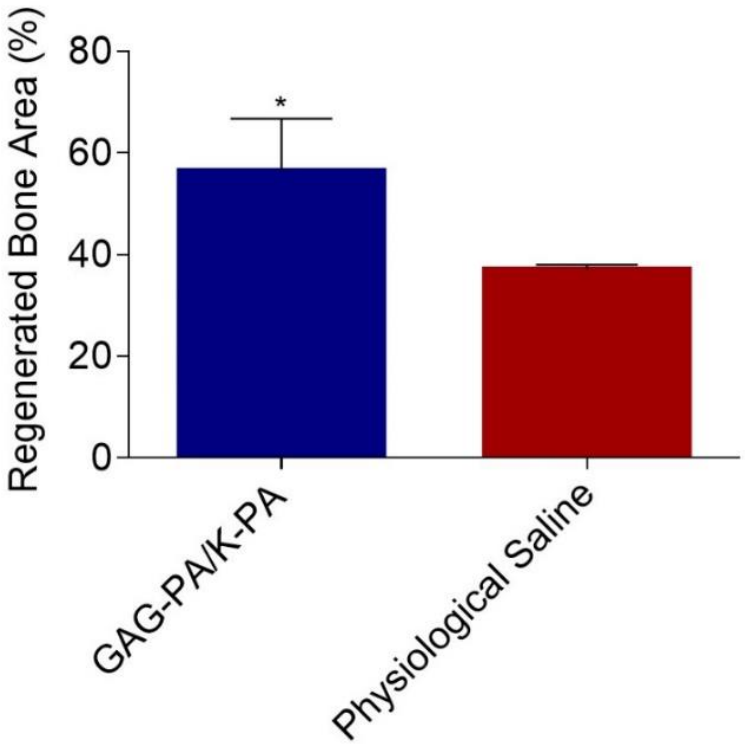

Figure 2.21 Regenerated bone areas were quantified through the histological evaluation of H&E results (G), *$p < 0.05$.

Masson's Trichrome staining studies showed that collagen deposition (as indicated by blue color) was prominent in tibial bone defects following both saline and GAG-PA gel treatment (Figures 2.22B-2.22E), indicating that bone matrix is actively synthesized during the treatment period. In GAG-PA gel treated defects, the newly formed bone turned to a red color which shows that the new bone had undergone maturation [167].

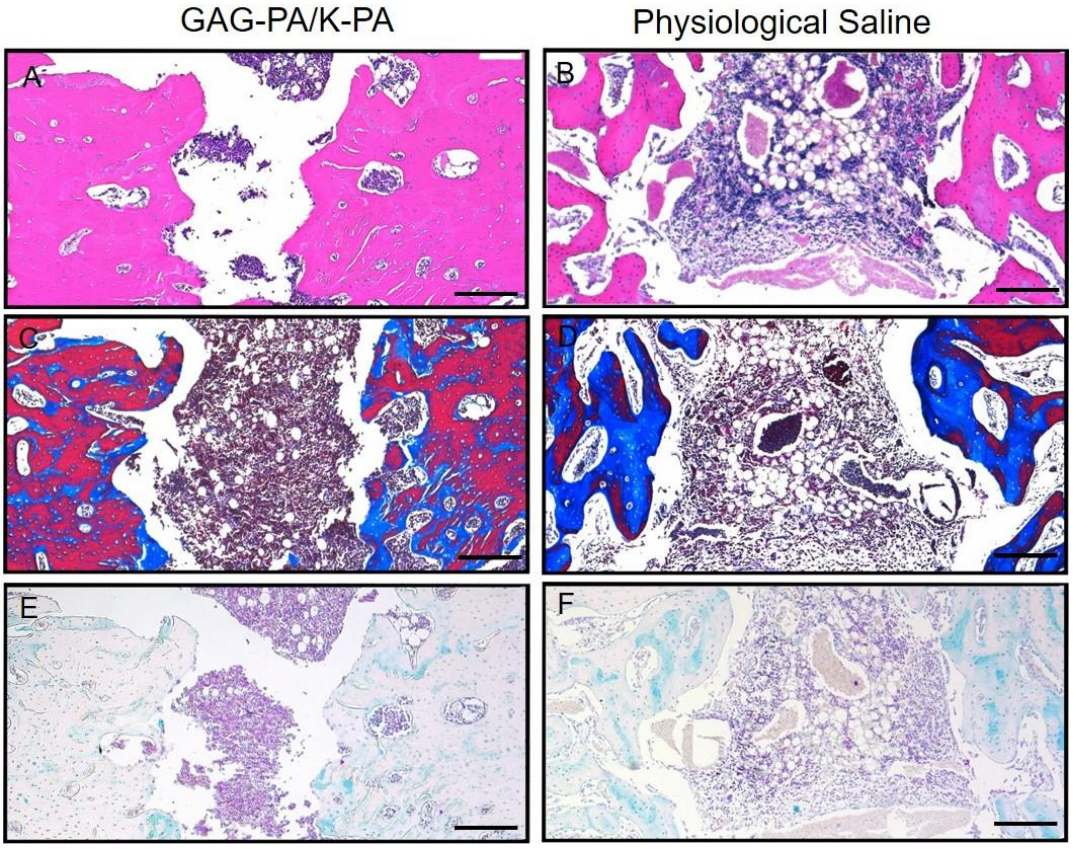

Figure 2.22 Histological evaluation of a tibial defect model after 4 weeks of GAG-PA gel treatment. Tissue sections of GAG-PA gel treated and physiological saline sham groups were stained with H&E (A, B) (Black lines show regenerated area). Deposition of bone matrix was confirmed by positive staining of collagen with Masson's trichrome staining (C, D). Endochondral ossification was observed by Alcian blue staining (E, F). Scale bars are 200 μm.

Both defects also stained positive for Alcian blue (blue color, Figures 2.22C-2.22F); however, Alcian blue staining was especially abundant in physiological saline treated defects (Figure 2.22F), suggesting an association between bone regeneration and cartilage formation [167].

Physiological saline-treated defects were mostly repaired with woven bone tissue, with small amounts of lamellar bone, as bone exhibits capacity for self-renewal [167]. On the other hand, GAG-PA gel treated defects were filled with a more compact form of bone, which indicates that the latter steps of bone healing had taken place in bioactive gel-treated tibiae. In addition, Image J analysis of H&E staining results suggests that the defect gap is bridged to a greater extent in GAG-PA gel-treated gels (Figure 2.21), which supports our Micro-CT results (Figure 2.19). High growth factor (VEGF, BMPs, FGF-1 and TGF-β) binding capacity of the GAG-mimetic peptide nanofibers is a potential factor contributing to the efficacy of the GAG-PA gel treatment [143, 144, 172, 173]. The growth factor and nanofiber interaction facilitates migration and invasion of multipotent MSCs originating from the periosteum, bone marrow, circulation, and the surrounding soft tissues [143, 144, 170]. Thus, bioactive groups on GAG-mimetic peptide nanofibers can facilitate the differentiation of MSCs to osteoblasts and enhance the bone formation as observed in the *in vitro* studies.

Previously, Sawyer *et al*. showed bone healing within a rat calvarial defect by using poly ε-caprolactone/tricalcium phosphate (mPCL–TCP) scaffolds with recombinant human (rh)BMP-2. Semi-quantitative measurements of the traverse sections demonstrated 30.6% ± 4.2 bone healing at 4 weeks [174]. Hao *et al*. showed that rabbit radial defects were implanted with a combination of rabbit adipose-derived stem cells encapsulated in collagen I gel with PLGA-β-TCP. After 8 weeks, the bone forming area was 44.2 ± 3.9%. After 16 weeks, the newly formed bone occupied 75.3 ± 2.6% of the total area and increased to 96.4 ± 2.3% eight weeks later [175]. Our model was able to induce 54% recovery within four weeks in a smaller defect; however, it should be noted that the present scaffold is cell-free and growth factor-free. Therefore,

inclusion of cells and growth factors may further improve the success of the GAG mimetic nanofiber system, which exhibits a high affinity for BMP-2 in particular. Further studies involving growth factor and cell encapsulation methods are therefore necessary to determine the full therapeutic potential of the present system.

2.4 Conclusion

In summary, we have demonstrated that GAG-mimetic peptide nanofiber system is able to provide a biocompatible and bioactive environment for promotion of osteogenic differentiation of stem cells. The rMSCs cultured on these peptide nanofibers exhibited enhanced alkaline phosphatase activity, calcium deposition, and osteogenic gene expression, which are the main indicators of bone-like mineralization. In addition, *in vivo* bone regeneration studies using this PA gel system demonstrated that GAG-PA gel treatment is associated with rapid maturation rate, higher cortical bone formation and mineralization compared to saline sham group. Therefore, the GAG-mimetic PA nanofiber gel is a promising candidate for the osteogenic differentiation of MSCs, and further studies regarding the *in vivo* efficiency of the PA nanofiber system may allow its use as an injectable scaffold to support the repair of bone defects in orthopedic applications.

Chapter 3

3. Osteoinductive Peptide Nanofibers Induce Osteogenic Differentiation of Rat Mesenchymal Stem Cells

3.1 Introduction

Mesenchymal stem cells (MSCs) show great promise for use in tissue-engineering applications because of their potential to regenerate many types of tissues, including bone, cartilage, adipose, and muscle [176]. Peptide nanofibers containing bioactive sequences are remarkably similar to the extracellular matrix in structure and function, and can be utilized to promote or modulate the differentiation of MSCs into specific cell lineages [132, 177]. In this work, a peptide amphiphile (E_3-PA) molecule with a triple glutamic acid sequence, derived from a non-collagenous matrix protein, was designed and synthesized. It was shown that E_3-PA molecules induced the differentiation of bone marrow derived rat MSCs into the osteogenic lineage.

3.2 Experimental Section

3.2.1 Materials

4-(2′,4′-dimethoxyphenyl-Fmoc-aminomethyl)-phenoxyacetamido-norleucyl-MBHA resin (Rink amide MBHA resin), Fmoc-Asp(OtBu)-Wang resin, all protected amino acids, HBTU, lauric acid, and DIEA were purchased from Nova-Biochem, ABCR, or Sigma-Aldrich. Calcein-AM and other cell culture materials were purchased from Invitrogen. All other chemicals and materials used in this study were purchased from Thermo Scientific or Sigma-Aldrich.

3.2.2 Synthesis of PA Molecules

Fmoc solid phase peptide synthesis method was used to synthesize Lauryl-Val-Val-Ala-Gly-Lys-Lys-Lys-Am (K_3-PA) and Lauryl-Val-Val-Ala-Gly-Glu-Glu-Glu (E_3-PA). Rink amide MBHA resin (Novabiochem) was used as the solid support for K_3-PA, while Fmoc-Glu(OtBu)-Wang resin (100-200 mesh) served as solid support for E_3-PA. Amino acid couplings were carried out with 2 molar equivalents of Fmoc protected amino acid, 1.95 molar equivalents of HBTU, and 3 molar equivalents of DIEA for 2 h. Fmoc protecting groups were removed from N^{α}-amino moieties through exposure to 20% piperidine in dimethylformamide (DMF) solution for 20 min. In order to block the remaining free amine groups after amino acid coupling, 10% acetic anhydride in DMF solution was used. The resin was washed by using DMF and dichloromethane after each step. The cleavage of PAs and protecting groups from the resin was carried out with a mixture of TFA: TIS: H_2O at a ratio of 95:2.5:2.5 for 2.5 h. Excess TFA was removed by rotary evaporation, and PAs were precipitated using ice-cold diethyl ether at −20 °C overnight. The precipitate was then collected by centrifugation, dissolved in ultrapure water and frozen at −80 °C overnight. The frozen samples were lyophilized for 4 days. The identity and purity of peptide amphiphile molecules were determined by LC-MS (Agilent 6530−1200 Q-TOF) analysis. Mass spectra were obtained with an Agilent LC-MS equipped with Agilent 6530 Q-TOF with an ESI source and Zorbax Extend-C18 2.1 mm × 50 mm column for basic conditions and Zorbax SB-C8 4.6 mm × 100 mm column for acidic conditions. A gradient of water (0.1% formic acid or 0.1% NH_4OH) and acetonitrile (0.1% formic acid or 0.1% NH_4OH) was used as the mobile phase. To purify the peptides, an Agilent preparative reverse-phase HPLC system equipped with Zorbax Extend-C18 21.2 mm

× 150 mm column was used for basic conditions, and Zorbax SB-C8 21.2 mm × 150 mm column was used for acidic conditions. A gradient of water (0.1% TFA or 0.1% NH_4OH) and acetonitrile (0.1% TFA or 0.1% NH_4OH) was used as the mobile phase. Positively charged PAs were treated with 0.1 M HCl solution and lyophilized to remove residual TFA.

3.2.3 Formation of Self-Assembled PA Nanofibers

Stock solutions of PAs were prepared in distilled water. For nanofiber formation, E_3-PA (0.75 mM) was mixed with K_3-PA (1 mM) at 1:1 (v/v) ratio, respectively, in order to stabilize all net charges. Tissue culture plate surfaces were coated with PA mixture, and then plates were placed under laminar flow hood for drying overnight. After drying, they were sterilized with UV light for an hour before cell culture studies. After addition of the cell culture medium, these nanofibers formed a thin hydrogel that is several mm thick.

3.2.4 Characterizations of Self-Assembled PA Nanofibers

3.2.4.1 Circular Dichroism (CD)

CD samples were prepared by mixing oppositely charged PA solutions (1 mM) at 3:4 volume ratio to stabilize all net charges. This mixture was then diluted to a final peptide concentration of 0.33 mM in a final volume of 300 μL. A JASCO J815 CD spectrometer was used at room temperature for the acquisition of CD spectra, which were measured in the range of 300 nm to 190 nm with a data pitch of 0.1 nm, a scanning speed of 100 nm min^{-1}, and all measurements representing three accumulations. Digital Integration Time (DIT) was selected as 1 s, bandwidth as 1 nm, and the sensitivity as standard.

3.2.4.2 Scanning Electron Microscopy (SEM) Imaging

1 wt % solution of E_3-PA was mixed with 1 wt % solution of K_3-PA at 3:4 volume ratio on a silicon wafer cleaned previously in acetone, ethanol and water, respectively. PA hydrogels formed on the silicon wafer were incubated at room temperature for 30 min, dehydrated in 20%, 40%, 60% and 80% ethanol solutions, for 10 min in each solution, and finally incubated in absolute ethanol for 3-4 h. Then, the hydrogel was critical point dried with an Autosamdri®-815B Tousimis CPD and coated with 5 nm Au/Pd by sputtering before the SEM imaging. FEI Quanta 200 FEG SEM with an ETD detector in high vacuum mode and with 5 kV electron beam energy was used for the imaging of E_3/K_3-PA at 30,000x magnification.

3.2.5 Cell Culture and Maintenance

rMSCs (Invitrogen) were used in all cell culture experiments at passage number 7. Cells were cultured in 75 cm^2 flasks at a density of 3 x 10^3 cells per cm^2 at 37 °C in a humidified incubator and supplied with 5% CO_2. The rMSCs were maintained in low glucose Dulbecco's Modified Eagle's Medium (DMEM) with L-glutamine supplemented with 10% fetal bovine serum (FBS) and 1% penicillin/streptomycin. All cell experiments were carried out after the cells reached 90% confluency. The culture medium was changed every 3-4 days. Cells were seeded under the same conditions used for their maintenance. For gelatin group, tissue culture plates were coated with 0.1% porcine gelatin (Millipore). For mineralization experiments, gene expression analysis and AFM studies, the seeded cell medium was replaced with osteogenic medium (DMEM with 10% FBS supplemented with 10 mM β-glycerophosphate, 50 μg mL^{-1} ascorbic acid and 10 nM dexamethasone) after reaching confluency.

3.2.6 Viability Assay

The viability of rMSCs incubated on PA-coated, gelatin-coated and uncoated tissue culture plates was studied by Live/Dead Assay (Invitrogen). Briefly, cells were seeded on PA-coated, gelatin-coated and uncoated 96-well tissue culture plates at a density of 5 x 10^3 cells/well. After 24 h of incubation, cell medium was discarded; cells were washed with PBS and then incubated with 2 μM calcein-AM and 2 μM EthD-1 in PBS for 30 min at room temperature. After incubation, images were taken at three random points per well with a fluorescent microscope (Zeiss, Axio Scope A1) at 100x magnification. All samples were analyzed in triplicate. Live and dead cells were counted by using Image J.

3.2.7 Actin Staining of rMSCs on PA Nanofiber-Coated Surfaces

Glass coverslips were coated with E_3/K_3-PA and cells were seeded on top of the PA coated, gelatin-coated and uncoated surfaces at a density of 4×10^4 cells per coverslip. After 7 and 14 days of culture in osteogenic medium, phalloidin/TO-PRO-3 staining was performed for PA coated and bare surfaces. Before staining, cells were fixed with 4% formaldehyde for 15 min and permeabilized with 0.1% Triton-X for 10 min at room temperature. Samples were incubated with 3% (w/v) bovine serum albumin (BSA)/PBS for blocking for 30 min. Actin filaments of the cells were initially stained with 1:500 diluted FITC-conjugated phalloidin (Thermo Fisher) in 3% (w/v) BSA/PBS for 20 min. After serial washing steps, samples were stained with 1:1000 diluted TO-PRO-3 (Thermo Fisher) or 1:3000 diluted DAPI (Thermo Fisher) for 20 min for the visualization of nuclei. Coverslips were mounted with Prolong Gold Antifade Reagent (Invitrogen). Cytoskeletal organizations of cells on E_3/K_3-PA

nanofibers, gelatin-coated and bare glass were observed using a Zeiss LSM 510 confocal microscope at 630x magnification.

3.2.8 Alkaline Phosphatase (ALP) Activity Assay

In order to measure the ALP activity of rMSCs, degradation of *p*-nitrophenol due to endogenous ALP activity was quantified after 3, 7 and 14 days of culture in osteogenic medium. Briefly, cells were seeded on PA nanofiber-coated, gelatin-coated and uncoated TCP surfaces of 48-well plates at a density of 2 x 10^4 cells per well and the cell medium was replaced with osteogenic medium after the cells reached confluency. Cells were rinsed with PBS at predetermined time points. M-PER protein extraction kit (Thermo) with 5% protease inhibitor solution was used to extract proteins. Pierce BCA protein assay (Thermo) was performed to quantify the amount of proteins obtained from the cells according to the manufacturer's protocol. To measure ALP activity, 50 µL of the protein sample was incubated with 150 µL of *p*-nitrophenol phosphate substrate in 96-well plates for 30 min on a shaker. Serial dilutions of *p*-nitrophenol in 0.25 M NaOH solution were used as standards. Finally, the optical density of the samples was determined at 405 nm using a Spectramax M5 microplate reader and ALP results were normalized to the amount of total proteins at each time point tested.

3.2.9 Gene Expression Analysis

For gene expression studies, rMSCs were seeded on PA-coated, gelatin-coated and bare tissue culture plates of 6 well plates at a density of 2.5 x 10^5 cells per cm^2. After cells reached confluency, their media were replaced with osteogenic medium. Gene expression profiles of Runx2 (*Runx2*), collagen I (*Col1A1*), and osteopontin (*Spp1*) were evaluated by qRT-PCR analysis for investigating osteogenic differentiation.

RNA isolation from rMSCs seeded on PA nanofibers, gelatin-coated and bare surfaces were performed by using TRIzol (Invitrogen) according to the manufacturer's instructions after 3, 7 and 14 days of incubation. Yield and purity of extracted RNAs were assessed by Nanodrop 2000 (Thermo Scientific). Samples were diluted to a concentration of 100 ng/μL prior to their use. Primers for PCR amplification of Runx2, collagen I, osteopontin and Gapdh are shown in Table 3.1. cDNA synthesis from RNA and qRT-PCR were performed using SuperScript III Platinum SYBR Green One-Step qRT-PCR Kit according to the manufacturer's instructions. mRNA levels were calculated and normalized to Gapdh according to comparative Ct method for each target gene [178].

Table 3.1 Primers used for qRT-PCR expression analysis

Gene	Primer Sequence:Forward/Reverse
Gapdh	5'-GTGCCAGCCTCGTCTCATA-3'
	5'-AACTTGCCGTGGGTAGAGTC-3'
Runx2	5'-GGACGAGGCAAGAGTTTCACT-3'
	5'-CCCTAAATCACTGAGGCGGT-3'
Collagen I	5'-TGACTGGAAGAGCGGAGAGT-3'
	5'-GGTCATGCTCTCTCCAAACC-3'
Osteopontin	5'-AGTTTGGCAGCTCAGAGGAG-3'
	5'-TGCTTGGAAGAGTTTCTTGCTT-3'

3.2.10 Detection of Mineralization by Alizarin Red Staining

Calcium deposition on the surface of E_3/K_3-PA peptide nanofibers was measured on days 3, 7 and 14 using Alizarin red staining. Briefly, rMSCs were seeded on PA-coated, gelatin-coated and bare tissue culture plates of 96 well plates at a density of 1 x 10^4 cells per well in DMEM containing 10% FBS and 1% penicillin-streptomycin. Cells were cultured in this medium until they reached confluency, and the medium was then replaced with fresh osteogenic medium. Osteogenic medium was replenished every 3-4 days over the course of experiments. At pre-determined time intervals, cells were fixed with ice-cold ethanol for 1 h and stained with 40 mM Alizarin red S for 30 min on a shaker. Then, samples were washed 4-5 times with double-distilled water to remove non-specific Alizarin red binding. Calcium nodules were imaged in PBS under light microscope. In order to quantify deposited calcium, PBS was discarded and the samples were incubated in 10% cetylpyridinium chloride for 30 min at room temperature. At the end of the incubation period, the solution was transferred to 96-well plates and absorbance measurements were performed at 562 nm.

3.2.11 Statistical Analysis

All quantitative values are presented as mean ± SEM (standard errors of mean), and all experiments were performed with at least three replicates. One-way ANOVA and two-way ANOVA were used for the statistical analysis of results of viability test, ALP activity assay, gene expression studies and quantification of mineral deposition. A p value of less than 0.05 was considered statistically significant. All statistical tests were performed using GraphPad Prism v7.00.

3.3 Results and Discussion

3.3.1 Characterization of Peptide Amphiphile (PA) Molecules and Self-Assembled PA Nanofibers

Fmoc solid phase peptide synthesis method was used to synthesize PA molecules [Lauryl-VVAGEEE (E_3-PA) and Lauryl-VVAGKKK-Am (K_3-PA)] (Figure 3.1). The E_3-PA containing osteoinductive Glu-Glu-Glu peptide sequence was inspired by non-collagenous matrix proteins [179, 180].

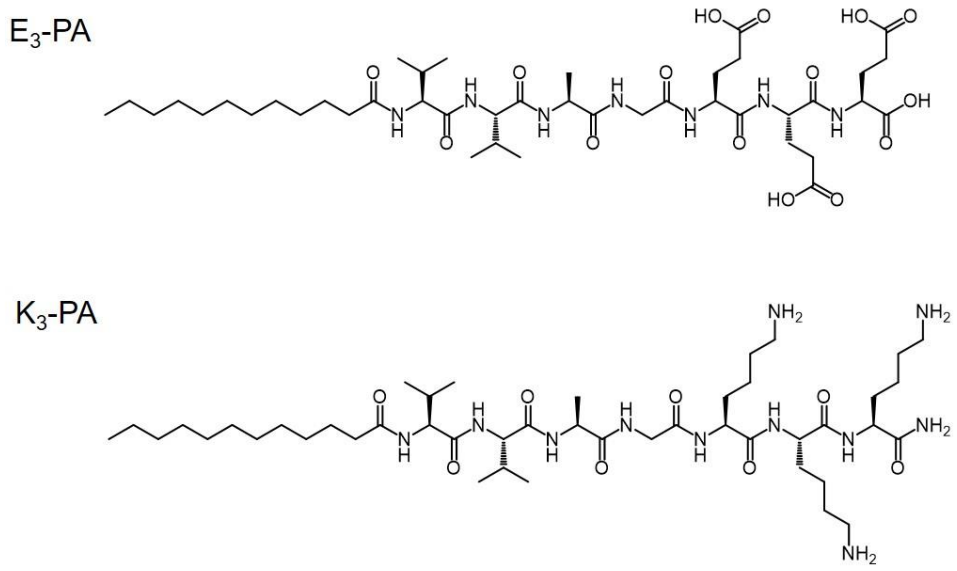

Figure 3.1 Chemical representations of Lauryl-VVAGEEE (E_3-PA), and Lauryl-VVAGKKK-Am (K_3-PA).

Positively charged K_3-PA was utilized to induce self-assembly when mixed with negatively charged E_3-PA molecules at physiological conditions. The PA molecules were characterized by LC-MS and purified by preparative HPLC (Figures 3.2-3.5). The formation of a porous nanofiber network resembling natural ECM was shown by SEM imaging (Figure 3.6).

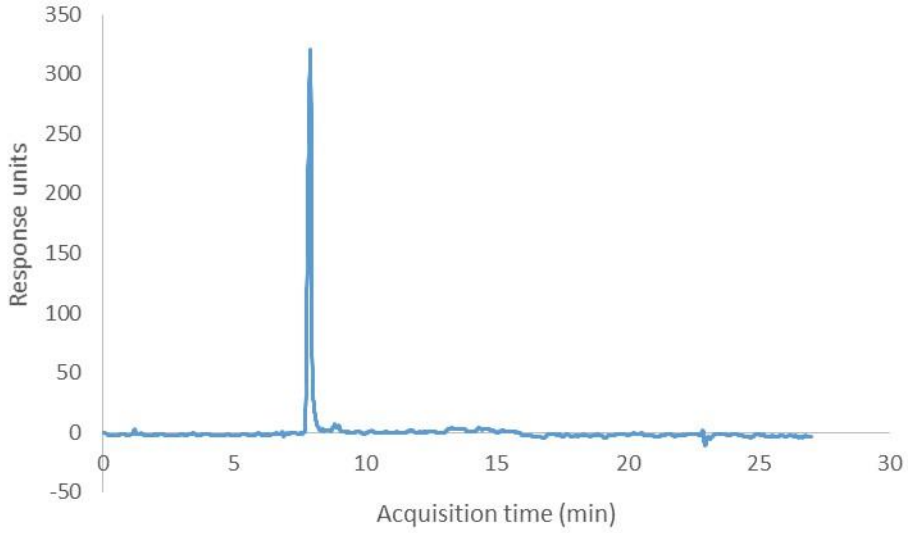

Figure 3.2 RP-HPLC chromatogram of E_3-PA, the change of response units with respect to time at 220 nm.

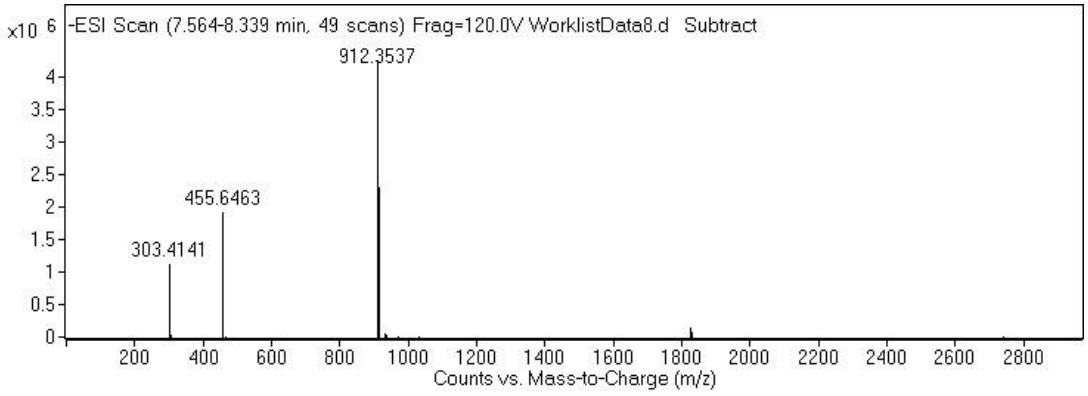

Figure 3.3 $[M-H]^-$ (calculated): 912.50, $[M-H]^-$ (observed): 912.35; $[M/2-H]^-$ (calculated): 455.75, $[M/2-H]^-$ (observed): 455.64; $[M/3+H]^+$ (calculated): 303.16, $[M/3+H]^+$ (observed): 303.41.

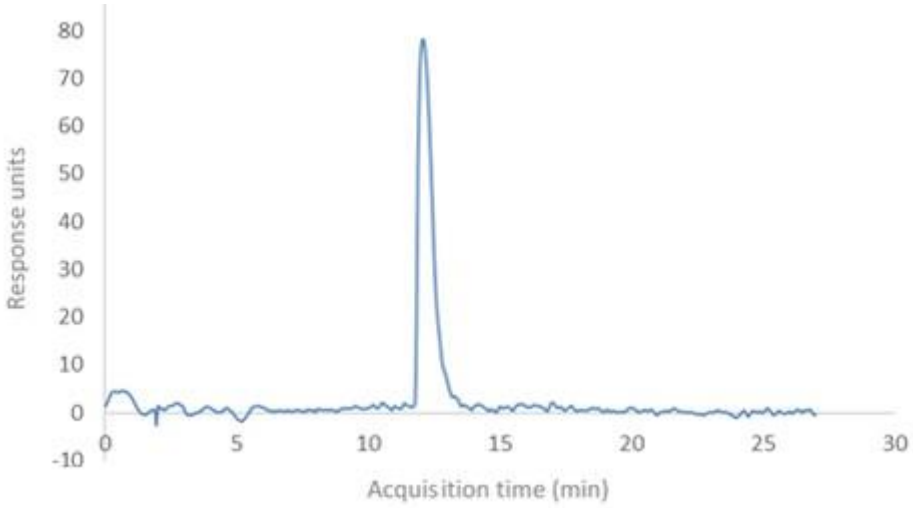

Figure 3.4 RP-HPLC chromatogram of K_3-PA, the change of response units with respect to time at 220 nm.

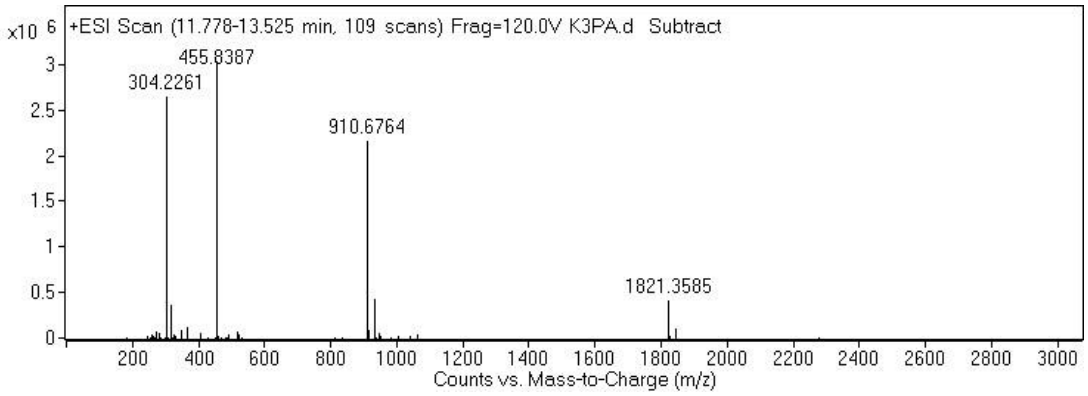

Figure 3.5 $[M+H]^+$ (calculated): 910.67, $[M+H]^+$ (observed): 910.67; $[M/2+H]^+$ (calculated): 455.83, $[M/2+H]^+$ (observed): 455.83; $[M/3+H]^+$ (calculated): 304.22, $[M/3+H]^+$ (observed): 304.22; $[2M+2H]^{+2}$ (calculated): 1821.34, $[2M+2H]^{+2}$ (observed): 1821.35.

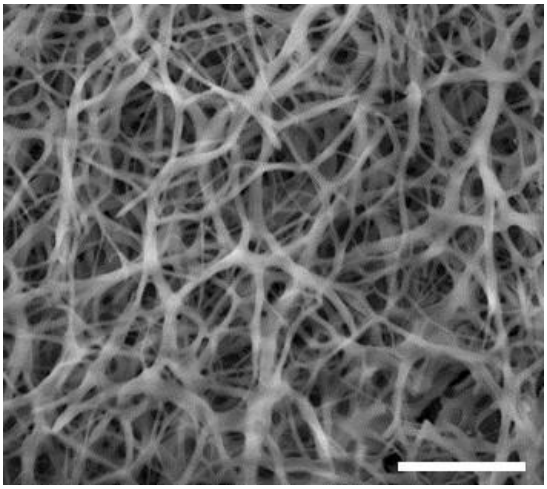

Figure 3.6 SEM image of E_3/K_3-PA nanofibers. Scale bar is 2 µm.

CD measurements of self-assembled PA nanofibers suggested a predominance of β-sheets with a chiral absorbance at 220 nm in the E_3/K_3-PA mixture, while individual PA molecules did not show β-sheet signal (Figure 3.7).

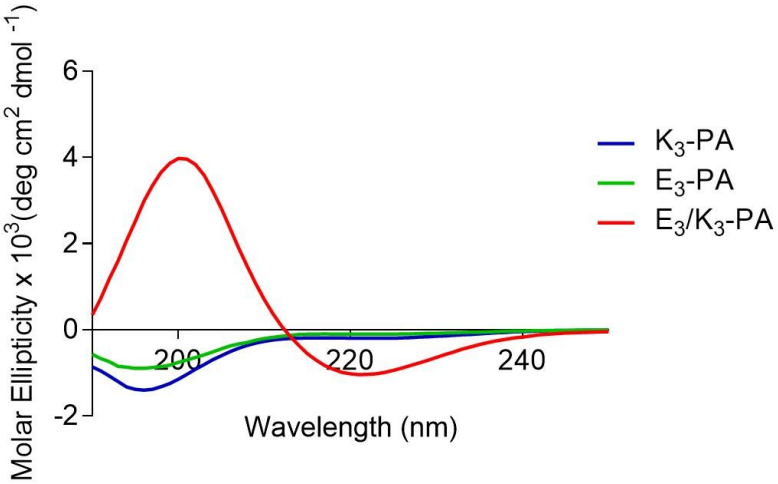

Figure 3.7 Circular dichroism (CD) spectroscopy characterization of peptide amphiphile molecules (E_3-PA and K_3-PA) and nanofibrous peptide assemblies (E_3/K_3-PA).

3.3.2 Cell Behavior and Viability on PA Nanofibers

The effect of E_3/K_3-PA nanofibers on the viability of rMSCs was tested by calcein AM staining at 24 h (Figure 3.8). The rMSCs were viable on all surfaces over this period. We did not observe any significant difference between the viability of cells on peptide nanofiber scaffolds, gelatin-coated and bare TCP (Figure 3.8). These results showed that peptide nanofibers provide a biocompatible environment and are not toxic to cells.

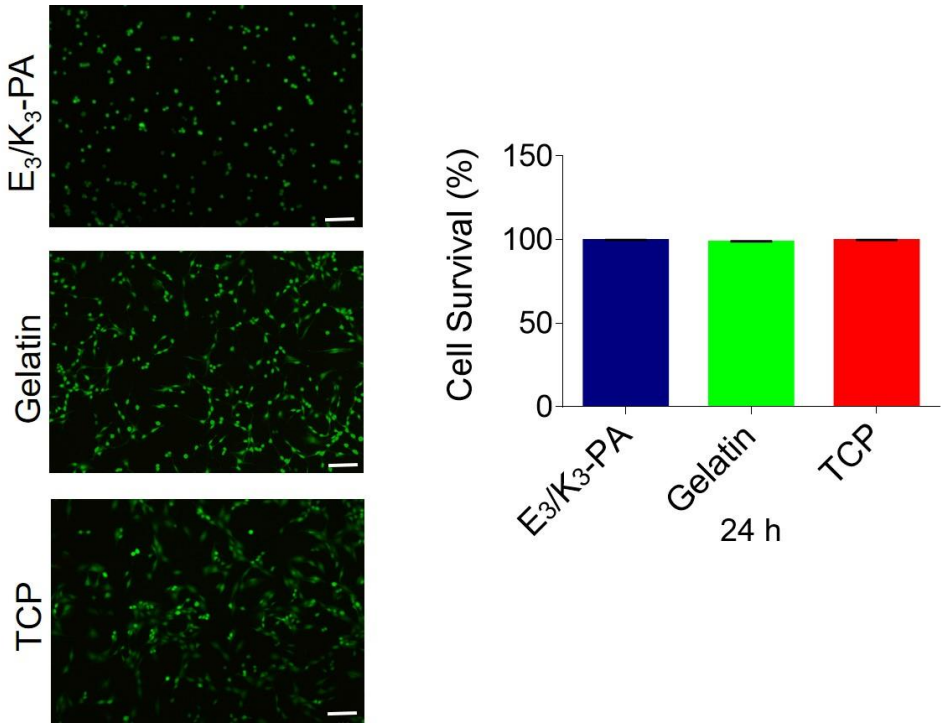

Figure 3.8 Viability of rMSCs cultured on PA coated, gelatin coated and uncoated surface (TCP), as analyzed by calcein-ethidium homodimer live−dead assay. Scale bars are 100 μm.

Cytoskeletal arrangement of rMSCs on E_3/K_3-PA, gelatin-coated and bare glass surfaces were investigated by phalloidin/TO-PRO-3 staining. Cells adhered on both glass surfaces and peptide nanofibers, and formed cytoskeletal attachments under both

culture conditions. However, from day 7 onward, cells on E_3/K_3-PA nanofibers were found to cluster together and form bone-like nodules (Figure 3.9).

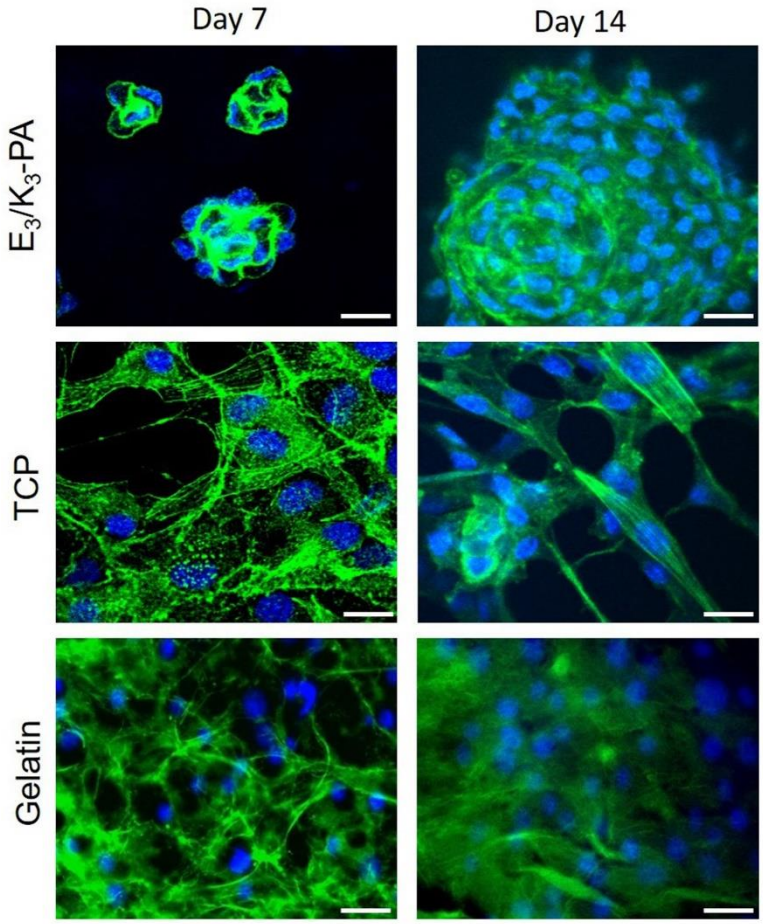

Figure 3.9 F-actin filaments stained with phalloidin (green), showing actin networks formed by rMSCs on PA nanofibers, gelatin-coated and bare TCP. Nuclei were stained with TO-PRO-3 reagent (blue). Scale bars are 20 μm.

3.3.3 Molecular Analysis of Osteogenic Differentiation Markers

ALP activity is an important early marker of osteogenic differentiation and ALP enzyme functions in releasing inorganic phosphate units from pyrophosphate as a source of biomineralization [31]. We tested the ALP activity of rMSCs cultured on E_3/K_3-PA, gelatin-coated and TCP surfaces after 3, 7 and 14 days of incubation in

osteogenic medium. All groups demonstrated a characteristic pattern of ALP activity (Figure 3.10), such that an initial increase in ALP production during early differentiation was followed by a subsequent decrease in later stages. rMSCs cultured on E_3/K_3-PA showed significantly higher ALP activity compared to gelatin and TCP groups. Maximum ALP activity was observed on day 3 for E_3/K_3-PA and gelatin groups, which was found to gradually decrease at days 7 and 14 (Figure 3.10). ALP activity of cells on TCP was minimal on day 3 and reached its maximum level on day 7 (Figure 3.10).

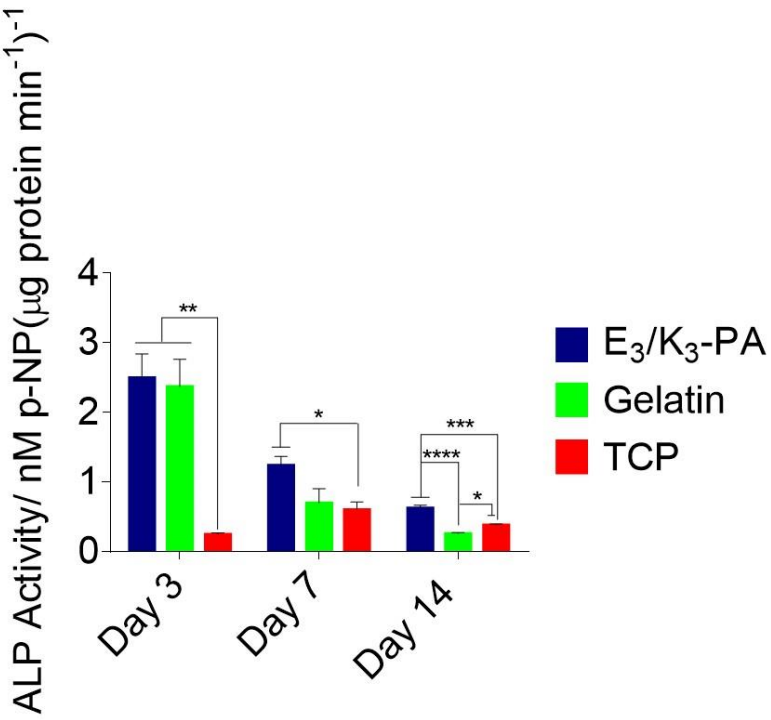

Figure 3.10 Effect of E_3/K_3-PA nanofibers on ALP activity of rMSCs on days 3, 7 and 14 of osteogenic differentiation.

In addition to ALP expression patterns, the osteogenic differentiation of MSCs is accompanied by the sequential expression of a series of genetic markers [154]. To understand whether rMSCs commit to the osteogenic lineage on the E_3/K_3-PA

nanofiber system, gene expression profiles of cells cultured on E_3/K_3-PA-coated, gelatin-coated and bare surfaces were analyzed and quantified. Expressions of the osteogenic markers Runt-related transcription factor 2 (Runx2), type I collagen (collagen I) and osteopontin were studied on days 3, 7 and 14. Runx2 is often referred to as the key regulator of osteogenic differentiation [181, 182] and its expression is usually analyzed during the early phases of osteogenic differentiation. The expression of Runx2 was upregulated when rMSCs were cultured on E_3/K_3-PA nanofibers and gelatin-coated wells compared to cells on bare TCP surfaces on day 3 (Figure 3.11).

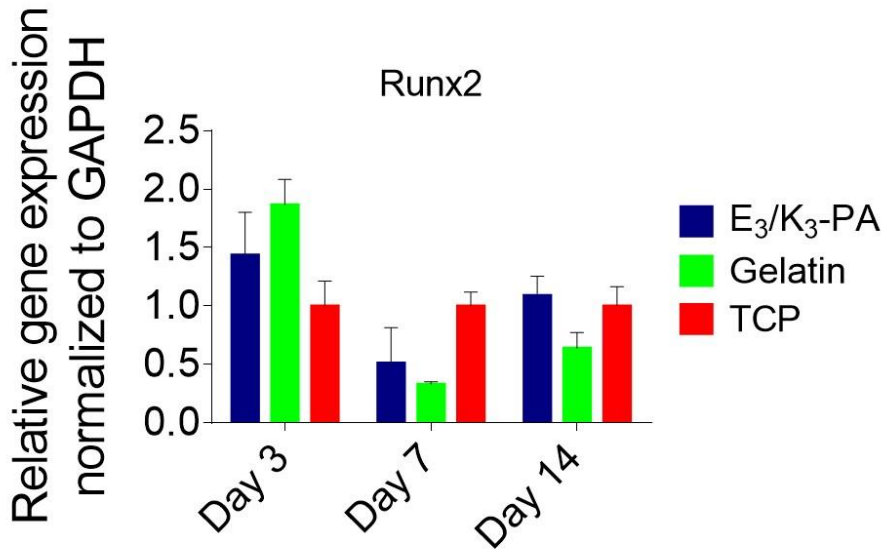

Figure 3.11 Gene expression analysis of Runx2 on days 3, 7 and 14.

Also found at an early stage is the expression of a collagen matrix, which can act as a template for mineralization [158, 183]. Collagen I expression was significantly upregulated in cells cultured on E_3/K_3-PA nanofibers compared to gelatin-coated wells and bare TCP, exhibiting an enhancement of ~3.4 folds on day 7 (Figure 3.12). In addition to collagen I, several non-collagenous proteins have crucial roles in the formation and maturation of mineralized tissues. Osteopontin is one of the most

notable among these proteins and is expressed at high levels during the late stages of osteogenic differentiation. Here, osteopontin expression of cells on E_3/K_3-PA nanofibers was also significantly higher compared to gelatin-coated wells on days 7 and 14 by ~18.8 and ~5.8 folds, respectively (Figure 3.13). The expression of osteopontin was also enhanced by ~4.14 and ~2.9 folds on days 7 and 14, respectively, on E_3/K_3-PA nanofibers compared to TCP (Figure 3.13). Overall, ALP analysis and gene expression profiles show that, although MSCs differentiate into osteogenic lineage on both gelatin and E_3/K_3-PA nanofibers, enhanced osteogenic differentiation was observed on E_3/K_3-PA surfaces.

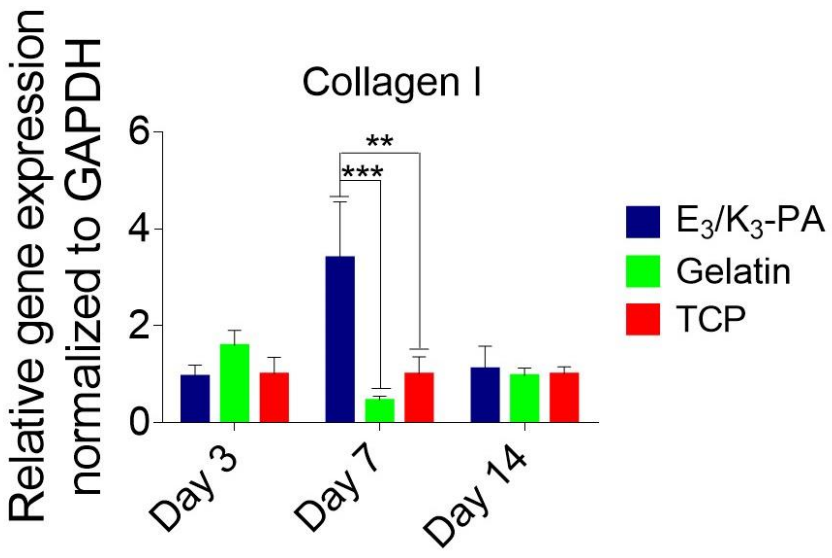

Figure 3.12 Gene expression analysis of collagen I on days 3, 7 and 14.

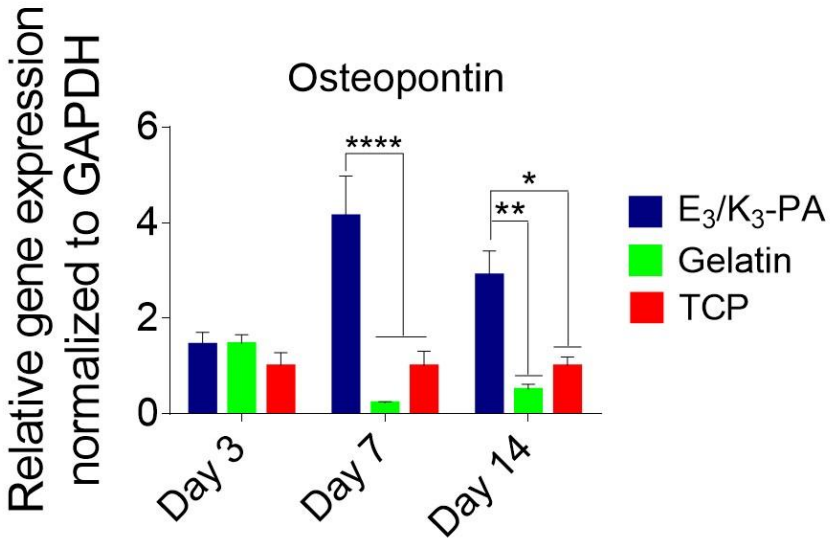

Figure 3.13 Gene expression analysis of osteopontin on days 3, 7 and 14.

3.3.4 Mineralization on Bioactive Peptide Nanofibers

Biomineralization is an important component of osteogenic differentiation and osteoblasts are the major cells that carry out the synthesis, deposition and mineralization of the extracellular matrix of bone [184]. A vital phase of biomineralization involves the deposition of calcium and phosphate [154, 156]. Calcium deposits can specifically be stained using Alizarin red S, which chelates Ca^{2+} and is a commonly used dye for the evaluation of bone mineralization [156, 157]. In this study, the visible mineralization of cells on E_3/K_3-PA peptide nanofibers in the presence of osteogenic supplements started on day 7, where quantitative analysis of relative calcium deposition showed a significant increase ($p < 0.0001$) compared to gelatin and TCP groups (Figure 3.14). Cells cultured on E_3/K_3-PA nanofibers showed early matrix mineralization with extensive Alizarin red staining on days 7 and 14, compared to gelatin and TCP groups which exhibited significantly less staining (Figure 3.15). No staining was observed on scaffolds without cells (Figure 3.16). These results show that mineralization in induced in rMSCs cultured on peptide nanofibers.

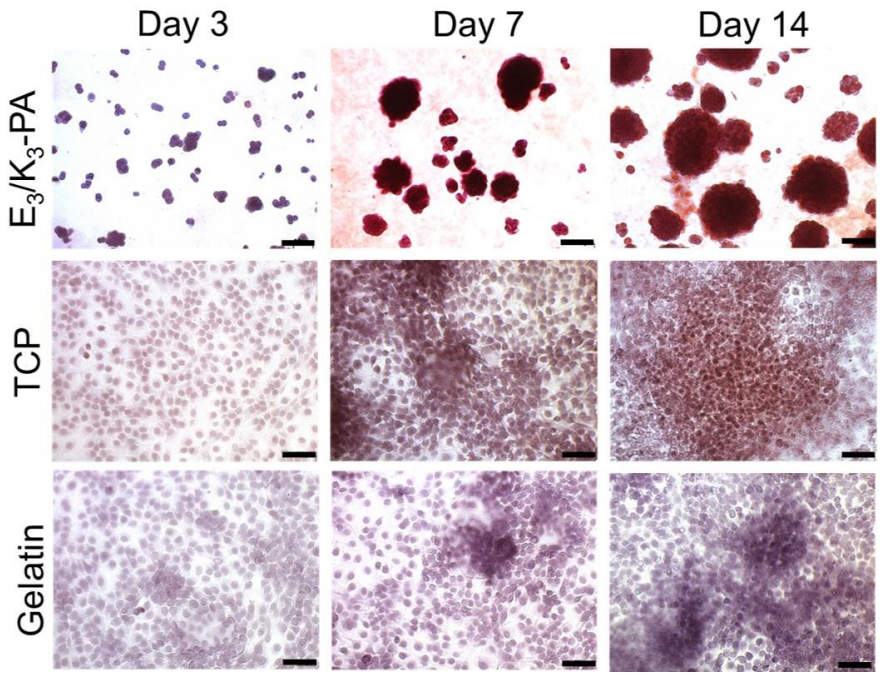

Figure 3.14 Alizarin red staining of rMSCs on PA coated, gelatin coated and uncoated TCP surfaces on days 3, 7 and 14. Scale bars are 100 μm.

While MSCs do not deposit extracellular calcium, osteoblasts are known to secrete remarkable amounts of extracellular calcium deposits [158]. In this study, cells cultured on E_3/K_3-PA peptide nanofibers showed higher matrix mineralization upon differentiation, suggesting that they were rapidly and effectively committed to the osteogenic lineage (Figures 3.14 and 3.15). On the other hand, gelatin-coated and bare TCP group exhibited a considerably lower capacity for osteogenic differentiation. rMSCs on E_3/K_3-PA peptide nanofibers showed early calcium deposition on day 7 (Fügure 3.15), which may be due to the effect of E_3-PA on the early maturation of osteoblasts [179]. This may be due to the presence of negatively-charged glutamic acid residues that strongly bind calcium ions that induce the biomineralization process.

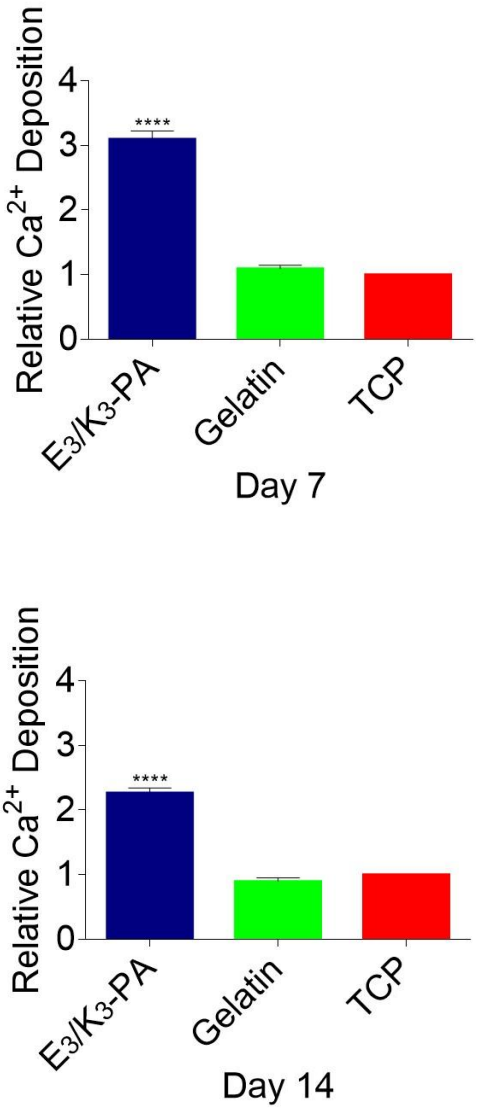

Figure 3.15 Quantification of Ca^{2+} deposition on PA coated, gelatin coated and uncoated TCP surfaces on days 7 and 14, $^{**}p < 0.01$, $^{***}p < 0.001$.

During intramembranous ossification, MSCs proliferate and reorganize into cell aggregates, which results in the formation of primary bone nodules. Following their integration into bone nodules, MSCs may subsequently differentiate into osteoprogenitor cells and finally into osteoblasts [144]. Phalloidin staining was used to determine whether this effect occurs in rMSCs on E_3/K_3-PA nanofibers, and cells

were observed to aggregate into bone nodule-like structure from day 7 onwards (Figure 3.9).

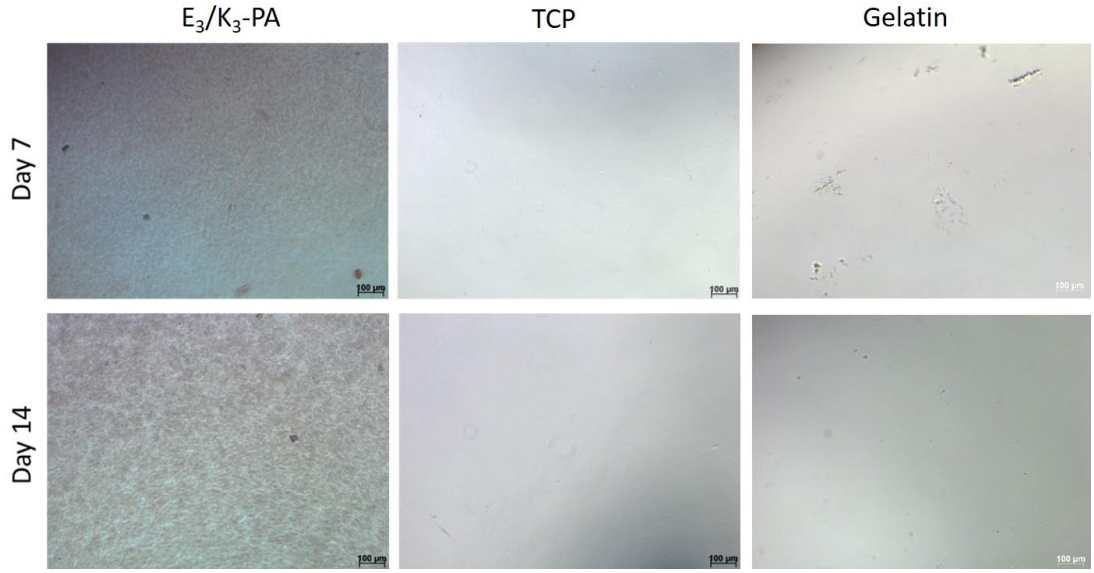

Figure 3.16 Alizarin red staining of E_3/K_3-PA nanofibers, gelatin-coated and bare TCP (samples without cells) after 7 and 14 days of incubation in osteogenic medium. No staining was observed on E_3/K_3-PA nanofibers, gelatin-coated or bare TCP. Scale bars are 100 µm.

3.4 Conclusion

In summary, we have demonstrated that self-assembled nanofiber scaffolds formed by PA molecules exhibiting a triple glutamic acid motif enhanced the biomineralization and osteogenic differentiation of rMSCs. The rMSCs cultured on these peptide nanofibers exhibited enhanced alkaline phosphatase activity, calcium deposition, and osteogenic gene expression, which are the main indicators of bone-like mineralization. In further studies, this PA system can be used and improved to investigate the changes in cell mechanical properties during osteogenic differentiation.

Chapter 4

4. Mineralized Peptide Nanofiber Gels for the Promotion of Osteogenic Differentiation

4.1 Introduction

In nature, biological organisms construct a diverse range of highly specialized organic-inorganic hybrid materials, such as bone, teeth, and shells, for purposes such as muscle attachment, predator defense and protection against environmental stresses. Living organisms produce these inorganic materials through the biomineralization process, and mineralized structures differ in terms of their mineral composition, morphologies, properties, and functions. Among these, the most well-known examples are calcium phosphate minerals, which are found in vertebrate bones and teeth and exist in different compositions depending on factors such as tissue type, location, age, injury status and diet [185, 186].

The fabrication of organic-inorganic hybrid materials through controlled mineralization processes similar to those found in nature has recently gained importance, since these structures can provide further insight into the mechanisms of the biomineralization process and assist in the development of more effective biomimetic materials [187]. In order to produce synthetic matrices incorporating both the organic and inorganic components of native bone tissue, several groups have constructed composite/hybrid biomaterials with the help of an organic template mineralization process that emulates several features of natural biomineralization [188-191]. In particular, calcium phosphate-based minerals have been used as

osteoinductive substrates [192, 193] and shown to promote osteogenic differentiation of progenitor cells *in vitro* [194-200]. These matrices could be incorporated into load-bearing metallic materials to repair fractures and rebuild joints through the effective integration of the implant with the surrounding bone matrix.

In this study, we report the design and fabrication of a mineralized peptide nanofiber gel that can potentially be employed in orthopedic implant applications. A negatively-charged peptide amphiphile molecule was used to emulate the charge-mediated mineralization process that is found in bones and teeth, and a cationic solution ($CaCl_2$) was used prior to mineralization to trigger the self-assembly of peptide amphiphile molecules. $(NH_4)_2HPO_4$ was then used to facilitate the formation of calcium phosphate biominerals on the peptide scaffold template. The PA hydrogel formation and mineralization processes were investigated by scanning electron microscopy (SEM), transmission electron microscopy (TEM), X-ray diffractometry (XRD) and oscillatory rheology; and rheological measurements showed that mineralization enhanced the mechanical stiffness of gels. In addition, we investigated the osteogenic differentiation of Saos-2 cells on a hydroxyapatite (HA) coated E_3-PA system to determine the potential applications of our biomineralized scaffold in regenerative medicine. Within 14 days, Saos-2 cells on HA coated peptide nanofibers exhibited higher alkaline phosphatase (ALP) activity and increased mRNA expression of Runx2, collagen I and osteocalcin compared to cells on non-mineralized peptide nanofibers and tissue culture plate, suggesting that mineralization-inducing peptides could be used as osteoinductive materials.

4.2 Experimental Section

4.2.1 Materials

All protected amino acids, lauric acid, Fmoc-Glu(OtBu)-Wang resin (100-200 mesh), HBTU and DIEA were purchased from Novabiochem ABCR or Sigma-Aldrich. Calcein-AM and other cell culture materials were obtained from Invitrogen or Thermo-Fisher. All other chemicals and materials used in this study were purchased from Thermo-Fisher, Merck, Alfa Aesar or Sigma-Aldrich.

4.2.2 Synthesis and Characterization of Peptide Amphiphiles (PAs)

Lauryl-Val-Val-Ala-Gly-Glu-Glu-Glu-OH (E_3-PA) was synthesized with Fmoc solid phase peptide synthesis method. Fmoc-Glu(OtBu)-Wang resin (100-200 mesh) (Novabiochem) served as the solid support. Amino acid couplings were carried out with 2 molar equivalents of Fmoc-protected amino acid, 1.95 molar equivalents of HBTU, and 3 molar equivalents of DIEA for 2 h. Fmoc groups were removed at each coupling step with 20% piperidine/DMF for 20 min. 10% acetic anhydride-DMF solution was used to block the unreacted amine groups after each coupling step. Cleavage of protecting groups and peptide molecules from the solid support was carried out by TFA cleavage cocktail (95% TFA, 2.5% water, 2.5% triisopropyl silane) for 3 h. Excess TFA was removed by rotary evaporation. Synthesized E_3-PA was then precipitated in diethyl ether overnight. The precipitate was collected by centrifugation and dissolved in ultra-pure water. This solution was frozen at -80 °C followed by lyophilization. The purity of the peptide amphiphile was assessed using an Agilent 6530 quadrupole time of flight (Q-TOF) mass spectrometer equipped with an electrospray ionization (ESI) source and a reverse-phase analytical high performance liquid chromatography (HPLC) system. Synthesized E_3-PA was purified with a

preparative HPLC system (Agilent 1200 series). E_3-PA was then freeze-dried and reconstituted in ultrapure water at pH 7.4 before use.

4.2.3 Preparation of Mineralized Hydrogels

Stock solutions of diammonium phosphate ($(NH_4)_2HPO_4$) and calcium chloride ($CaCl_2$) were prepared in ultra-pure water. E_3-PA was also dissolved in ultra-pure water at neutral pH at a 1% (w/v) concentration. Self-assembled scaffolds were prepared by pipetting the negatively-charged E_3-PA solution on a silicon wafer and adding positively-charged $CaCl_2$ to trigger charge neutralization-based gel formation behavior. The mixture was incubated for 30 min to obtain a thermodynamically stable gel, and a mineralized peptide nanofiber system was obtained by adding $(NH_4)_2HPO_4$ dropwise following the incubation period. The volumetric ratio of $CaCl_2$ and $(NH_4)_2HPO_4$ to E_3-PA was set as 1:1 within the mineralized hydrogels.

4.2.4 Transmission Electron Microscopy (TEM)

The samples were prepared and mineralized on carbon-coated TEM grids. A drop of aqueous peptide amphiphile (0.05% w/v) was mounted on the holey grid, 5 mM of $CaCl_2$ and 5 mM of $(NH_4)_2HPO_4$ solutions were dropped onto the grid at a 1:10 (v/v) ratio, and the mixture was incubated for several minutes to obtain calcium phosphate minerals. Then, TEM imaging was performed with a FEI Tecnai G2 F30 transmission electron microscope at 300 kV.

4.2.5 X-Ray Diffraction (XRD) Analysis

In order to determine the presence and type of minerals on the peptide scaffolds, XRD spectra of mineralized and non-mineralized PAs were obtained with a Panalytical X'pert Pro Multi-Purpose X-Ray Diffractometer. A total volume of 560 μL of gel was

prepared by mixing E_3-PA, $CaCl_2$ and $(NH_4)_2HPO_4$ at a ratio of 1:10:10, respectively. The samples were immersed into liquid nitrogen, lyophilized, and powdered prior to XPS measurements. Two control samples (E_3-PA/HCl, prepared by substituting HCl instead of $CaCl_2$ during hydrogel preparation, and E_3-PA/$CaCl_2$, prepared by substituting omitting $(NH_4)_2HPO_4$ to prevent the formation of calcium phosphate) were also measured in order to determine the differences between mineralized and non-mineralized peptide nanofibers.

4.2.6 Oscillatory Rheology

Mechanical properties of mineralized PAs were characterized by oscillatory rheology measurements on an Anton Paar Physica RM301 Rheometer. For sample preparation, 250 µL of (1% w/v) E_3-PA was placed on the plate of the rheometer, 25 µL of $CaCl_2$ solution was added dropwise in order to produce self-assembled peptide nanofibers, and 25 µL of $(NH_4)_2HPO_4$ solution was then added to obtain calcium phosphate minerals. All measurements were carried out at room temperature. Time-dependent rheology was used to determine the gelation kinetics of the mineralized and non-mineralized peptide nanofibers. Strain and angular frequency were held constant at 0.01% and 10 rad s^{-1}, respectively, during the time-sweep test.

4.2.7 Cell Culture and Maintenance

Saos-2 cells (human osteosarcoma cell line, ATCCR HTB-85TM) were used in all cell culture experiments at passage numbers between 20-25. Cells were cultured in 75 cm^2 flasks at 37 °C in a humidified incubator and supplied with 5% CO_2. Saos-2 cells were maintained in low glucose Dulbecco's Modified Eagle's Medium (DMEM) with L-glutamine, supplemented with 10% fetal bovine serum (FBS) and 1% penicillin/streptomycin. All cell experiments were carried out after the cells reached

90% confluency. The culture medium was changed every 3-4 days. Alkaline phosphatase activity (ALP) assay and gene expression analyses were performed in both osteogenic medium and maintenance medium (control group). In the osteogenic medium group, the cell medium was replaced with osteogenic medium (DMEM with 10% FBS supplemented with 10 mM β-glycerophosphate, 50 μg mL^{-1} ascorbic acid and 10 nM dexamethasone) after the seeded cells had reached confluency.

4.2.8 Viability Assay

The viability of Saos-2 cells incubated on mineralized PA nanofibers, non-mineralized PA nanofibers and bare tissue culture plates (TCP) was studied by Live/Dead Assay (Invitrogen). Briefly, cells were seeded on mineralized PA nanofibers, non-mineralized PA nanofibers and bare 96-well tissue culture plates at a density of 5 x 10^3 cells/well. After 24 h of incubation, cell medium was discarded, and cells were washed with phosphate buffered saline (PBS) and incubated with 2 μM calcein-AM and 2 μM EthD-1 in PBS for 30 min at room temperature. After incubation, images were taken at three random points per well with a fluorescence microscope (Zeiss, Axio Scope A1) at 100x magnification. All samples were analyzed in triplicate. Live and dead cells were counted by using Image J.

4.2.9 Actin Staining of Saos-2 Cells on Mineralized PA Nanofibers

Cells were seeded on top of mineralized PA nanofiber-coated, non-mineralized PA nanofiber-coated and uncoated surfaces at a density of 4 × 10^4 cells per 13 mm coverslip. After 3 days of culture, phalloidin/TO-PRO-3 staining was performed to evaluate the differences in cytoskeletal organization. Before staining, cells were fixed with 4% formaldehyde for 15 min and permeabilized with 0.1% Triton-X for 10 min at room temperature. Samples were incubated with 3% (w/v) bovine serum albumin

(BSA)/PBS for 30 min for blocking. Actin filaments of the cells were initially stained with 1:500 diluted FITC-conjugated phalloidin (Thermo Fisher) in 3% (w/v) BSA/PBS for 20 min. After serial washing steps, samples were stained with 1:1000 diluted TO-PRO-3 (Thermo Fisher) or 1:3000 diluted DAPI (Thermo Fisher) for 20 min for the visualization of nuclei. Coverslips were mounted with Prolong Gold Antifade Reagent (Invitrogen). Cytoskeletal organizations of cells were observed using a Zeiss LSM 510 confocal microscope at 630x magnification.

4.2.10 Cell Adhesion Assay

Cell adhesion experiments were performed under serum-free conditions. Cells were incubated for 1 h in serum free DMEM medium supplemented with 4 mg/mL bovine serum albumin (BSA) and 50 μg/mL cycloheximide at standard culture conditions before seeding. After 1 h, cells were removed from tissue culture plate by trypsinization and seeded onto the coated 96 well plates. After 4 h of incubation in serum-free medium at standard culture conditions, Calcein AM (Invitrogen) staining (2 μM) was performed for 40 min according to the manufacturer's instructions. Cell adhesion was quantified directly by counting the number of cells using ImageJ program from fluorescent microscopy images. Images were taken from 5 different random locations per well, and the experiment was carried out with n = 5. Results were then normalized to tissue culture plate counts.

4.2.11 Cell Proliferation Assay

Proliferation of cells on coatings was assessed using BrdU assay (Roche). Cells were seeded onto PA-coated wells and uncoated tissue culture plates (TCP) at a density of 3×10^3 cells/well. Cells were incubated in standard cell culture medium supplemented with 100 μM BrdU labeling solution for 24 h and 72 h. At the end of the incubation

period, BrdU incorporation assay was performed according to the manufacturer's instructions. Briefly, cells were fixed with FixDenat for 30 min and anti BrdU-POD solution was added into wells. Following 90 min of incubation and subsequent tapping, substrate solution was added into wells and proliferation rates of the cells were quantified by measuring their absorbance (370 nm, with 492 nm reference wavelength) with a microplate reader.

4.2.12 Alkaline Phosphatase (ALP) Activity Assay

In order to measure the ALP activity of Saos-2 cells, degradation of *p*-nitrophenol through endogenous ALP activity was quantified after 3, 7 and 14 days of culture in maintenance medium and osteogenic medium. Briefly, cells were seeded on mineralized PA nanofiber-coated, non-mineralized PA nanofiber-coated and uncoated (bare TCP) surfaces of 48-well plates at a density of 2×10^4 cells per well and the cell medium was replaced with osteogenic medium after the cells had reached confluency. Cells were rinsed with PBS at predetermined time points. M-PER protein extraction kit (Thermo) with 5% protease inhibitor solution was used to extract proteins. Pierce BCA protein assay (Thermo) was performed to quantify the amount of proteins obtained from the cells according to the manufacturer's protocol. To measure ALP activity, 50 µL of the protein sample was incubated with 150 µL of *p*-nitrophenol phosphate substrate in 96-well plates for 30 min on a shaker. Serial dilutions of *p*-nitrophenol in 0.25 M NaOH solution were used as standards. Finally, the optical density of the samples was determined at 405 nm using a Spectramax M5 microplate reader and ALP results were normalized to the amount of total proteins at each time point tested.

4.2.13 Gene Expression Analysis

For gene expression studies, Saos-2 cells were seeded on mineralized PA nanofiber-coated, non-mineralized PA nanofiber-coated and uncoated (bare TCP) surfaces of 6 well plates at a density of 2.5 x 10^5 cells per cm^2. After cells had reached confluency, their media were replaced with osteogenic medium, and gene expression profiles of Runx2, collagen I and osteocalcin were evaluated by quantitative RT-PCR (qRT-PCR) analysis to investigate the osteogenic differentiation process. RNA isolation from Saos-2 cells seeded on mineralized PA nanofiber-coated, non-mineralized PA nanofiber-coated and uncoated surfaces was performed by using TRIzol (Invitrogen) according to the manufacturer's instructions after 3, 7 and 14 days of incubation. Yield and purity of extracted RNAs were assessed by Nanodrop 2000 (Thermo Scientific). Samples were diluted to a concentration of 100 ng/μL prior to their use. Primers for PCR amplification of Runx2, collagen I, osteocalcin and GAPDH are shown in Table 4.1. cDNA synthesis from RNA and qRT-PCR were performed using SuperScript III Platinum SYBR Green One-Step qRT-PCR Kit according to the manufacturer's instructions. mRNA levels were calculated and normalized to GAPDH according to comparative Ct method for each target gene [178].

Table 4.1 Primers used for qRT-PCR expression analysis

Gene	Primer Sequence:Forward/Reverse
GAPDH	5’- TCGACAGTCAGCCGCATCTTCT-3’
	5’-GTGACCAGGCGCCCAATACGAC-3’
Runx2	5'-TCTGGCCTTCCACTCTCAGT-3'
	5'-GACTGGCGGGGTGTAAGTAA-3'
Collagen I	5'-GAGAGCATGACCGATGGATT-3'
	5'-CCTTCTTGAGGTTGCCAGTC-3'
Osteocalcin	5’-CACCGAGACACCATGAGAGC -3’
	5’-GTGGTCAGCCAACTCGTCAC -3’

4.3 Results and Discussion

4.3.1 Peptide Synthesis and Characterization

It is known that electrostatic interactions between noncollagenous proteins and crystals regulate the process of bone mineralization [201, 202]. Indeed, nature employs proteins with negatively charged residues in the biomineralization processes [203-206]. Consequently, we designed a negatively-charged peptide amphiphile (E_3-PA) to prepare mineralized peptide nanofibers in this study (Figure 4.1).

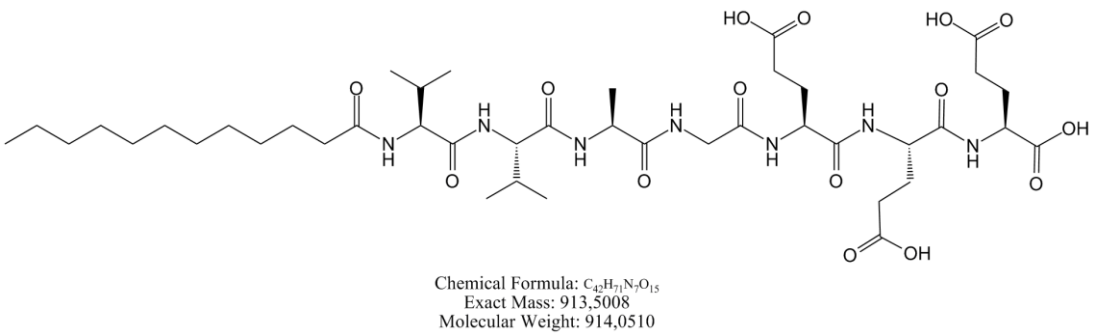

Figure 4.1 Chemical representation of Lauryl-VVAGEEE (E_3-PA).

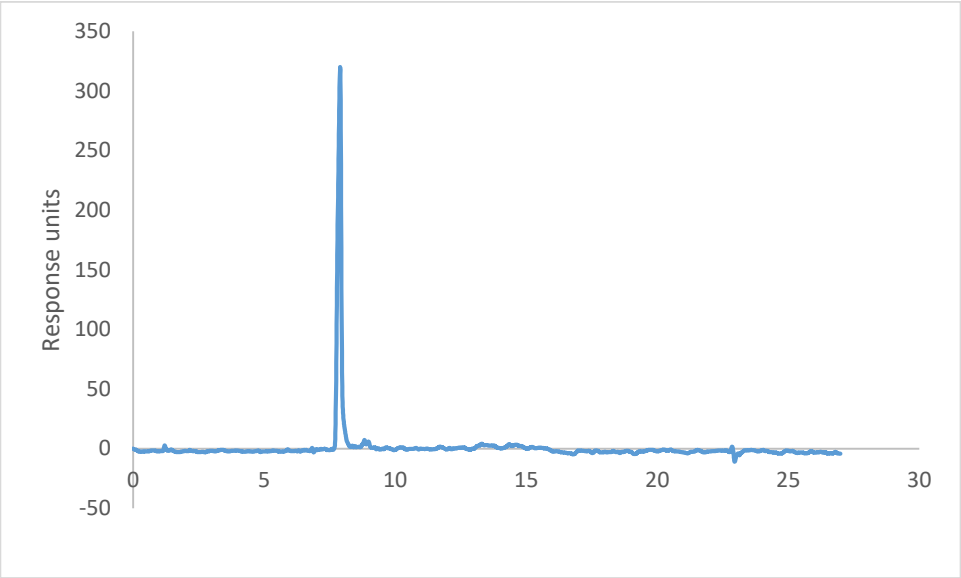

Figure 4.2 RP-HPLC chromatogram of E_3-PA, the change of response units with respect to time at 220 nm.

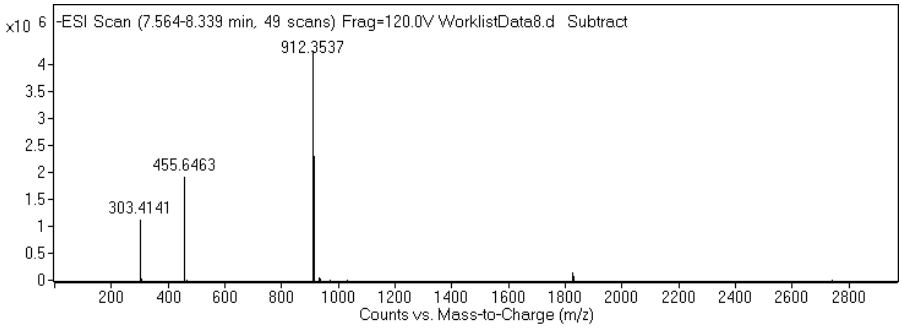

Figure 4.3 $[M-H]^-$ (calculated):912.50, $[M-H]^-$ (observed):912.35; $[M/2-H]^-$ (calculated): 455.75, $[M/2-H]^-$ (observed): 455.64; $[M/3+H]^+$ (calculated): 303.16, $[M/3+H]^+$ (observed): 303.41.

This peptide amphiphile molecule, lauryl-VVAGEEE-OH, contains an alkyl chain, a short linker sequence of hydrophobic amino acids and a head region of negatively charged amino acids. It was used as an organic template for the synthesis of calcium phosphate biominerals. The identity and purity of E_3-PA were assessed by LC-MS

(Agilent 6530−1200 Q-TOF) analysis (Figure 4.2 and Figure 4.3).

4.3.2 Morphology of Mineralized PA Nanofibers

Following the chemical characterization of peptide amphiphiles, nanofiber formation and the nucleation of the minerals on scaffold surfaces were observed by TEM images (Figure 4.4). TEM images showed the nucleation of the minerals on scaffold surfaces following their interaction with Ca^{2+} ion-decorated peptide amphiphile nanofibers for 30 min (Figure 4.4b). When the duration of mineralization on gels was increased to 90 min, plate-like crystals were observed to have developed on peptide amphiphile nanofibers, corresponding to the formation of hydroxyapatite minerals (Figure 4.4c) [191, 207].

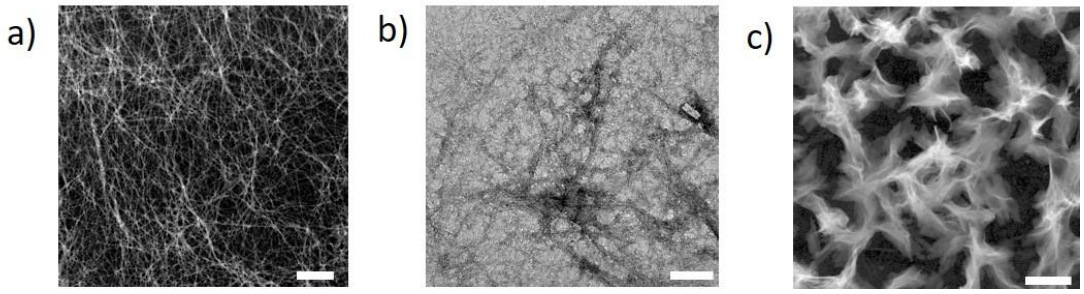

Figure 4.4 TEM images of formation of plate-like hydroxyapatite crystals in the presence of peptide amphiphile molecules. (a) Peptide nanofibers in the absence of minerals (scale bar is 250 nm), (b) calcium phosphate mineralization after 30 min of incubation (scale bar is 100 nm) and (c) calcium phosphate mineralization after 90 min of incubation (scale bar is 50 nm).

4.3.3 Characterization of Mineral Type on Mineralized PA Nanofibers

X-ray diffractometry (XRD) was performed in order to determine the type of the minerals that are deposited on the surfaces of peptide amphiphile nanofibers. The

mineralized peptide amphiphile nanofibers showed the characteristic peaks of hydroxyapatite [190, 208]. Indeed, the diffraction peaks at (211), (300) and (004) match with the expected peaks of HA (Figure 4.5). On the other hand, non-mineralized peptide amphiphile nanofibers did not show any characteristic peaks corresponding to HA (Figure 4.6). In addition, peaks corresponding to trace amounts of NaCl were observed even after five times of washing prior to the preparation of XRD samples (Figure 4.7).

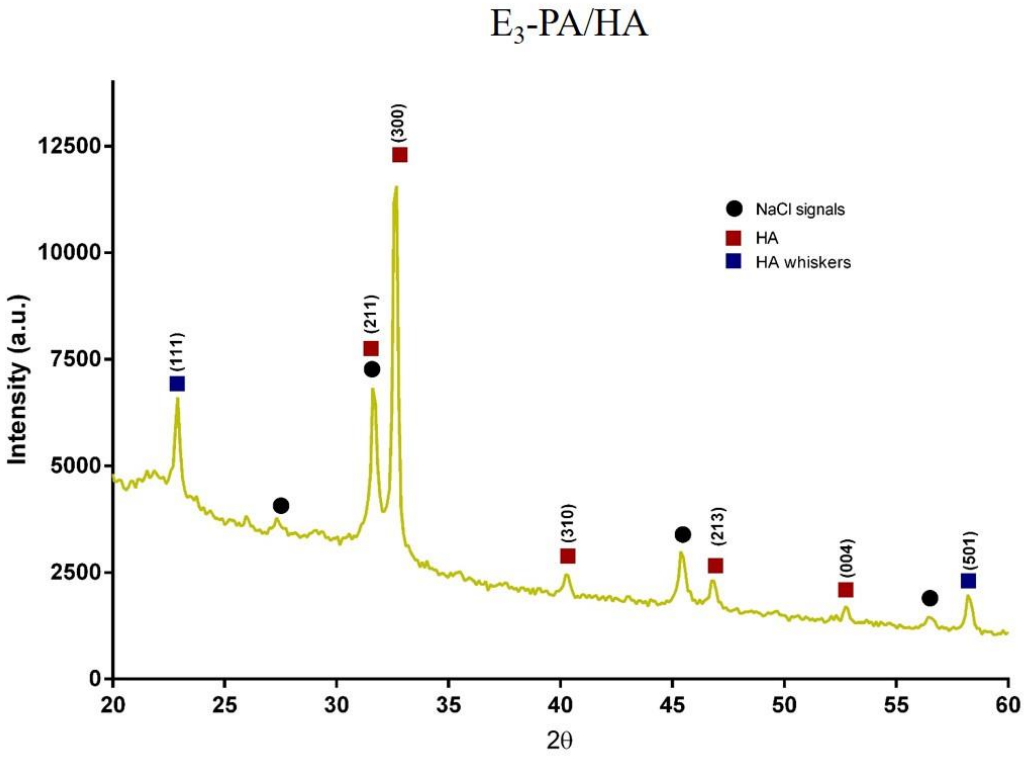

Figure 4.5 XRD patterns of calcium phosphate mineralized E_3-PA nanofibers.

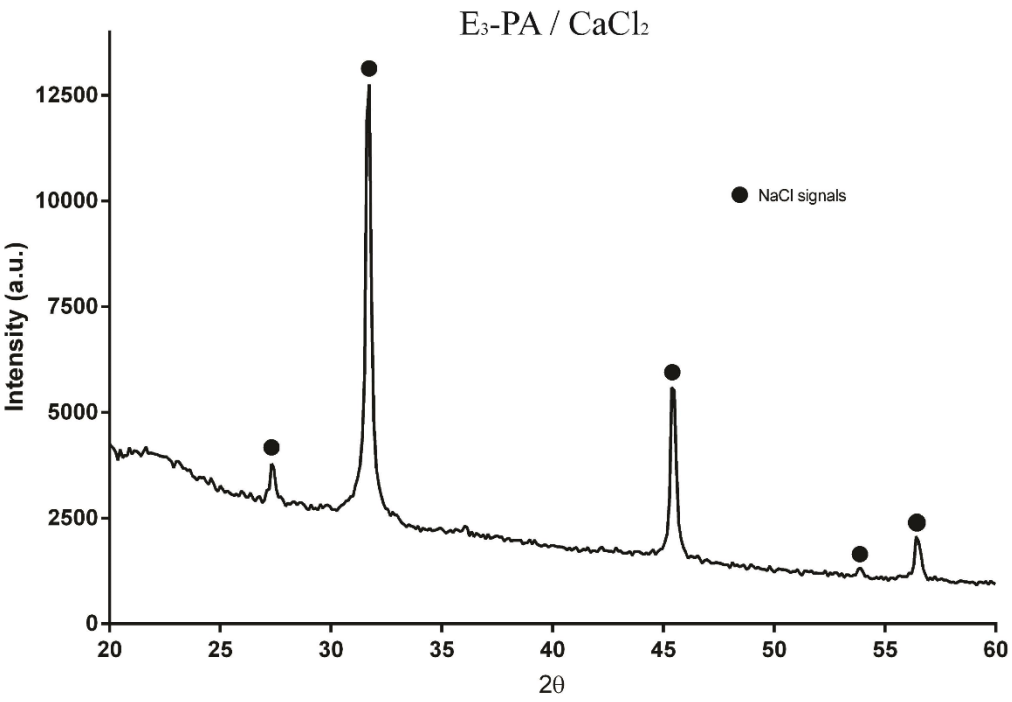

Figure 4.6 XRD patterns of non-mineralized E_3-PA nanofibers. The triggering mechanism of self-assembly is calcium ions.

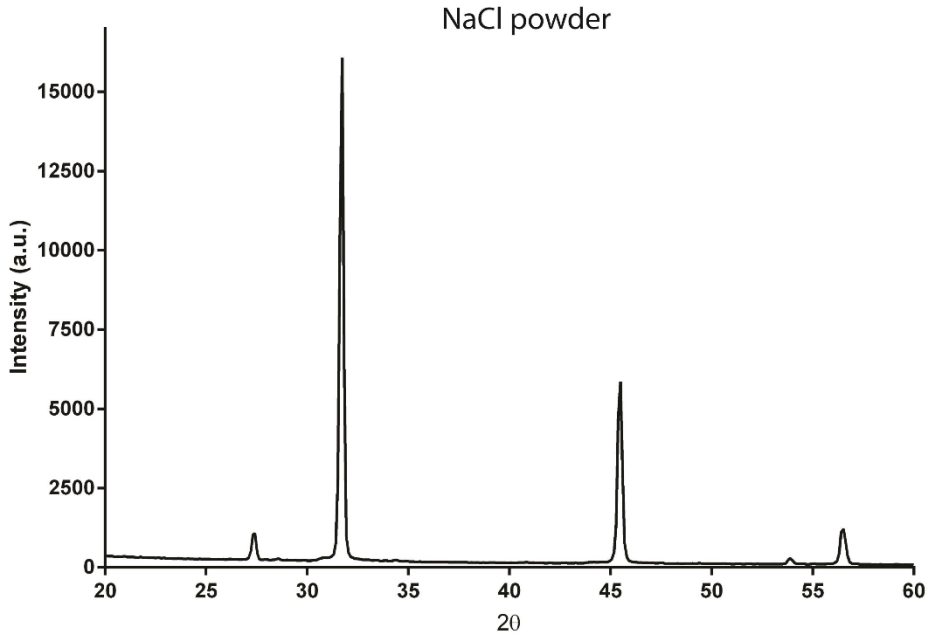

Figure 4.7 XRD patterns of NaCl salt.

4.3.4 Mechanical Properties of Mineralized PA Nanofibers

Rheological measurements were performed to determine the viscoelastic properties of mineralized and non-mineralized peptide amphiphile nanofibers. Through rheological measurements, we obtained storage moduli (G´) and loss moduli (G´´) of the materials, and the mechanical stiffness of peptide amphiphile nanofibers were found to be improved by the mineralization of nanofibers (Figure 4.8). In fact, our results showed that, while non-mineralized peptide amphiphile nanofibers demonstrated G´ values ranging from 0.5 kPa to 2 kPa, G´ values of mineralized peptide amphiphile nanofibers were in the 9 kPa–13 kPa range.

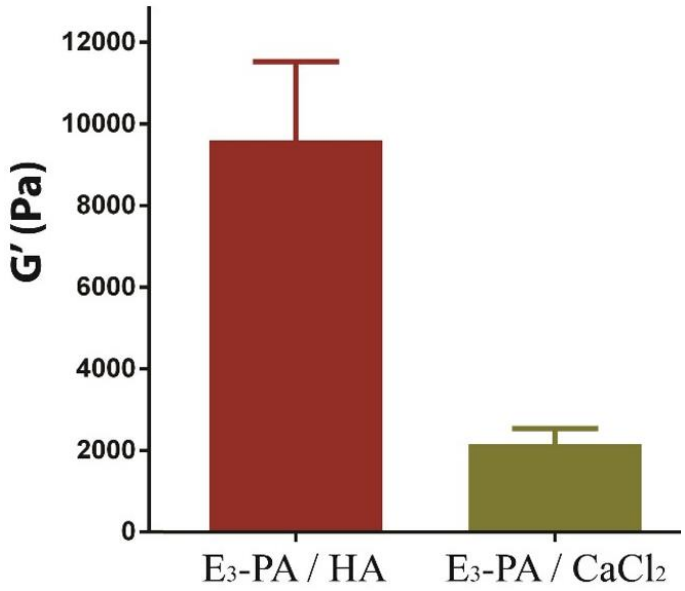

Figure 4.8 Equilibrium storage moduli of mineralized E_3-PA nanofibers.

4.3.5 Cell Viability and Behavior on Mineralized PA Nanofibers

Scaffolds play a key role in tissue engineering by mimicking the native ECM, and the properties of these systems have been shown to affect cellular behaviors such as attachment, proliferation and differentiation [209]. Therefore, in order to investigate the effect of the mineralized peptide nanofiber systems on cellular behaviors, Saos-2

cells were seeded on mineralized peptide coated surfaces or uncoated tissue culture plate, and their viability, adhesion and proliferation were evaluated. Saos-2 is a human osteosarcoma cell line, and these cells are commonly used as a model system in bone regeneration and osteogenic differentiation studies [210]. Adhesion of Saos-2 cells on the mineralized peptide nanofiber network system was studied at 4 h following seeding. The number of cells adhered on peptide nanofibers was greater than those that adhered on non-mineralized and glass surfaces (Figure 4.9).

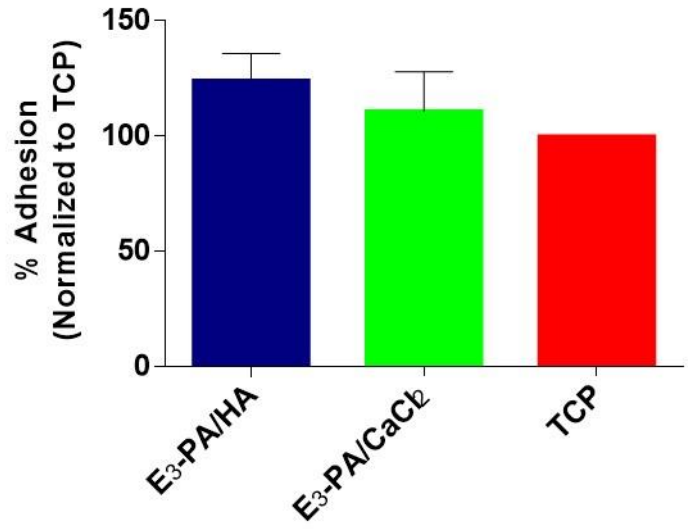

Figure 4.9 Relative adhesion of Saos-2 cells on the peptide nanofibers after 4 h.

The effect of mineralized peptide nanofibers on the viability of Saos-2 cells was tested by calcein AM staining after 24 h of incubation. Cells were viable on all surfaces over this time period (Figure 4.10). Cellular viability on peptide nanofibers was comparable with TCP, which indicates the biocompatibility of mineralized peptide nanofibers (Figure 4.11).

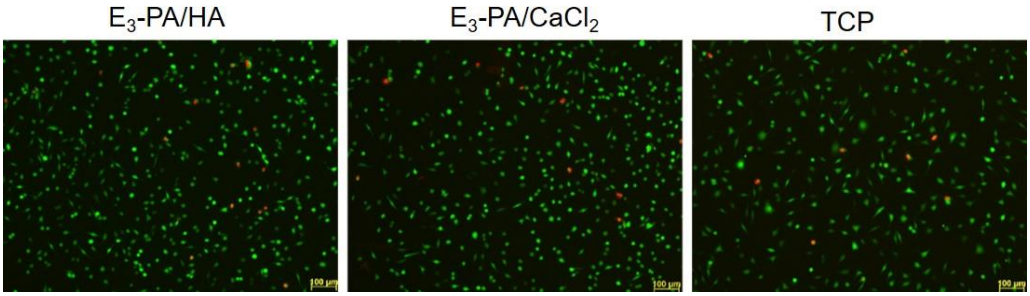

Figure 4.10 Viability of Saos-2 cells on mineralized and non-mineralized peptide nanofibers after 24 h of incubation. Live cells–green. Dead cells–red. Scale bars are 100 µm.

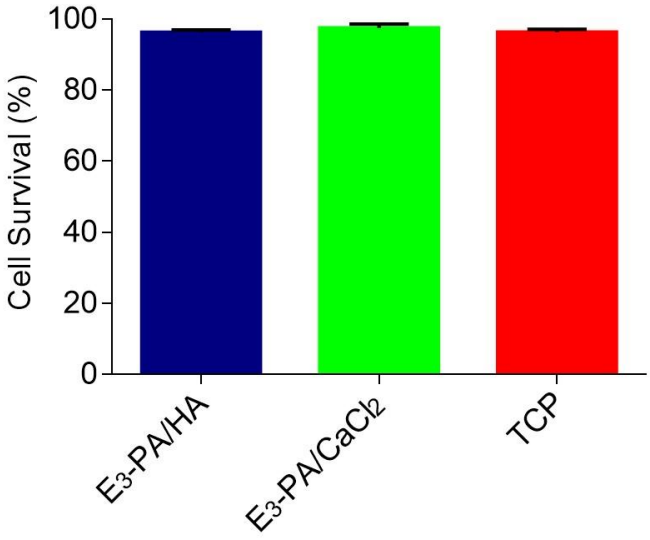

Figure 4.11 Viability of Saos-2 cells on mineralized and non-mineralized peptide nanofibers after 24 h of incubation.

The interaction of cells with peptide nanofibers was further evaluated by actin cytoskeleton staining (phalloidin/TO-PRO-3 staining) and examination of cell spreading. Cells adhered firmly on the peptide nanofiber networks and formed cytoskeletal attachments (Figure 4.12).

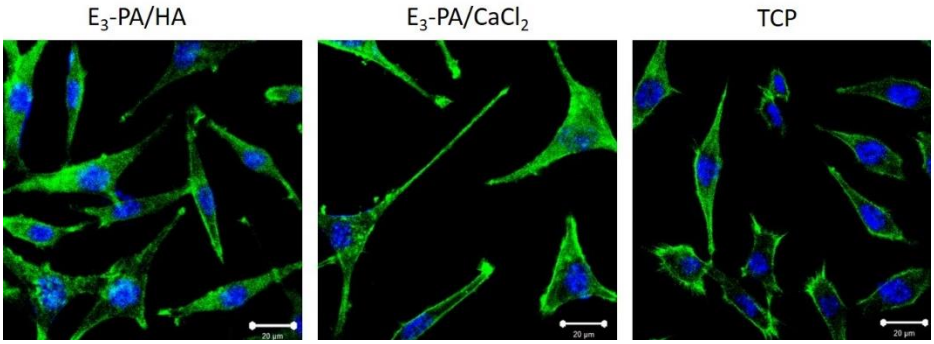

Figure 4.12 Spreading of Saos-2 cells characterized with actin fiber staining (nuclei stained with TO-PRO3 (blue), actin fibers stained with TRITC-conjugated phalloidin (green). Scale bars are 20 µm.

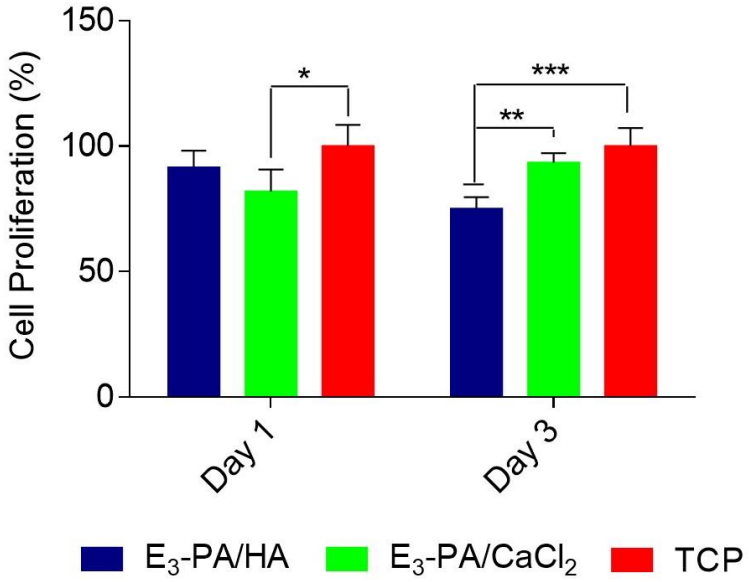

Figure 4.13 Relative proliferation of cells normalized to TCP on day 1 and 3. Error bars represent mean ± SEM, (*$p < 0.05$, **$p < 0.01$, ***$p < 0.001$).

When proliferation profiles of cells were studied on different surfaces, the proliferation of cells on mineralized peptide nanofibers was found to be comparable to TCP on day 1, but decreased compared to non-mineralized peptide nanofibers and TCP on day 3

(Figure 4.13). This effect may be an indicator of cellular differentiation, since decreased cell proliferation is associated with an increase in osteoblast differentiation markers [211].

4.3.6 Alkaline Phosphatase Activity (ALP) Assay

The main glycosylated protein present in bone is alkaline phosphatase (ALP), which is bound to osteoblast cell surfaces by a phosphotidylinositol linkage and is also found free within the mineralized matrix. ALP hydrolyzes pyrophosphate and provides inorganic phosphate to promote mineralization [31]. As the ALP activity test is widely employed as an early marker of osteogenic differentiation, we tested the ALP activity of Saos-2 cells cultured on mineralized peptide nanofiber, nonmineralized peptide nanofiber and TCP surfaces after 3, 7 and 14 days of incubation in osteogenic medium and maintenance medium. Cells cultured on mineralized matrices in growth medium (which lacks any osteogenesis-inducing soluble factors) showed significantly enhanced ALP activity compared to non-mineralized peptide nanofiber and TCP groups on day 3 (Figure 4.14). On day 7, exposure to mineralized peptide nanofibers significantly enhanced the ALP activity in Saos-2 cells with respect to TCP. In addition, ALP activity of cells cultured on non-mineralized peptide nanofibers was significantly higher than both mineralized peptide nanofibers and TCP (Figure 4.14). Maximum ALP activity was observed on day 14 for all samples. In osteogenic medium group, cells on mineralized peptide nanofibers also exhibited significantly enhanced ALP activity with respect to both nonmineralized peptide nanofibers and TCP on days 7 and 14 (Figure 4.15).

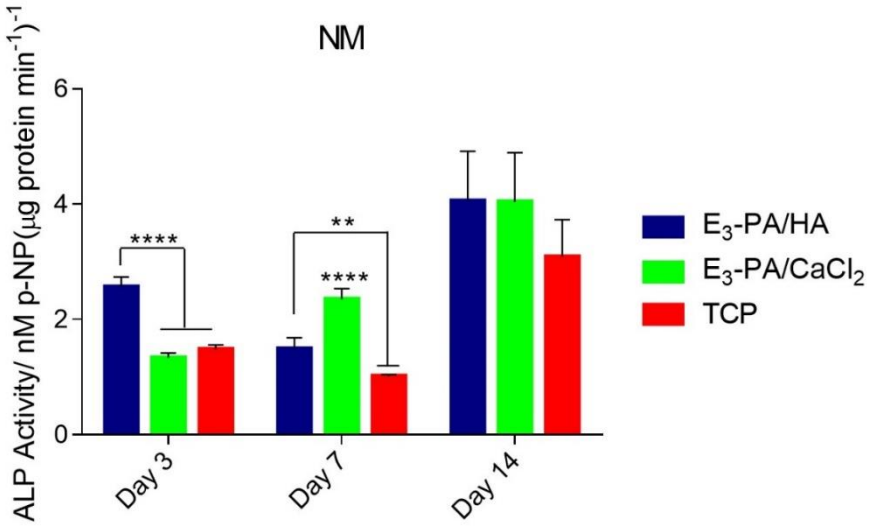

Figure 4.14 Effect of mineralized and non-mineralized peptide nanofibers on ALP activity of Saos-2 cells in normal medium on days 3, 7, and 14. ***$p < 0.001$, **$p < 0.01$.

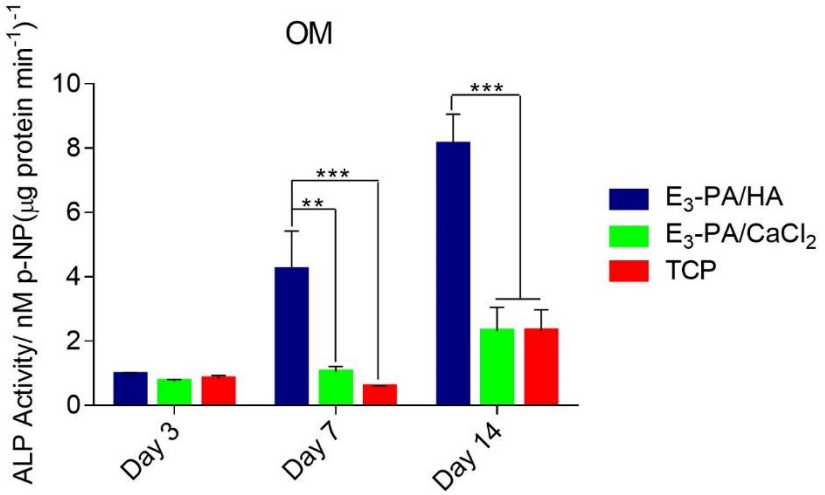

Figure 4.15 Effect of mineralized and non-mineralized peptide nanofibers on ALP activity of Saos-2 cells in osteogenic medium on days 3, 7, and 14. ***$p < 0.001$, **$p < 0.01$.

4.3.7 Gene Expression Profiles of Cells on Mineralized PA Nanofibers

Quantitative real-time RT-PCR measurements were performed to further evaluate osteogenic differentiation on mineralized peptide nanofibers, which were found to stimulate the expression of several osteogenic genes such as collagen I, osteocalcin and the transcription factor Runx2 in Saos-2 cells. Runx2 is a runt related transcription factor that is essential for osteoblast differentiation and regulates the expression of several osteoblastic genes such as α(I)collagen, osteopontin, bone sialoprotein, and the skeletal-specific osteocalcin [212].

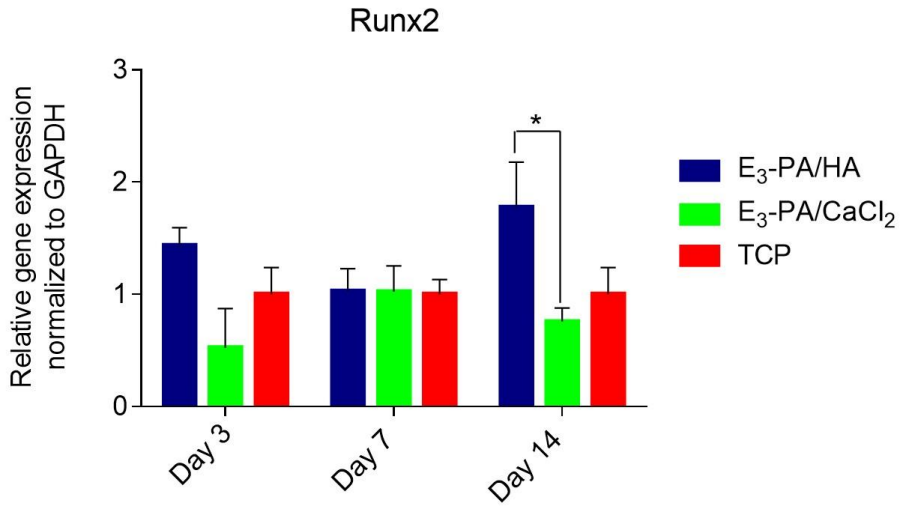

Figure 4.16 Gene expression analysis of Runx2 on days 3, 7 and 14 in maintenance medium. Expression levels of each gene were normalized against TCP and GAPDH was used as internal control, $*p < 0.05$.

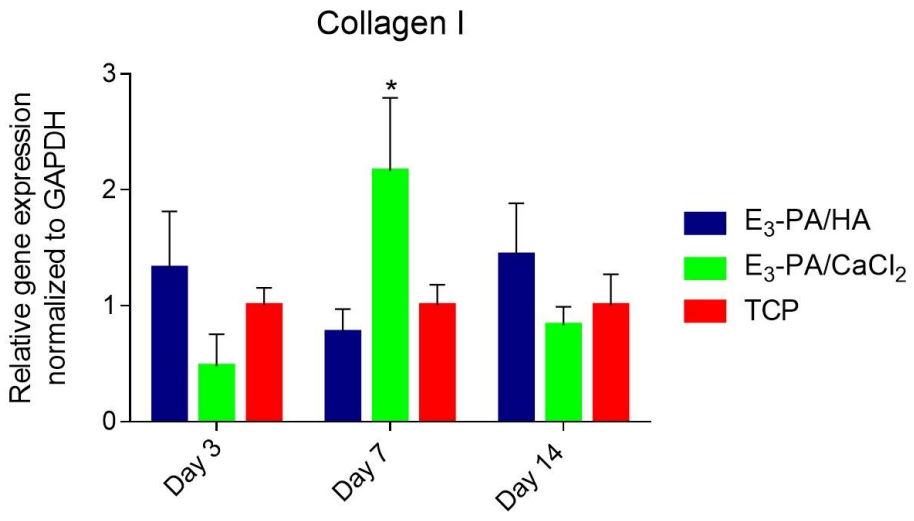

Figure 4.17 Gene expression analysis of collagen I in maintenance medium on days 3, 7 and 14. Expression levels of each gene were normalized against TCP and GAPDH was used as internal control, $*p < 0.05$.

A characteristic collagen I-rich matrix is also deposited at an early stage of osteogenic differentiation, acting as a template for mineralization [183]. Osteocalcin is a noncollagenous protein that is crucial for the mineralization of bone, and it is usually used as a late marker of ostegenic differentiation [158]. In the maintenance medium group, the expression of Runx2 and collagen I was upregulated on day 3 when cells were cultured on mineralized peptide nanofibers compared to cells on non-mineralized peptide nanofibers and TCP (Figures 4.16 and 4.17). On day 7, the expression of collagen I was significantly upregulated when Saos-2 cells were cultured on non-mineralized peptide nanofibers compared to cells on mineralized peptide nanofibers and TCP by ~2.8 and ~2.1 folds, respectively (Figure 4.17). On day 14, Runx2 expression of cells on mineralized peptide nanofibers was significantly higher compared to cells on non-mineralized peptide nanofibers by ~2.4 folds (Figure 4.16).

Osteocalcin expression of cells was also enhanced by ~1.6 fold on mineralized peptide nanofibers compared to TCP (Figure 4.18).

In osteogenic medium group, Runx2 expression of cells on mineralized peptide nanofibers was significantly upregulated by ~18.12 and ~2.0 folds on day 7 compared to non-mineralized peptide nanofibers and TCP (Figure 4.19). Collagen I expression of cells on mineralized peptide nanofibers was also enhanced by ~5.5 folds and ~1.26 folds compared to non-mineralized peptide nanofibers and TCP, respectively (Figure 4.20). On day 14, expression of osteocalcin was higher on both mineralized peptide nanofibers and non-mineralized peptide nanofibers compared to TCP (Figure 4.21). In addition, cells on peptide nanofibers showed intense collagen I immunostaining on day 7 (Figure 4.22).

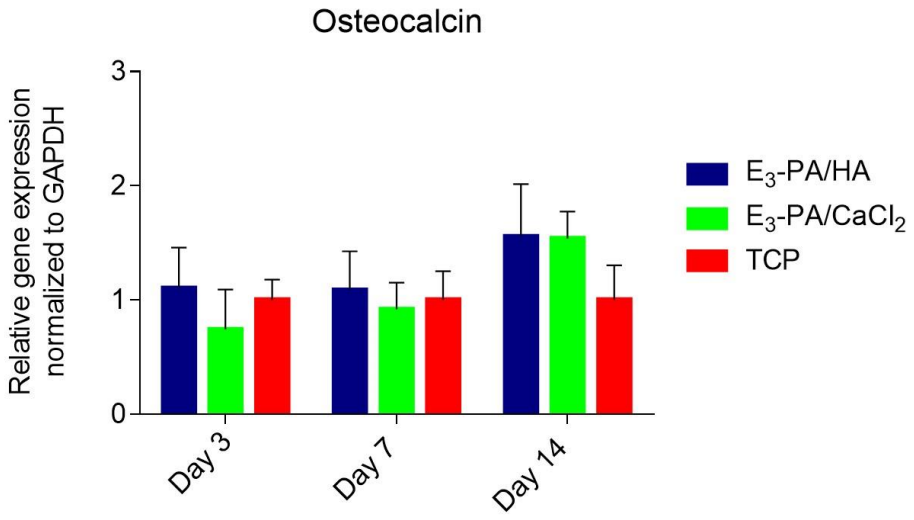

Figure 4.18 Gene expression analysis of osteocalcin in maintenance medium on days 3, 7 and 14. Expression levels of each gene were normalized against TCP, and GAPDH was used as internal control, $*p < 0.05$.

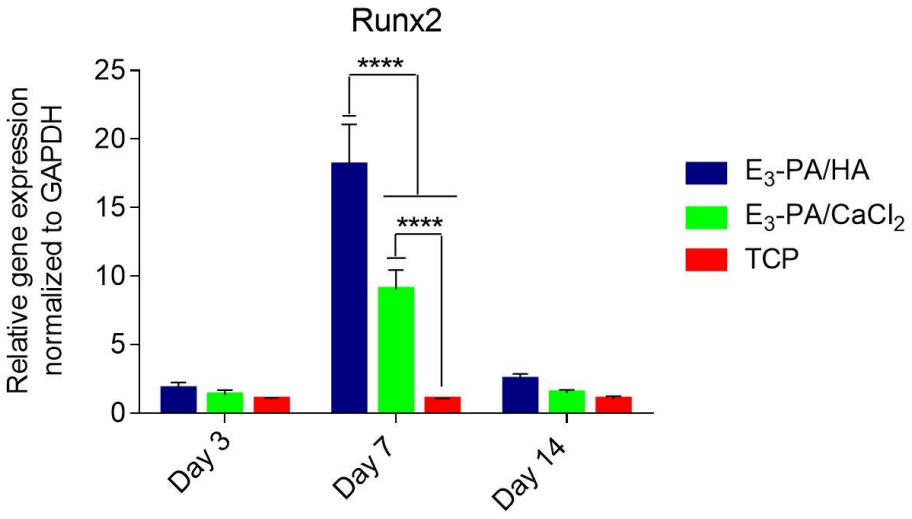

Figure 4.19 Gene expression analysis of Runx2 in osteogenic medium on days 3, 7 and 14. Expression levels of each gene were normalized against TCP, and GAPDH was used as internal control, ****$p < 0.0001$.

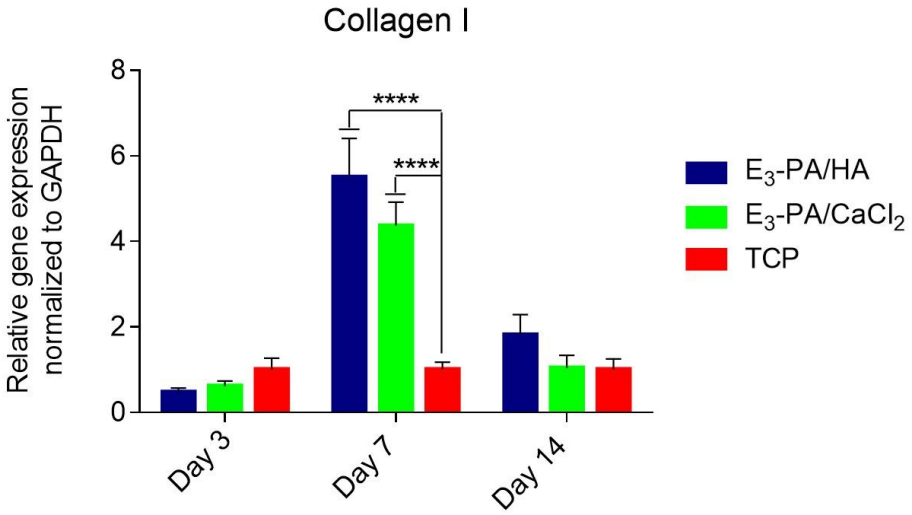

Figure 4.20 Gene expression analysis of collagen I in osteogenic medium on days 3, 7 and 14. Expression levels of each gene were normalized against TCP, and GAPDH was used as internal control, ****$p < 0.0001$.

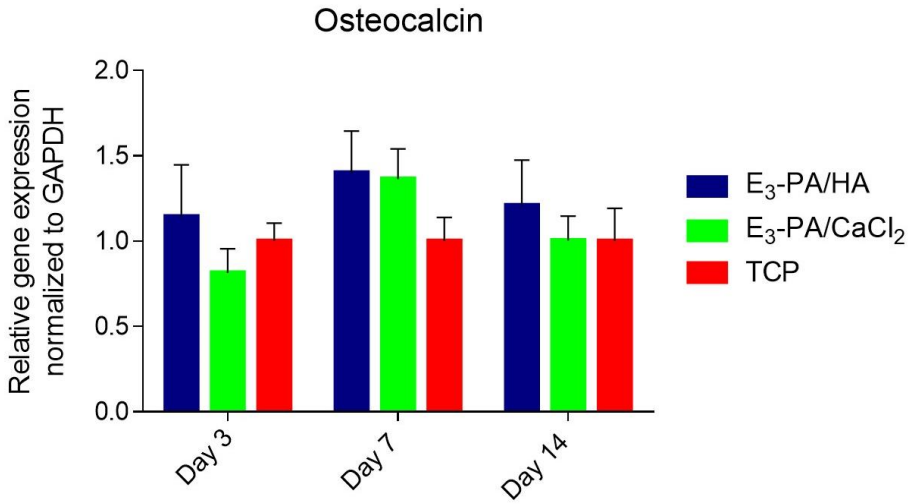

Figure 4.21 Gene expression analysis of osteocalcin in osteogenic medium on days 3, 7 and 14. Expression levels of each gene were normalized against TCP, and GAPDH was used as internal control.

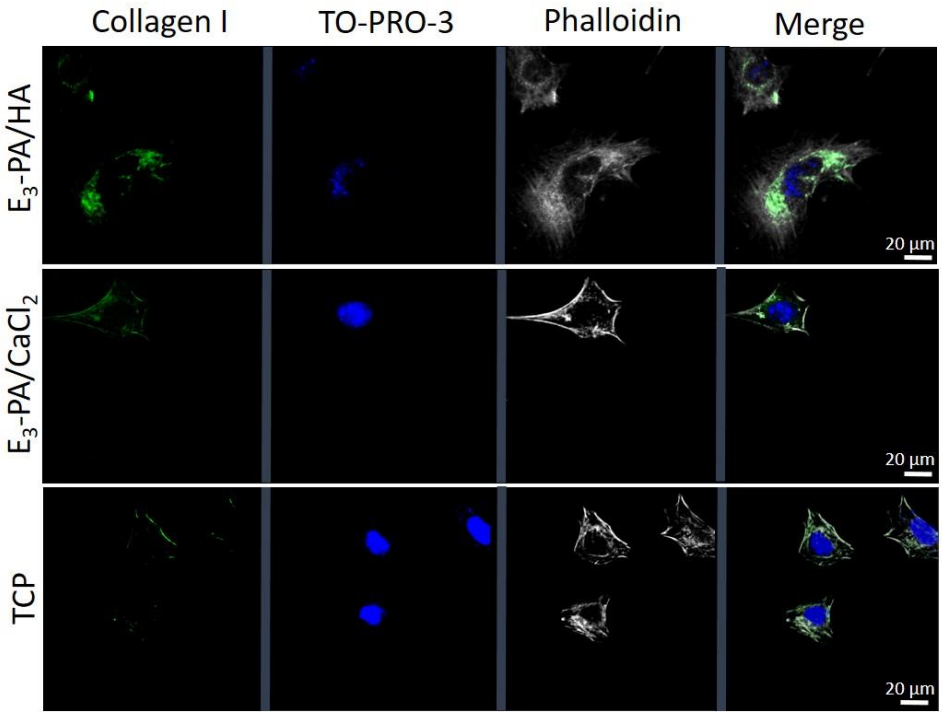

Figure 4.22 Immunostaining of collagen I in osteogenic medium on day 7.

4.4 Conclusion

Here, we present the synthesis of mineralized peptide amphiphile nanofibers in a templated manner. An anionic nanofiber gel matrix was used as template for the formation of HA nanocrystals, and its nucleation, growth and morphological alterations were investigated by TEM. XRD results demonstrated that the PA template promotes the formation of hydroxyapatite crystals. Rheological measurements showed that mineralized peptide nanofibers were mechanically superior compared to non-mineralized counterparts. Based on ALP activity assay and osteogenic gene expression analysis, the presence of HA in PA nanofibers seems to favor osteogenic differentiation. The stimulating effect on osteogenesis by hydroxyapatite surfaces may result from altered cell–extracellular matrix interactions; as such, the dynamic behaviour of focal adhesions should be investigated in further studies.

Chapter 5

5. Dentin Phosphoprotein (DPP)-Mimetic Peptide Nanofibers Promote Biomineralization

5.1 Introduction

Mineralization of hard connective tissues, such as bone and dentin, is a complex process that involves the deposition of hydroxyapatite (HA) within a collagenous matrix [213, 214]. Understanding the mechanisms of mineral deposition in collagen is vital for the development of treatments for mineralization-related diseases, and may have key importance for the design of bioinspired materials for hard tissue repair [213, 215].

Dentin is a mineralized connective tissue that is formed by odontoblasts. This mineralized connective tissue develops through a mechanism similar to bone. During its formation, odontoblasts secrete unmineralized, type I collagen-rich matrices called “predentin” [216]. This unmineralized organic phase lies between the mineralization front and odontoblasts, forming the corresponding mineralized tissue. Through the deposition of HA crystals, this proteinaceous matrix is gradually transformed into a mineralized structure. Similar to bone, this is a dynamic process involving active interactions between type I collagen and numerous non-collagenous proteins [216].

Both collagen and non-collagenous proteins regulate the nucleation, growth and inhibition of HA during hard tissue formation [214]. Among these non-collagenous proteins, dentin sialophosphoprotein (DSPP) is a member of the SIBLING family and was originally thought to be dentin-specific [217]. These NCPs are known to actively

promote and control the mineralization of collagen fibers and crystal growth within predentin, which facilitates the conversion of this tissue to dentin [218]. Afterwards, several studies showed the expression of DSPP in bone [219], cementum [220], and certain non-mineralized tissues [221, 222]. Human and mouse genetic studies demonstrated that *DSPP* gene mutations and ablations lead to mineralization defects in dentin and bone, which indicates the importance of DSPP in biomineralization [223-226].

DSPP is expressed from the DSPP gene (4q21) and cleaved by proteases into three active protein products: N-terminal dentin sialoprotein (DSP), intermediate dentin glycoprotein (DGP) and C-terminal dentin phosphoprotein (DPP) (Figure 5.1) [227, 228].

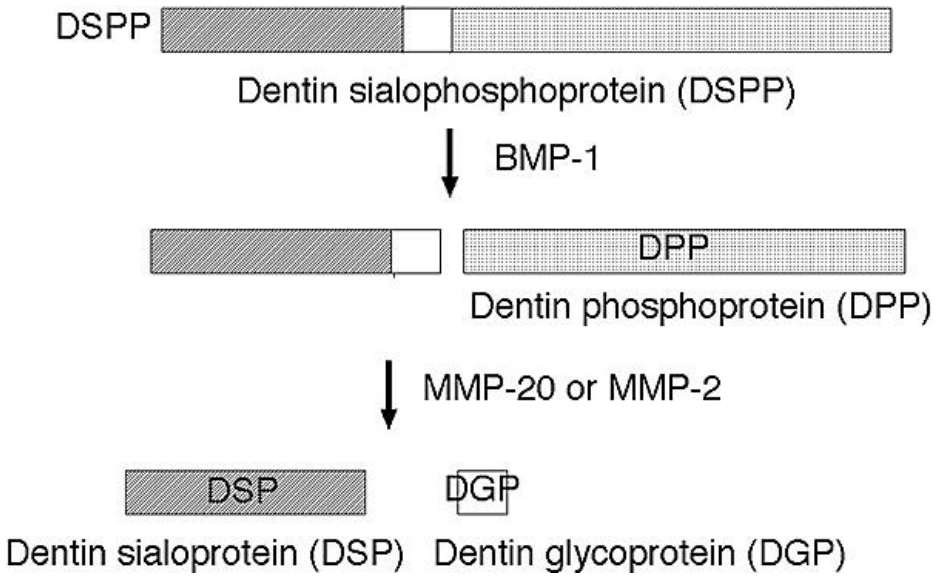

Figure 5.1 Processing of dentin sialophosphoprotein (DSPP). DSPP is the precursor of dentin phosphoprotein (DPP). (Reproduced from Ref. [228] with permission from Frontiers in Bioscience Publishing Group).

While the precise function of DGP remains relatively unclear, both DSP and DPP are abundantly present in the dentin matrix and appear to play crucial roles in the initiation and maturation phases of dentin formation, respectively [229, 230]. DPP, a highly phosphorylated protein, contains extremely high ratios of phosphoserine and aspartic acid, with most of the serine residues being phosphorylated [228]. This makes DPP a very polyanionic protein that binds to large amounts of calcium with a relatively high affinity [231, 232] and plays a critical role in the formation of hydroxyapatite crystals that form the bulk of the dentin structure [233]. However, while the hydroxyapatite-binding and mineralization-inducing capacities of DPP have been replicated in a short, serine-rich, non-phosphorylated peptide sequence [234], the potential effects of serine phosphorylation on these properties have not fully been demonstrated in PA systems.

The whole amino acid sequence of rat DSPP has been deduced using cDNA libraries [235], and was used in the present study to design a dentin phosphoprotein-mimetic peptide amphiphile molecule (SpDSp-PA). This PA molecule was designed to emulate the structure and function of DSPP in general and DPP in particular, and bears Ser(phos)-Asp-Ser(phos) (SpDSp) repeats to effectively induce mineralization and subsequent differentiation of osteogenic cells. Self-assembling SpDSp-PA hydrogels were produced through calcium ion-mediated charge neutralization, creating a calcium-rich matrix that may further stimulate osteogenesis under *in vitro* conditions. We then evaluated the capacity of self-assembled, DPP-mimetic PA scaffolds to support the hydroxyapatite deposition, survival and biomineralization of osteogenic cells. In addition, a non-phosphorylated control (SDS-PA) was utilized to assess the influence of phosphoryl groups on biomineralization.

Ca ion-treated SpDSp-PA hydrogels showed a strong capacity for biomineralization, in contrast to soluble, non-hydrogel peptides which were ineffective for this purpose. Compared to SpDSp-PA, non-phosphorylated SDS-PA networks also failed to facilitate mineral deposition despite their nanofibrous structure. This suggests that phosphoryl residues and scaffold formation are both critical for the formation of hydroxyapatite. As Ca ion-treated SpDSp-PA hydrogels also supported the survival, osteogenic differentiation and biomineralization of Saos-2 cells, the hydrogel system described here shows great promise to be used in the further investigation of the biomineralization process in hard tissues.

5.2 Experimental Section

5.2.1 Materials

Rink amide MBHA resin, Fmoc protected all protected amino acids, lauric acid, HBTU, triisopropylsilane (TRIS), DIEA, and TFA were purchased from Sigma-Aldrich, Novabiochem, Alfa Aesar or Merck. Calcein-AM and other cell culture materials were obtained from Invitrogen or Thermo-Fisher. All other chemicals and materials used in this study were purchased from Thermo-Fisher, Merch, Alfa Aesar or Sigma-Aldrich.

5.2.2 Synthesis of Peptide Amphiphile (PA) Molecules

Lauryl-VVAGS(Phos)DS(Phos)G-Am and Lauryl-VVAGSDSG-Am peptides were constructed on a Rink amide MBHA resin (Novabiochem) at a 0.25 mmol scale. Amino acid couplings were done with 2 equivalents of Fmoc-protected amino acid, 1.95 equivalents of HBTU, and 3 equivalents of DIEA for 2 h. Fmoc removal was performed with 20% piperidine/dimethylformamide (DMF) solution for 20 min. Peptides were cleaved from the resin with a mixture of TFA:TIS:H_2O in the ratio of

95:2.5:2.5 for 3 h. Excess TFA was removed by rotary evaporation; the remaining viscous peptide solution was triturated with ice-cold ether, and the resulting white product was freeze-dried for use following resolubilization in water. The identity and purity of peptide amphiphile molecules were determined by LC-MS (Agilent 6530−1200 Q-TOF) analysis. Mass spectrum was obtained with Agilent LC-MS equipped with Agilent 6530 Q-TOF with an ESI source and Zorbax Extend-C18 2.1 mm × 50 mm column for basic conditions. A gradient of (a) water (0.1% NH_4OH) and (b) acetonitrile (0.1% NH_4OH) was used. To purify the peptides, an Agilent preparative reverse-phase HPLC system equipped with a Zorbax Extend-C18 21.2 mm × 150 mm column was used with a gradient of (a) water (0.1% NH_4OH) and (b) acetonitrile (0.1% NH_4OH).

5.2.3 Circular Dichroism (CD) of DPP-Mimetic PAs

For CD measurements, all peptides are dissolved in water at a concentration of 1 mM and calcium (10 fold excess, 10 mM) was used for gel formation. Peptide/Ca mixtures were incubated until gel equilibrium was reached, and subsequently diluted to a final concentration of $5x10^{-5}$ M for CD analysis. A JASCO J815 CD spectrometer was used at room temperature. Measurements were performed with three accumulations from 300 nm to 190 nm, data interval and data pitch being 0.1 nm and scanning speed being 100 nm/min. Digital integration time was selected as 1 s, band width as 1 nm, and the sensitivity was standard.

5.2.4 Oscillatory Rheology Measurements of DPP-Mimetic PAs

Viscoeslastic properties of DPP like Ca mixture materials were measured with Anton Paar Physica RM301. Rheometer operating was performed by 25 mm parallel plate configuration at 25 °C. 125 µL of each sample (peptide and 10 fold excess calcium

chloride) and 250 µL total volume with a final peptide concentration of 1 wt% was carefully loaded on the center of the lower plate and incubated for 15 min before measuring. The upper plate was lowered to a gap distance of 0.5 mm after equilibration. Storage moduli (G′) and loss moduli (G″) values were screened from 100 rad/s to 0.1 rad/s of angular frequency, with a 0.5% shear strain.

5.2.5 Transmission Electron Microscopy (TEM) Imaging of DPP-mimetic PAs

TEM imaging was performed with a FEI Tecnai G2 F30 transmission electron microscope at 300 kV. 1 mM peptide solution was prepared and gelified with 10 mM Ca solution and incubated for 6 h. Then, peptide gels were diluted with water and a small amount of solution was dropped onto carbon covered copper grids. 2% (w/v) uranyl acetate solution was used to stain peptide fibers with enhanced contrast. Prior to TEM imaging, the carbon grids were air-dried.

5.2.6 Mineralization of DPP-Mimetic Nanonetworks in Simulated Body Fluid

For sample preparation, coverslip surfaces were coated with 2 mM peptide solutions. After they were incubated with 1.5x simulated body fluid (SBF) for 12 h, the solution was discarded and the coverslips were washed repeatedly with water. For SEM imaging, samples were dehydrated in ethanol/water gradient. Then, samples were dried in critical point drier and coated with 3 nm Au−Pd. Finally, they were imaged under scanning electron microscopy (SEM) operating under 10−15 kV.

5.2.7 Cell Culture and Maintenance

Saos-2 human osteosarcoma cells (ATCCHTB-85) were used in viability, immunocytochemistry (ICC), gene expression and *in vitro* biomineralization experiments. All cells were cultured in 75 cm^2 cell culture flasks using Dulbecco's

modified Eagle medium (DMEM) supplemented with 10% fetal bovine serum (FBS), 1% penicillin/streptomycin, and 2 mM L-glutamine. The cells were kept at 37 °C in a humidified chamber supplied with 5% CO_2. Cell passage was carried out at cell confluency between 80 and 90% using trypsin/EDTA chemistry. The culture medium was changed every 3−4 days. The osteogenic differentiation experiments (ICC stainings and RT-PCR analysis) were conducted in two groups: osteogenic medium (OM) group [osteogenic medium is a combination of the maintenance medium with 10 mM β-glycerophosphate, 50 μg mL^{-1} ascorbic acid, and 10 nM dexamethasone] and maintenance medium (MM) group [Dulbecco's modified Eagle's medium (DMEM, Gibco), containing 10% fetal bovine serum, 100 μg/mL streptomycin and 100 U/mL [penicillin/streptomycin].

5.2.8 Viability of Saos-2 Cells on PA Networks

The viability of Saos-2 cells incubated on peptide nanofibers and uncoated tissue culture plates (TCP) for 24 h was studied by Live/Dead Assay (Invitrogen). Briefly, cells were seeded on peptide coated nanofibers and uncoated 96-well tissue culture plates at a density of 5 x 10^3 cells/well for 24 h. After incubation under standard conditions for 24 h, cells were stained with 2 μ M calcein-AM and and 4 μ M ethidium homodimer I (EthD-1) in PBS (1X) for 30 min at room temperature. Images were taken at three random points per well with a fluorescent microscope at 100x magnification. Viable cells were imaged under fluorescence microscope. All samples were studied in triplicate. Live and dead cells were counted by using Image J and number of live cells was calculated for each sample.

5.2.9 Immunocytochemistry (ICC)

Before ICC stainings, differentiated cells were fixed with 4% formaldehyde for 15 min and permeabilized with 0.5% Triton-X for 10 min at room temperature. 3 wt % BSA/PBS was used for blocking for 1 h. Rabbit-raised, anti-human, DMP-1 polyclonal antibodies and goat-raised, anti-rabbit, IgG H&L DyLight 488 conjugated secondary antibodies (Abcam) (ab103203 and ab96899, respectively) were obtained from Abcam. Filamentous actins were stained with TRITC-conjugated phalloidin and the cell nuclei were stained with TO-PRO-3 iodide. The samples were visualized with a Zeiss LSM 510 confocal microscope.

5.2.10 Gene Expression Analysis

For gene expression studies, Saos-2 cells were seeded on peptide nanofiber-coated and uncoated wells of 6-well plates at a density of 2.5×10^5 cells per cm^2. Gene expression profiles of Runx2, collagen I, and osteopontin were evaluated by quantitative RT-PCR (qRT-PCR) analysis for investigating the osteogenic differentiation process. RNA isolation from Saos-2 cells seeded on peptide nanofiber-coated and bare surfaces was performed after 7 days of incubation by using TRIzol (Invitrogen) according to the manufacturer's instructions. Yield and purity of extracted RNAs were assessed by Nanodrop 2000 (Thermo Scientific). Samples were diluted to a concentration of 100 ng/μL prior to their use. Primers for PCR amplification of Runx2, collagen I, osteopontin and GAPDH are shown in Table S1. Melting temperatures (Tm) for the primers were determined as 58 °C for Runx2 and GAPDH, 57.3°C for osteopontin, and 61.4 °C for collagen I. cDNA synthesis from RNA and qRT-PCR were performed using SuperScript III Platinum SYBR Green One-Step qRT-PCR Kit according to the

manufacturer's instructions. mRNA levels were calculated and normalized to GAPDH according to comparative Ct method for each target gene [178].

5.3 Results and Discussion

5.3.1 Design and Characterization of DPP-Mimetic Peptide Amphiphile Molecules

The DPP-mimetic peptide amphiphile was synthesized using a solid-phase peptide synthesis method. The lauryl-VVAGSDSG sequence was used to imitate the Ser-Asp-Ser motifs that exist in large numbers in DPP. In this sequence, hydrophobic collapse in alkyl tails and β-sheet driving units in the VVAG peptide sequence promote the self-assembly of the peptide, while the phosphorylated or non-phosphorylated serine residues are presented on the SDSG sequence to facilitate the deposition of hydroxyapatite onto the nanofiber matrix. Two different PAs were synthesized; a phosphorylated negatively charged PA containing phosphoserine residues (SpDSp-PA) and a non-phosphorylated negatively charged PA containing serine residues (SDS-PA) (Figure 5.2). After the identification and purification of all PA molecules by LC-MS (Figure 5.3), the physicochemical characteristics of SDS-PA, SpDSp-PA and their hydrogels were characterized by circular dichroism, oscillatory rheology and SEM and TEM imaging.

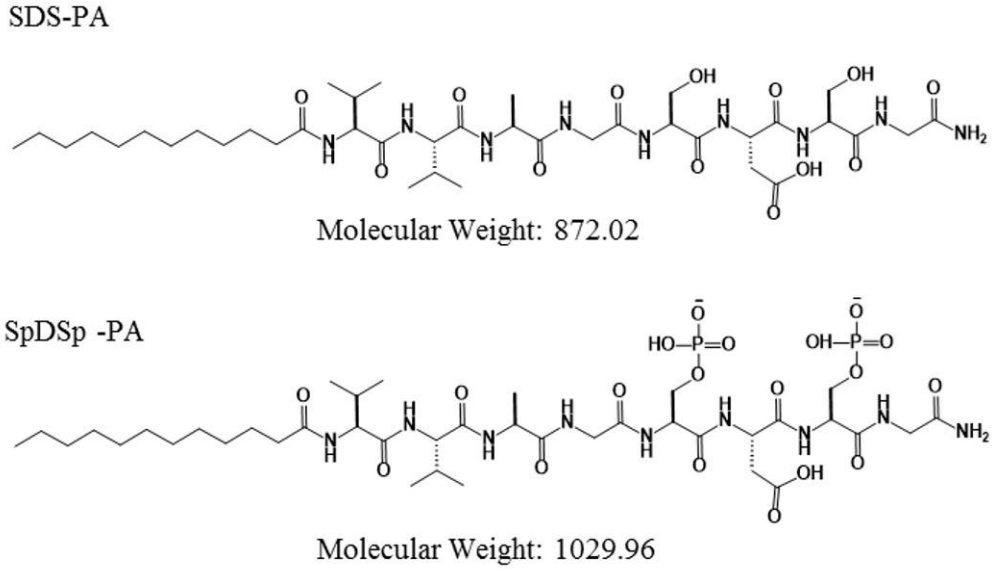

Figure 5.2 Chemical structures of the designed PA molecules

Ca-mediated co-assembly was used for the formation of hydrogels from SpDSp-PA solutions**,** in which an excess of calcium was added to neutralize the overall charge of SpDSp-PA. Calcium treatment was observed to rapidly induce the formation of hydrogels under room temperature, and Ca-mediated assemblies exhibited CD spectra consistent with a β-sheet structure (Figure 5.4). On the other hand, SpDSp-PA did not show any secondary structure formation in water, which might be due to its strong negative charge preventing any large-scale assemblies. In contrast to SpDSp-PA, SDS-PA did not require a neutralizing agent for its self-assembly, and consequently maintained a β-sheet structure with or without the inclusion of a cation (Figure 5.4). TEM imaging and oscillatory rheology measurements were also used to assess the calcium-induced hydrogel formation. Oscillatory rheology analyses showed that the storage modulus of Ca-treated SpDSp-PA was substantially higher than that of SDS-PA (Figure 5.5).

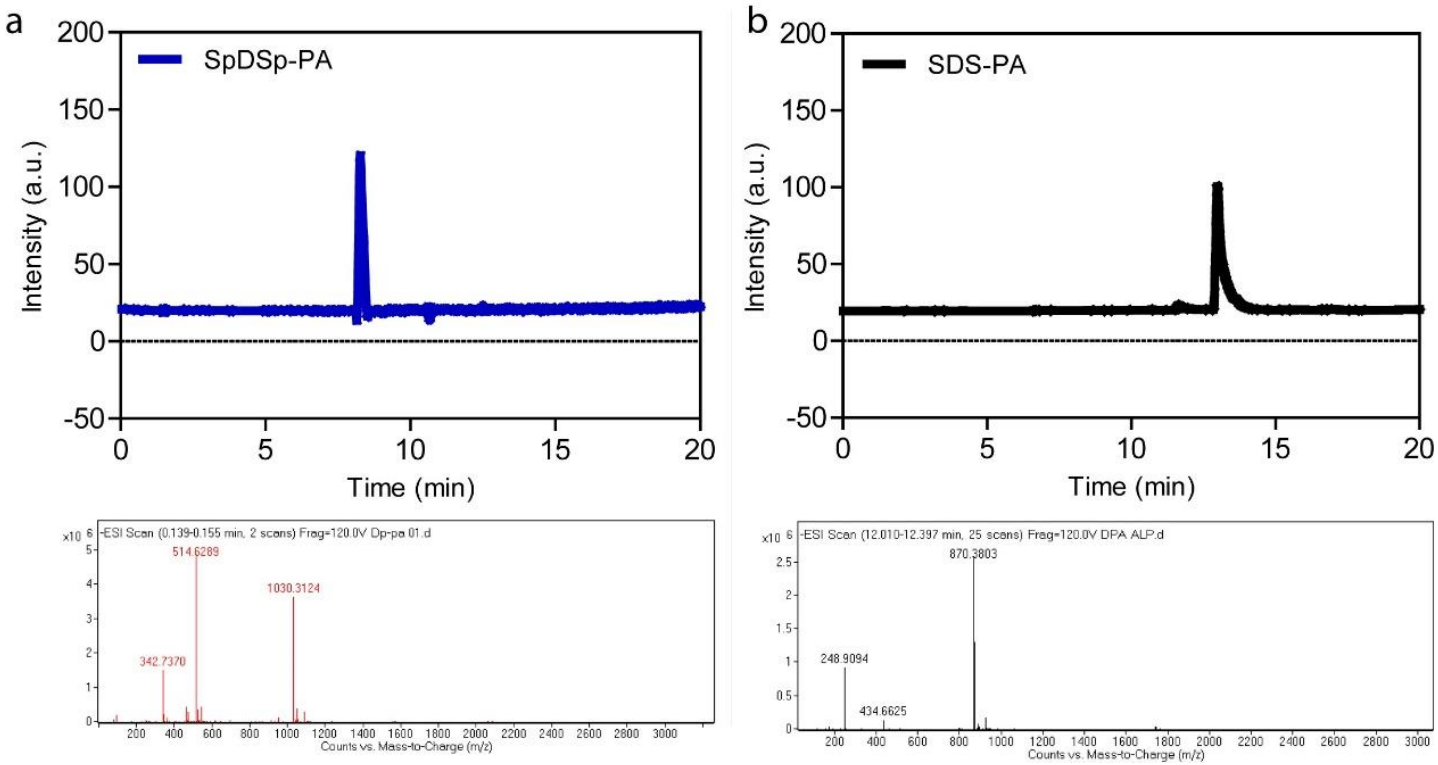

Figure 5.3 Liquid chromatography and mass spectrometry results of the PA molecules. (a) $[M-H]^-$ (calculated): 1030.96, $[M-H]^-$ (observed): 1030.31; $[M/2-H]^-$ (calculated): 514.49, $[M/2-H]^-$ (observed): 514.62; $[M/3-H]^-$ (calculated): 342.65, $[M/3-H]^-$ (observed): 342.73. (b) $[M-H]^-$ (calculated): 870.02, $[M-H]^-$ (observed): 870.38; $[M/2-H]^-$ (calculated): 434.01, $[M/2-H]^-$ (observed): 434.66.

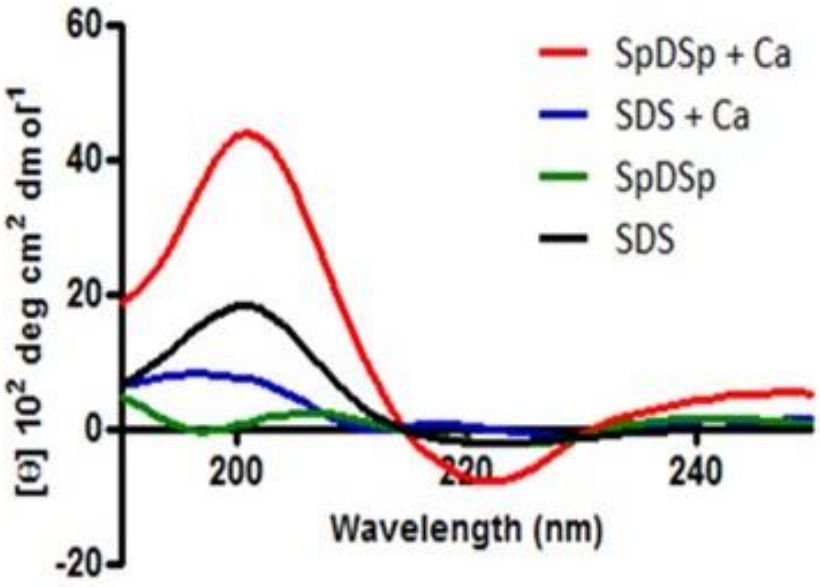

Figure 5.4 Secondary structure analysis of gels formed with the addition of calcium ion.

This suggests that the ion-mediated assemblages may be mechanically more stable than those created through the electrostatic interactions of hydrophobic tail groups and β-sheet-forming peptide sequences alone. Nonetheless, both hydrogel forms showed a fibrous structure common to many peptide amphiphile assemblies (Figure 5.6).

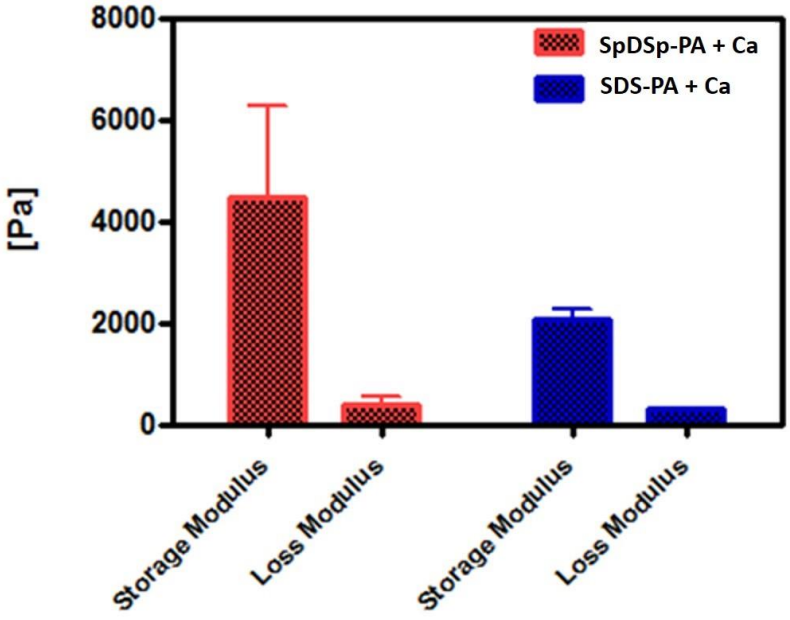

Figure 5.5 Oscillatory rheology of DPP-mimetic PA networks after addition of calcium ions.

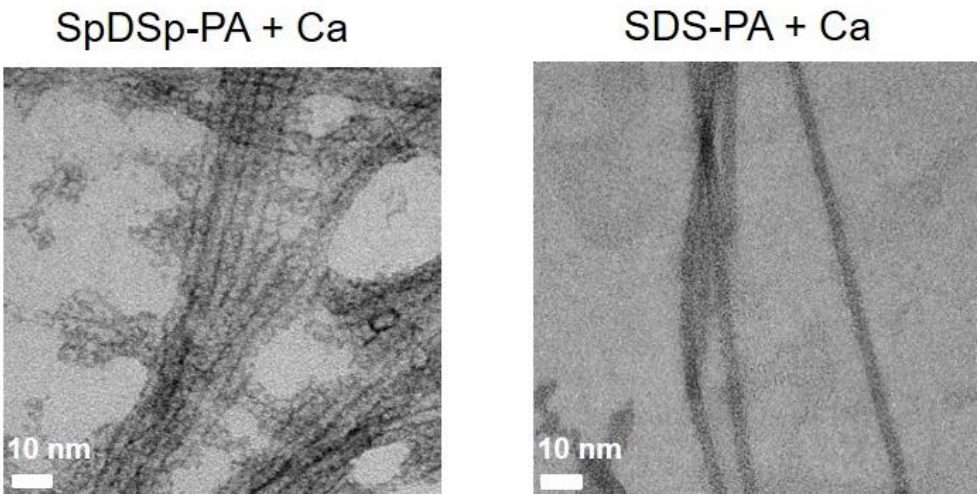

Figure 5.6 TEM images of DPP-mimetic PA networks after addition of calcium ions.

5.3.2 Mineral Deposition Capacity of DPP-Mimetic PAs under Ionic Self-Assembly

Here, an *in vitro* biomineralization assay was performed to determine the effectiveness of DPP-mimetic PAs in facilitating the deposition of a mineral matrix closer to hydroxyapatite found in dentin and bone. SEM and EDX results revealed that Ca ion-treated SpDSp-PA supported biomineralization with a Ca/P ratio of 1.54 (Figure 5.7 and Table 5.1), while non-treated SpDSp-PA and SDS-PA were both largely ineffective in facilitating the mineralization of the glass surface (Figure 5.7 and Tables 5.2-5.4). In addition, Dey *et al*. demonstrated that the surface-induced formation of apatite from simulated body fluid (SBF) starts with the aggregation of prenucleation clusters, which facilitate the nucleation of amorphous calcium phosphate before the development of oriented apatite crystals [236].

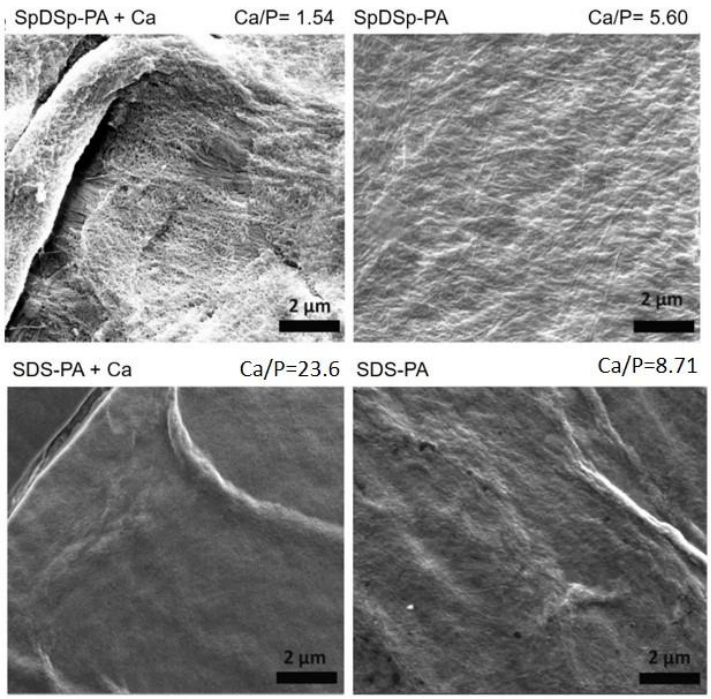

Figure 5.7 Hydroxyapatite deposition on peptide coated surfaces. Mineral deposition on peptide surfaces with and without hydrogel formation.

Table 5.1 SEM-EDX results of SpDSp-PA + Ca

Element	Wt %	At %	K-Ratio	Z	A	F
C K	28.86	36.98	0.1254	1.0274	0.4228	1.0005
N K	7.99	8.77	0.0176	1.0154	0.2163	1.0009
O K	47.90	46.07	0.1503	1.0044	0.3123	1.0001
Na K	6.82	4.57	0.0340	0.9305	0.5350	1.0002
P K	3.30	1.64	0.0277	0.9111	0.9205	1.0008
Ca K	5.13	1.97	0.0466	0.9030	1.0057	1.0000

Table 5.2 SEM-EDX results of SpDSp-PA

Element	Wt %	At %	K-Ratio	Z	A	F
C K	54.00	63.12	0.3225	1.0174	0.5869	1.0003
O K	36.72	32.23	0.1070	0.9947	0.2928	1.0001
Na K	5.12	3.13	0.0279	0.9209	0.5917	1.0001
P K	0.63	0.29	0.0054	0.9019	0.9459	1.0006
Ca K	3.53	1.23	0.0319	0.8936	1.0129	1.0000

Here, these stages of mineralization were observed on Ca ion-treated SpDSP-PA nanofibers incubated in SBF (Figure 5.8 and Figure 5.9). Therefore, we suggest that the presence of a well-organized nanofiber scaffold can support or substitute for the

strongly negative charge of naturally occurring DPP, allowing for efficient mineralization.

Table 5.3 SEM-EDX results of SDS-PA + Ca

Element	Wt %	At %	K-Ratio	Z	*A*	*F*
C K	51.56	58.82	0.3524	1.0129	0.6746	1.0002
N K	12.97	12.69	0.0225	1.0011	0.1735	1.0004
O K	31.06	26.60	0.0757	0.9904	0.2459	1.0000
Na K	1.44	0.86	0.0077	0.9166	0.5838	1.0000
P K	0.12	0.05	0.0011	0.8979	0.9576	1.0006
Ca K	2.84	0.97	0.0257	0.8895	1.0161	1.0000

Table 5.4 SEM-EDX results of SDS-PA

Element	Wt %	At %	K-Ratio	Z	A	F
C K	55.81	64.39	0.2771	1.0153	0.4888	1.0002
N K	10.41	10.30	0.0164	1.0035	0.1572	1.0003
O K	23.38	20.25	0.0553	0.9927	0.2384	1.0001
Na K	1.89	1.14	0.0107	0.9189	0.618	1.0005
Si K	6.48	3.20	0.0559	0.9329	0.9243	1.0002
P K	0.21	0.09	0.0018	0.9000	0.9268	1.0003
Ca K	1.83	0.63	0.0164	0.8917	1.0095	1.0000

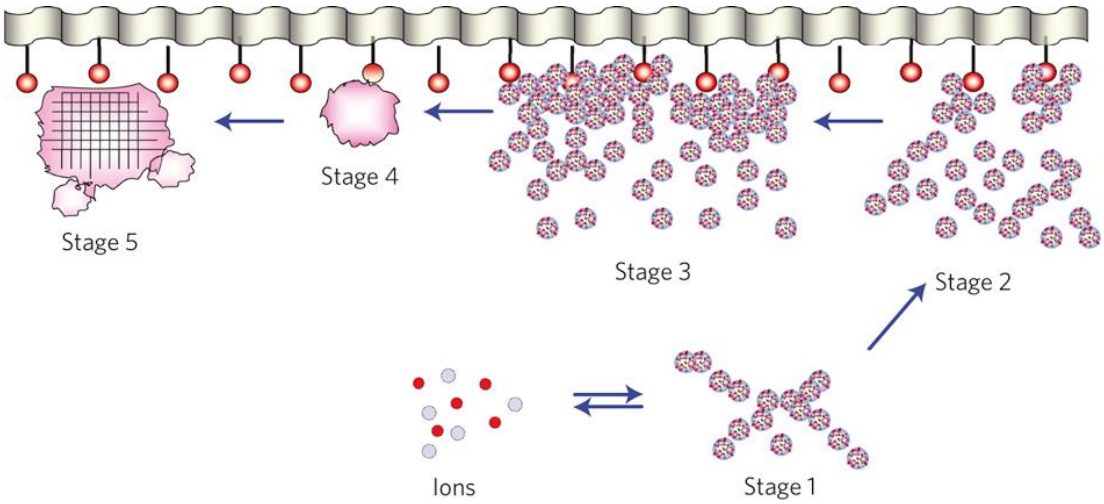

Figure 5.8 Schematic representation of the different stages of surface-directed mineralization of calcium phosphate from SBF at 37 °C. Stage 1: loose aggregation of prenucleation clusters in equilibrium with ions in solution. Stage 2: prenucleation clusters aggregate in the presence of the monolayer with loose aggregates still present in solution. Stage 3: aggregation leads to densification near the monolayer. Stage 4: nucleation of amorphous spherical particles only at the monolayer surface. Stage 5: development of crystallinity following the oriented nucleation directed by the monolayer. (Reproduced from Ref. 242 with permission from Nature Publishing Group)

In order to better demonstrate the effectiveness of the SpDSp-PA hydrogel system as a mimic of the native DPP matrix, we further performed a set of experiments on the biocompatibility, osteogenic differentiation and biomineralization efficiency of Saos-2 cells on these networks.

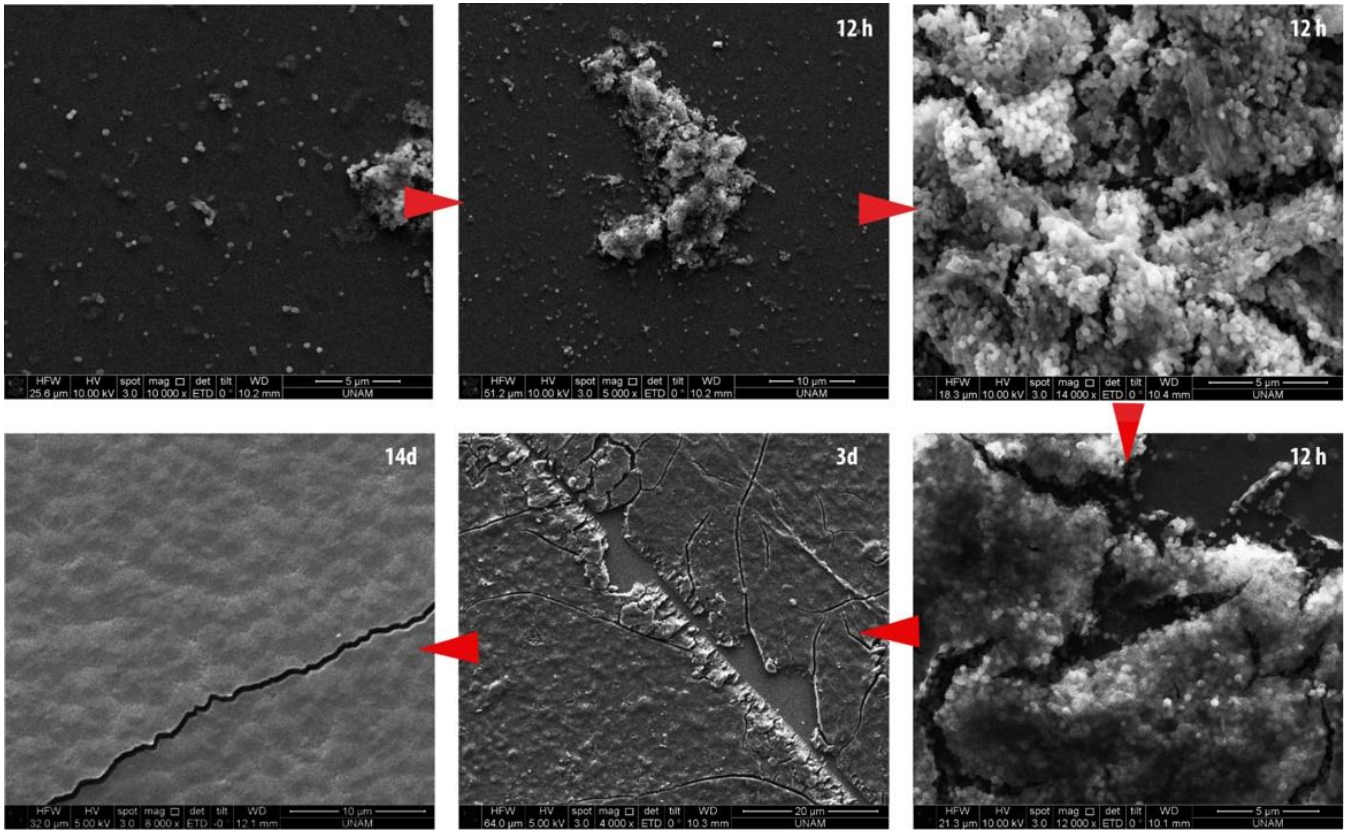

Figure 5.9 CaP mineralization on Ca ion-treated SpDSp-PA hydrogel.

5.3.3 Viability of Saos-2 Cells on DPP-Mimetic PA networks

Biocompatibility of DPP-mimetic PAs was tested with live/dead assay for Saos-2 cells. Cells were viable on all surfaces over a 24 h period. No significant difference was observed between the viability of cells on different peptide nanofiber scaffolds and bare tissue culture plate (TCP), suggesting that the peptide nanofibers provided a biocompatible environment for cellular survival (Figures 5.10 and 5.11).

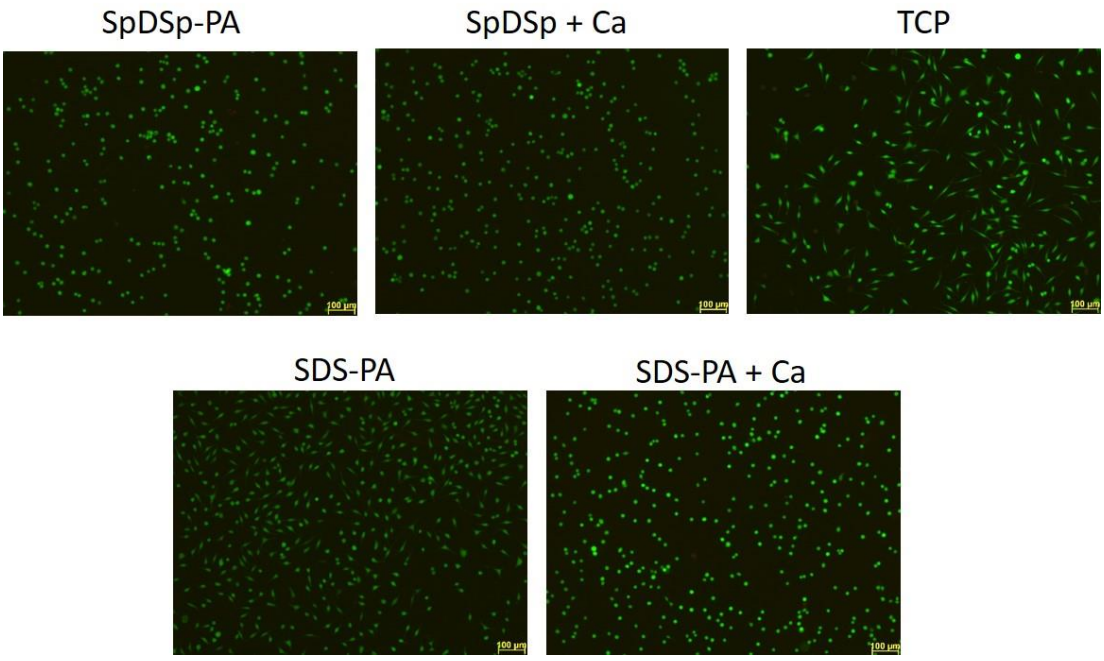

Figure 5.10 Viability of Saos-2 cells cultured on peptide nanofibers and uncoated surface (TCP), as analyzed by calcein-ethidium homodimer live−dead assay.

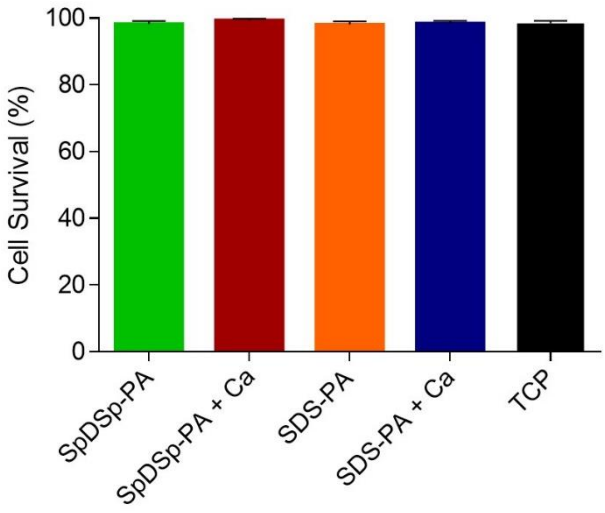

Figure 5.11 Viability of Saos-2 cells cultured on peptide nanofibers and uncoated surfaces (TCP), as analyzed by calcein-ethidium homodimer live−dead assay.

5.3.4 Molecular Analysis of Osteogenic Differentiation Markers

The differentiation of progenitor cells into the osteogenic lineage is regulated by the expression of specific marker genes such as transcription factors, adhesion molecules and proteins of the ECM [237]. Here, expressions of the osteogenic markers Runt-related transcription factor 2 (Runx2), type I collagen (collagen I) and osteopontin were studied on day 7 in both osteogenic medium and maintenance medium groups. Runx2 is often referred to as the key regulator of osteogenic differentiation [181, 182] and its expression is typically analyzed during the early phases of osteogenic differentiation. In the osteogenic medium group, the expression of Runx2 was upregulated when cells were cultured on Ca ion-treated SpDSp-PA nanofibers compared to cells on non-treated SpDSp-PA and SDS-PA nanofibers, Ca ion-treated SDS-PA nanofibers and bare TCP surfaces by ~2.56, ~3.15, ~1.06 and ~3.41 folds, respectively (Figure 5.12).

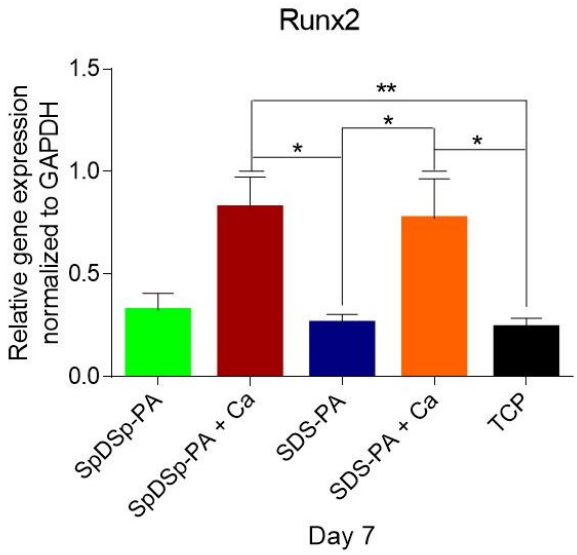

Figure 5.12 Molecular analysis of osteogenic differentiation in osteogenic medium. Gene expression analysis of Runx2. The level of Runx2 gene expression was normalized to GAPDH. Values represent mean ± SEM (**$p < 0.01$, *$p < 0.05$).

The expression of Runx2 was also enhanced on Ca ion-treated SDS-PA nanofibers compared to non-treated SDS-PA and TCP groups by ~2.96 and ~3.2 folds, respectively (Figure 5.12). Early stage mineral deposition of a collagen matrix acts as a template for mineralization and serves as a marker for osteogenic differentiation [183]. The expression of collagen I was significantly upregulated when Saos-2 cells were cultured on Ca ion-treated SpDSp-PA nanofibers compared to cells on non-treated SpDSp-PA and SDS-PA nanofibers and bare TCP surfaces by ~2.51, ~5.33 and ~12.80 folds, respectively (Figure 5.13). The expression of collagen I was also enhanced by ~1.64 fold on Ca ion-treated SpDSp-PA peptide nanofibers compared to Ca ion-treated SDS-PA group (Figure 5.13).

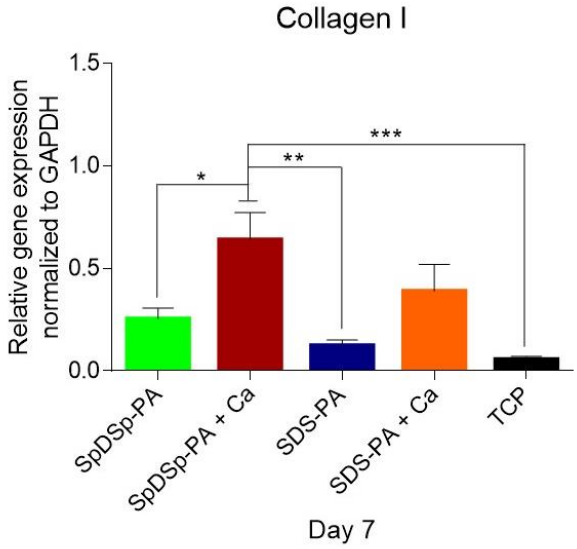

Figure 5.13 Molecular analysis of osteogenic differentiation in osteogenic medium. Gene expression analysis of collagen I. The level of collagen I gene expression was normalized to GAPDH. Values represent mean ± SEM (***p < 0.001, **p < 0.01, *p < 0.05).

In addition to collagen I, several non-collagenous proteins have crucial roles in the formation and maturation of mineralized tissues. Osteopontin is one of the most notable among these proteins and is a highly phosphorylated sialoprotein that occurs as a prominent component of the mineralized extracellular matrices of bones [162]. The osteopontin expression of cells on Ca ion-treated SpDSp-PA nanofibers was also significantly higher compared to cells on non-treated SpDSp-PA and SDS-PA nanofibers and bare TCP surfaces by ~2.72, ~4.12 and ~6.8 folds, respectively (Figure 5.14). The expression of osteopontin was likewise enhanced by ~1.43 fold on Ca ion-treated SpDSp-PA nanofibers compared to Ca ion-treated SDS-PA group (Figure 5.14), which in turn exhibited a ~4.75 fold increase in osteopontin expression compared to TCP (Figure 5.14).

Dentin matrix protein 1 (DMP1) is an acidic phosphoprotein that is also present in mineralized tissues and plays an important role in both the intra- and extracellular bio-mineralization process of osteoblasts and odontoblasts [238-240]. DMP1 expression was also examined on day 14, and ICC stainings showed that cells on Ca ion-treated SpDSp-PA nanofibers showed DMP1 staining (Figure 5.15).

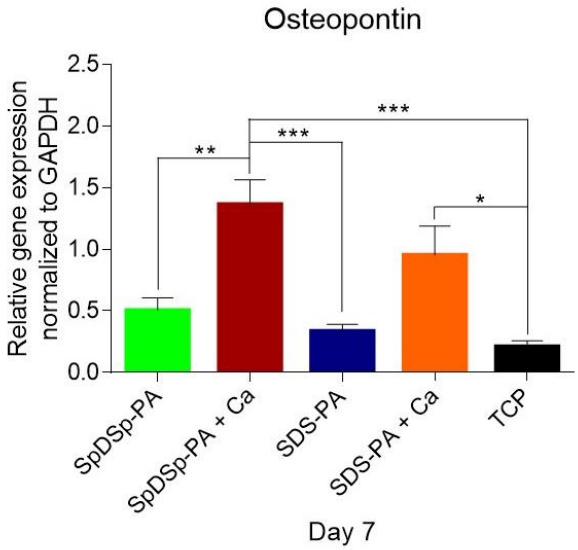

Figure 5.14 Molecular analysis of osteogenic differentiation in osteogenic medium. Gene expression analysis of osteopontin. The level of osteopontin gene expression was normalized to GAPDH. Values represent mean ± SEM (***$p < 0.001$, **$p < 0.01$, *$p < 0.05$).

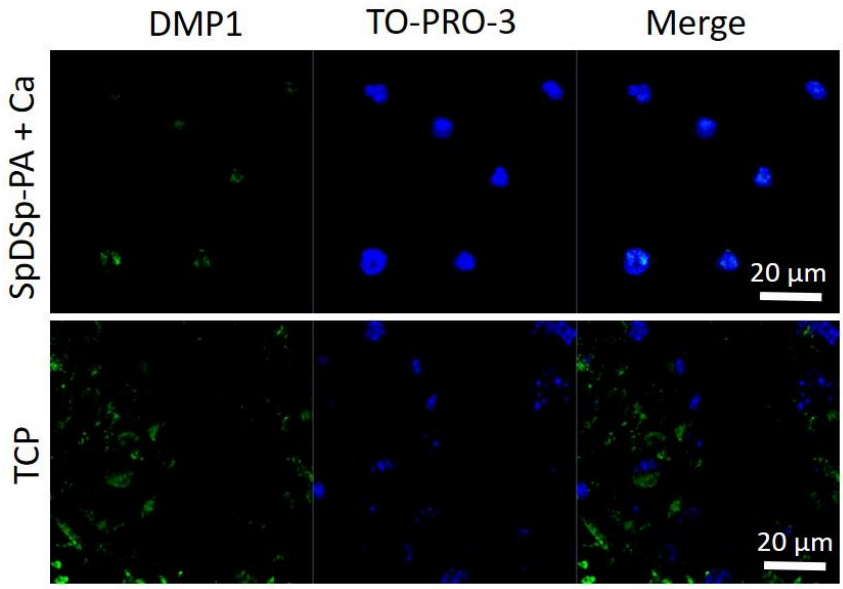

Figure 5.15 Confocal images of DMP-1 immunostaining in osteogenic medium on day 14. Green shows DMP-1, and blue shows the nucleus.

In maintenance medium, the expression of Runx2 was significantly upregulated on Ca ion-treated SpDSp-PA nanofibers compared to cells on non-treated SpDSp-PA and SDS-PA nanofibers, Ca ion-treated SDS-PA nanofibers and bare TCP surfaces by ~9.26, ~6.51, ~3.66 and ~22 folds, respectively. The expression of Runx2 was also significantly enhanced by ~6 folds on Ca ion-treated SDS-PA nanofibers compared to TCP group (Figure 5.16). Similarly, the expression of collagen I was significantly upregulated when cells were cultured on Ca ion-treated SpDSp-PA nanofibers compared to cells on non-treated SpDSp-PA and SDS-PA nanofibers, Ca ion-treated SDS-PA nanofibers and bare TCP surfaces by ~7.33, ~14.6, ~2.07 and ~25.14 folds, respectively (Figure 5.17).

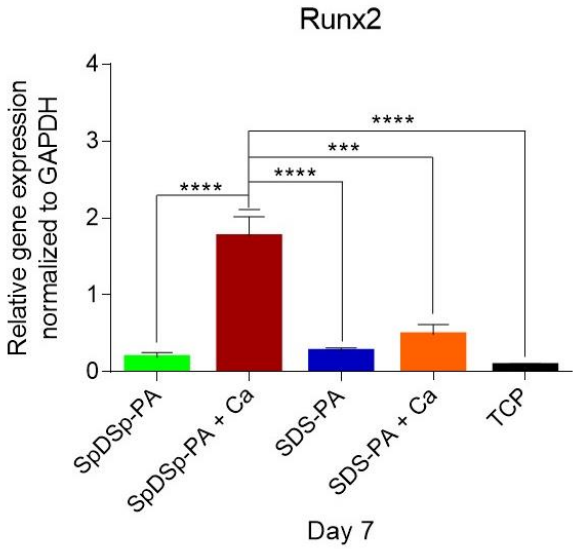

Figure 5.16 Molecular analysis of osteogenic differentiation in maintenance medium. Gene expression analysis of Runx2. The level of Runx2 gene expression was normalized to GAPDH. Values represent mean ± SEM (****p < 0.0001, ***p < 0.001).

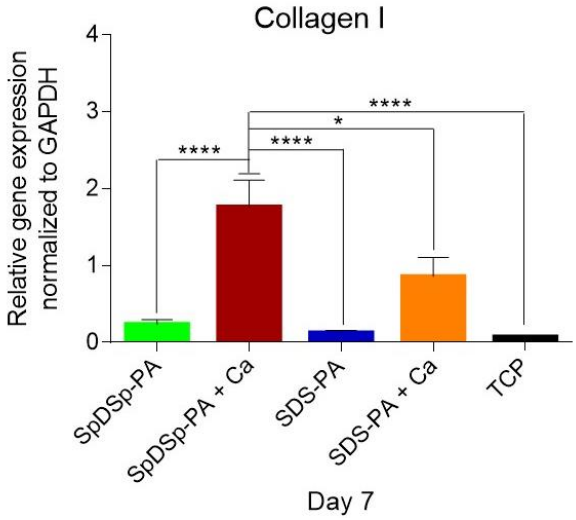

Figure 5.17 Molecular analysis of osteogenic differentiation in maintenance medium. Gene expression analysis of collagen I. The level of collagen I gene expression was normalized to GAPDH. Values represent mean ± SEM (****p < 0.0001, *p < 0.05).

The expression of osteopontin was also upregulated when cells were cultured on Ca ion-treated SpDSp-PA nanofibers compared to cells on non-treated SpDSp-PA and SDS-PA peptide nanofibers, Ca ion-treated SDS-PA nanofibers and bare TCP surfaces by ~5.6, ~2.2, ~1.25 and ~4.29 folds, respectively (Figure 5.18). The expression of osteopontin was also significantly enhanced on Ca ion-treated SDS-PA nanofibers compared to TCP group by ~3.41 folds (Figure 5.18).

DMP1 staining results were found to support the gene expression profiles, with cells on Ca ion-treated SpDSp-PA showing enhanced DMP1 expression, while the TCP group did not show any staining (Figure 5.19).

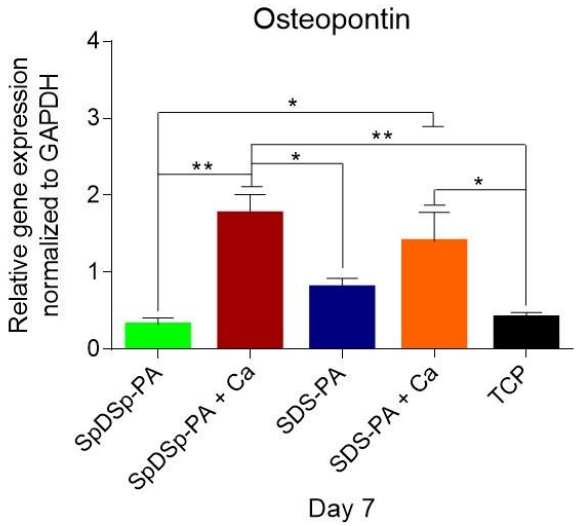

Figure 5.18 Molecular analysis of osteogenic differentiation in maintenance medium. Gene expression analysis of osteopontin. The level of osteopontin gene expression was normalized to GAPDH. Values represent mean ± SEM (**$p < 0.01$, *$p < 0.05$).

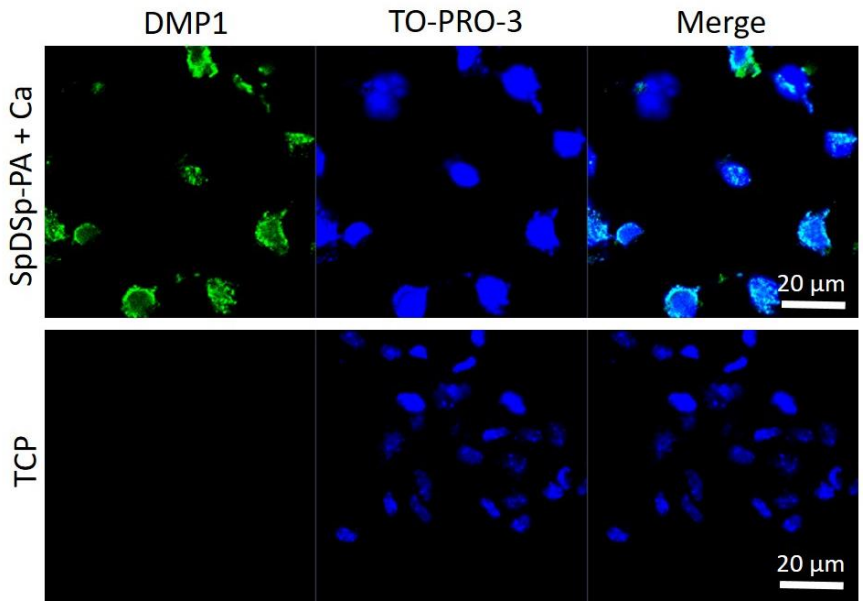

Figure 5.19 Confocal images of DMP-1 immunostaining in maintenance medium on day 14. Green shows DMP-1, and blue shows the nucleus.

5.3.5 Mineral Deposition of Saos-2 Cells on DPP-Mimetic PA networks

Effect of peptides on cellular mineralization was investigated through Alizarin red staining. On day 7, cells cultured on Ca ion-treated SpDSp-PA hydrogel showed enhanced mineralization compared to SpDSp-PA and non-phosphorylated SDS-PA networks (Figures 5.20 and 5.21). On day 14, all groups exhibited Alizarin red staining (Figure 5.22). Early calcium deposition on Ca-treated SpDSp-PA hydrogel system and its significantly higher mineral deposition compared to other groups over a 14 day period (Figures 5.21 and 5.23) indicate the importance of scaffold formation and presence of phosphoryl groups for the biomineralization process.

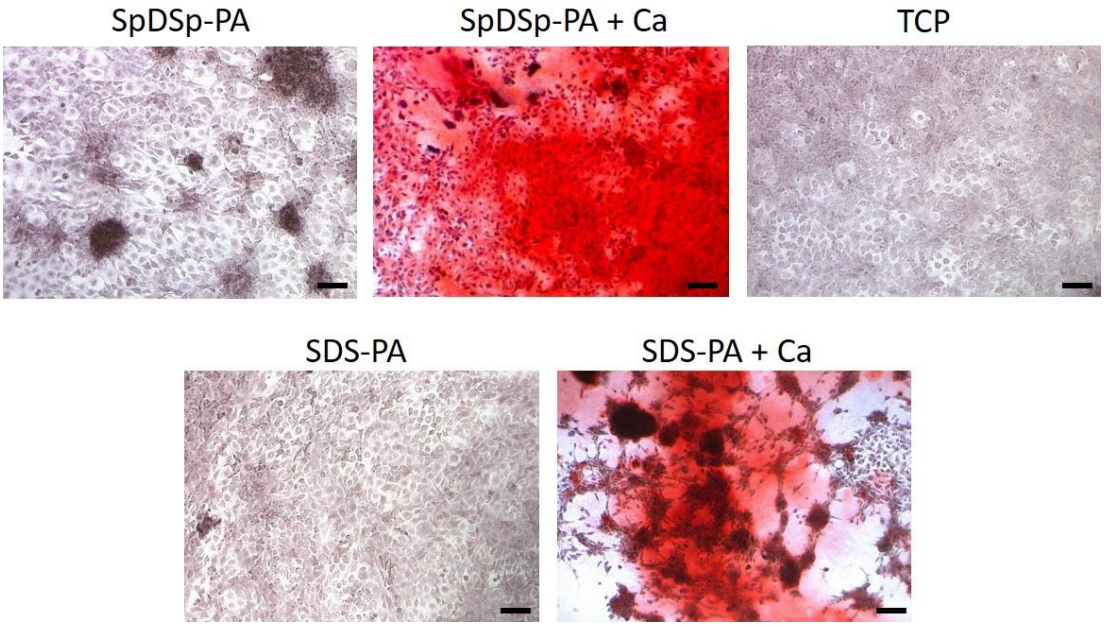

Figure 5.20 Biomineralization of Saos-2 cells on DPP-mimetic PA nanofibers and TCP on day 7, as demonstrated by Alizarin red staining. Scale bars are 100 µm.

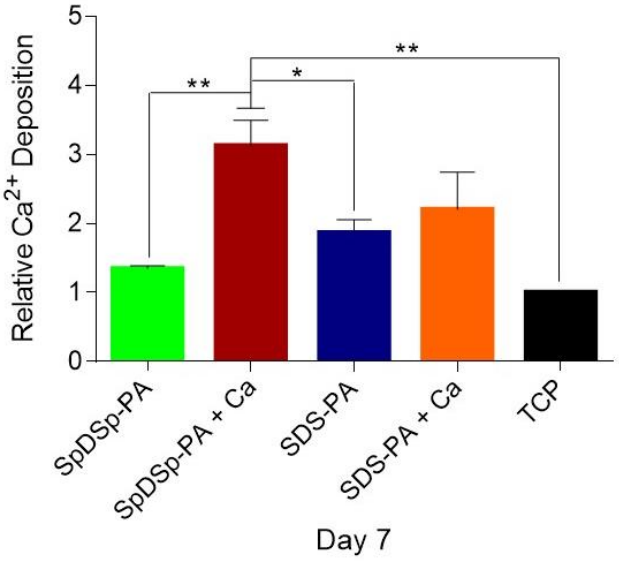

Figure 5.21 Quantification of Ca^{2+} deposition on DPP-mimetic PA nanofibers and uncoated TCP surfaces on day 7, ***p < 0.01*.

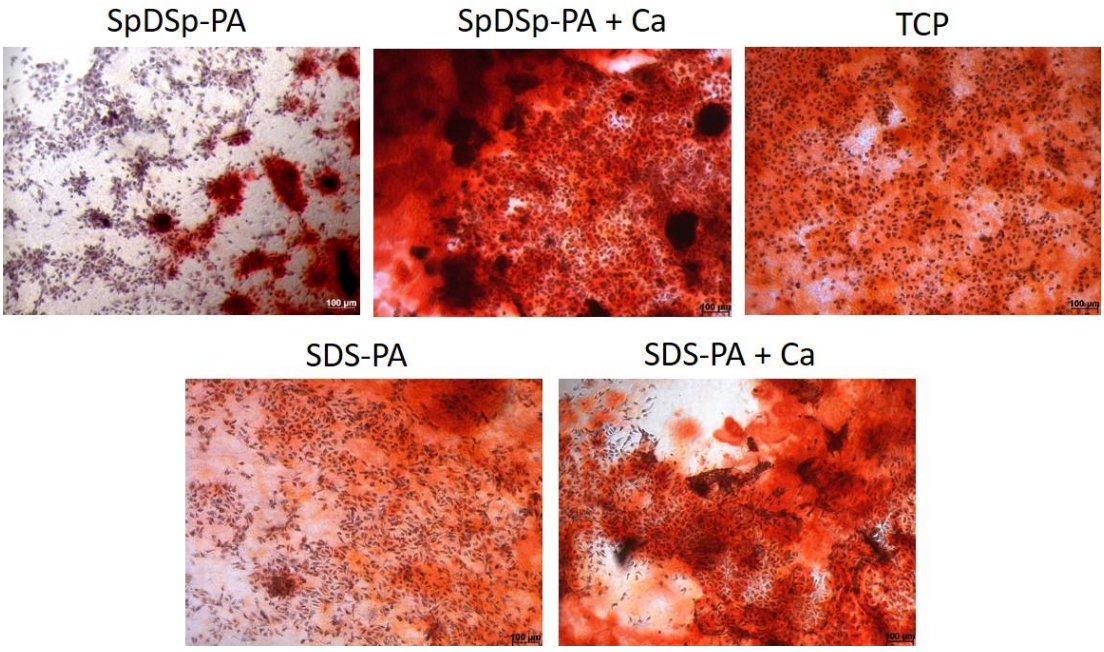

Figure 5.22 Biomineralization of Saos-2 cells on DPP-mimetic PA nanofibers and TCP on day 14, as demonstrated by Alizarin red staining. Scale bars are 100 µm.

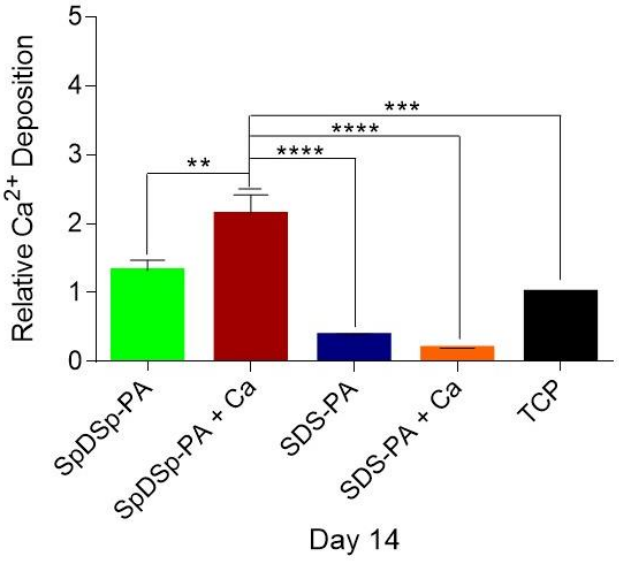

Figure 5.23 Quantification of Ca^{2+} deposition on DPP-mimetic PA nanofibers and uncoated TCP surfaces on day 14, $^{**}p < 0.01$, $^{***}p < 0.001$, $^{****}p < 0.0001$.

5.4 Conclusion

In this study, we designed a DPP-mimetic peptide network system that can mediate its self-assembly and biomineralization capacity through the phosphorylation status of its serine residues. In contrast, the soluble SpDSp-PA and gelous-but-not-phosphorylated SDS-PA both failed to facilitate mineral deposition. This suggests that the presence of phosphoryl groups and the nanofibrous composition of the peptide matrix are both vital for the biomineralization process. SpDSp-PA and SDS-PA also supported the viability of osteogenic cells, and the ability of Ca-treated SpDSp-PA to induce biomineralization of Saos-2 cells may be utilized to develop new treatments for the assisted repair of bone and tooth defects. In addition, this study will be helpful to understand the complicated process of bone and tooth mineralization and the regulator factors responsible for effecting it.

Chapter 6

6. Conclusion and Future Prospects

The global incidence of bone diseases and disorders has shown a steeply upward trend. Taking into account the serious limitation of conventional therapies, nanomaterials may promote new strategies in bone regeneration. Nanostructured scaffolds can better mimic the nanostructural architecture found in natural extracellular matrix environments and regulate cell proliferation, differentiation, and migration to efficiently stimulate new bone formation.

Molecular self-assembly presents a very attractive strategy to build nanoscale materials and the structural features of the final assemblies can be readily and finely tuned by molecular structure, environmental factors (pH, solvents, coassembling molecules, and temperature), and assembly kinetics. With their inherent biocompatibility and biodegradability, peptides have been recognized as very useful building blocks for creating self-assembling nanostructures for medical applications. Among these, peptide amphiphile molecules combine the structural features of amphiphilic surfactants with the functions of bioactive peptides, and are known to assemble into a variety of nanostructures. This thesis describes the formation of different nanofibrous scaffolds from self-assembled PAs to induce *in vitro* osteogenic differentiation and *in vivo* bone regeneration, in addition to *in vitro* and *in vivo* biomineralization.

In the first study, we developed a bone extracellular matrix-mimetic nanofibrous network system by self-assembly. Glycosaminoglycans play key roles in bone regeneration and mineralization, and glycosaminoglycan-mimetic peptide nanofibers

were synthesized by utilizing the chemical groups found in glycosaminoglycans of the bone extracellular matrix. Cellular experiments showed that glycosaminoglycan-mimetic peptide nanofibers provided a biocompatible microenvironment for stem cell growth, and rat mesenchymal stem cells (rMSCs) cultured on these nanofibers exhibited enhanced osteogenic potential, as measured by alkaline phosphatase activity, osteogenic gene expression and calcium deposition. Moreover, the effect of bioactive peptide nanofibers on mineralization were investigated *in vivo* using a rabbit tibial defect model. Glycosaminoglycan-mimetic peptide nanofiber gels (GAG-PA gels) were placed into cylindrical defects generated by surgical methods in rabbit tibiae, and surgical defects were analyzed 4 weeks following scaffold implantation. Micro-Computed Tomography measurements revealed that the regenerated tissue in GAG-PA gel-treated bone defects was predominated by cortical bone and had a greater mineral density compared to physiological saline-treated sham group. Histological analyses also showed that bone defects were filled with a more compact form of bone after GAG-PA gel treatment. In addition, the defect gap was bridged to a greater extent in the GAG-PA gel treated group. This work shows that glycosaminoglycan-mimetic peptide nanofibers exhibit considerable potential for clinical applications in bone defect repair, as they effectively facilitate the differentiation of rMSCs to osteoblasts and enhance bone formation under *in vivo* conditions.

The motivation of the second study was to investigate the effect of osteoinductive peptide nanofibers on the osteogenic differentiation of rMSCs. For this purpose, we synthesized and used E_3-PA molecules bearing the Glu-Glu-Glu (EEE) motif, which was derived from a non-collagenous matrix protein of bone tissue. Here, we showed

that rMSCs on E_3/K_3-PA nanofibers differentiated effectively into mature osteoblasts, and extensively deposited minerals compared to gelatin and TCP control groups.

The third study was about the development of a mineralized peptide nanofiber scaffold system through template-directed mineralization, and we investigated the effect of this system on the osteogenic differentiation ability of Saos-2 cells. Hydroxyapatite formation on PA nanofibers was identified through XRD measurements, while morphological changes during the formation, nucleation and growth of hydroxyapatite minerals were examined by TEM. We found that mineralized peptide nanofibers were mechanically superior compared to non-mineralized counterparts, and cellular experiments demonstrated that the presence of HA in PA nanofibers stimulates osteogenic differentiation.

The last study discussed in this thesis was the design and development of a dentin-phosphoprotein mimetic peptide amphiphile and its self-assembly through ionic interactions with calcium ions. An *in vitro* mineralization test was also performed to investigate the effectiveness of phosphorylation on biomineralization. The failure of non-phosphorylated SDS-PA networks in facilitating the mineral deposition despite their nanofibrous structure suggests that phosphoryl residues and scaffold formation are both critical for the formation of hydroxyapatite. As SpDSp-PA hydrogels also supported the survival and biomineralization of Saos-2 cells, the hydrogel system described here shows great promise to be used in the further investigations of the dental and bone biomineralization process, potentially involving a combination of cellular, mineral and protein hydrogel components.

In conclusion, we presented a wide range of applications based around the induction of biomineralization and bone tissue regeneration by bioactive PA scaffolds. We

investigated the cellular changes that occur in the presence and absence of PA matrices at morphological, protein and gene expression levels. Overall, there are several clinical conditions that require the enhancement of bone regeneration either locally or systemically, and there are many issues of efficacy, safety and cost to be addressed before the general clinical application of biomaterials designed for bone repair. Emulation of the normal cascade of bone formation is an effective strategy for exerting precise control over bone regeneration, and shows great promise for the successful management of conditions that result from bone disorders and require bone repair. Research is ongoing within all described fields to enhance bone regeneration and biomineralization, and it is hoped that optimal outcomes will be obtained in future clinical applications of biomimetic nanofibrous scaffolds.

Bibliography

[1] M. M. Stevens, "Biomaterials for bone tissue engineering," *Materials today,* vol. 11, pp. 18-25, 2008.

[2] R. S. Taichman, "Blood and bone: two tissues whose fates are intertwined to create the hematopoietic stem-cell niche," *Blood,* vol. 105, pp. 2631-2639, 2005.

[3] P. Fratzl and R. Weinkamer, "Hierarchical structure and repair of bone: deformation, remodelling, healing," in *Self Healing Materials*, ed: Springer, 2007, pp. 323-335.

[4] X. Wang, S. Xu, S. Zhou, W. Xu, M. Leary, P. Choong*, et al.*, "Topological design and additive manufacturing of porous metals for bone scaffolds and orthopaedic implants: A review," *Biomaterials,* vol. 83, pp. 127-141, 2016.

[5] U. Kini and B. Nandeesh, "Physiology of bone formation, remodeling, and metabolism," in *Radionuclide and hybrid bone imaging*, ed: Springer, 2012, pp. 29-57.

[6] P. Fratzl and R. Weinkamer, "Nature's hierarchical materials," *Progress in Materials Science,* vol. 52, pp. 1263-1334, 2007.

[7] J.-Y. Rho, L. Kuhn-Spearing, and P. Zioupos, "Mechanical properties and the hierarchical structure of bone," *Medical engineering & physics,* vol. 20, pp. 92-102, 1998.

[8] P. Fratzl, H. Gupta, E. Paschalis, and P. Roschger, "Structure and mechanical quality of the collagen–mineral nano-composite in bone," *Journal of materials chemistry,* vol. 14, pp. 2115-2123, 2004.

[9] T. Hassenkam, G. E. Fantner, J. A. Cutroni, J. C. Weaver, D. E. Morse, and P. K. Hansma, "High-resolution AFM imaging of intact and fractured trabecular bone," *Bone,* vol. 35, pp. 4-10, 2004.

[10] F. Long, "Building strong bones: molecular regulation of the osteoblast lineage," *Nature reviews Molecular cell biology,* vol. 13, pp. 27-38, 2012.

[11] H. R. Dudley and D. Spiro, "The fine structure of bone cells," *The Journal of biophysical and biochemical cytology,* vol. 11, pp. 627-649, 1961.

[12] J. Pritchard, "A cytological and histochemical study of bone and cartilage formation in the rat," *Journal of anatomy,* vol. 86, p. 259, 1952.

[13] L. F. Bonewald, "The amazing osteocyte," *Journal of Bone and Mineral Research,* vol. 26, pp. 229-238, 2011.

[14] W. J. Boyle, W. S. Simonet, and D. L. Lacey, "Osteoclast differentiation and activation," *Nature,* vol. 423, pp. 337-342, 2003.

[15] S. L. Teitelbaum and F. P. Ross, "Genetic regulation of osteoclast development and function," *Nature Reviews Genetics,* vol. 4, pp. 638-649, 2003.

[16] S. L. Teitelbaum, "Bone resorption by osteoclasts," *Science,* vol. 289, pp. 1504-1508, 2000.

[17] R. Cancedda, "Cartilage and bone extracellular matrix," *Current pharmaceutical design,* vol. 15, pp. 1334-1348, 2009.

[18] R. Florencio-Silva, G. R. d. S. Sasso, E. Sasso-Cerri, M. J. Simões, and P. S. Cerri, "Biology of bone tissue: structure, function, and factors that influence bone cells," *BioMed research international,* vol. 2015, 2015.

[19] A. K. Gaharwar, A. Arpanaei, T. L. Andresen, and A. Dolatshahi-Pirouz, "3D Biomaterial Microarrays for Regenerative Medicine: Current State-of-the-Art,

Emerging Directions and Future Trends," *Advanced Materials,* vol. 28, pp. 771-781, 2016.
[20] B. Brodsky and A. V. Persikov, "Molecular structure of the collagen triple helix," *Advances in protein chemistry,* vol. 70, pp. 301-339, 2005.
[21] B. Clarke, "Normal bone anatomy and physiology," *Clinical journal of the American Society of Nephrology,* vol. 3, pp. S131-S139, 2008.
[22] D. Heinegard and A. Oldberg, "Glycosylated matrix proteins," *Connective Tissue and its Heritable Disorders-Molecular, Genetics and Medical Aspects,* pp. 189-209, 1993.
[23] M. F. Young, J. M. Kerr, K. Ibaraki, A.-M. Heegaard, and P. G. Robey, "Structure, expression, and regulation of the major noncollagenous matrix proteins of bone," *Clinical orthopaedics and related research,* vol. 281, pp. 275-294, 1992.
[24] J. W. Poser, F. S. Esch, N. C. Ling, and P. A. Price, "Isolation and sequence of the vitamin K-dependent protein from human bone. Undercarboxylation of the first glutamic acid residue," *Journal of Biological Chemistry,* vol. 255, pp. 8685-8691, 1980.
[25] P. A. Price, J. D. Fraser, and G. Metz-Virca, "Molecular cloning of matrix Gla protein: implications for substrate recognition by the vitamin K-dependent gamma-carboxylase," *Proceedings of the National Academy of Sciences,* vol. 84, pp. 8335-8339, 1987.
[26] M. E. Bolander, M. F. Young, L. W. Fisher, Y. Yamada, and J. D. Termine, "Osteonectin cDNA sequence reveals potential binding regions for calcium and hydroxyapatite and shows homologies with both a basement membrane protein (SPARC) and a serine proteinase inhibitor (ovomucoid)," *Proceedings of the National Academy of Sciences,* vol. 85, pp. 2919-2923, 1988.
[27] J. Engel, W. Taylor, M. Paulsson, H. Sage, and B. Hogan, "Calcium binding domains and calcium-induced conformational transition of SPARC/BM-40/osteonectin, an extracellular glycoprotein expressed in mineralized and nonmineralized tissues," *Biochemistry,* vol. 26, pp. 6958-6965, 1987.
[28] A. Oldberg, A. Franzén, and D. Heinegård, "Cloning and sequence analysis of rat bone sialoprotein (osteopontin) cDNA reveals an Arg-Gly-Asp cell-binding sequence," *Proceedings of the National Academy of Sciences,* vol. 83, pp. 8819-8823, 1986.
[29] L. Fisher, O. McBride, J. Termine, and M. Young, "Human bone sialoprotein. Deduced protein sequence and chromosomal localization," *Journal of Biological Chemistry,* vol. 265, pp. 2347-2351, 1990.
[30] A. Oldberg, A. Franzen, and D. Heinegaard, "The primary structure of a cell-binding bone sialoprotein," *Journal of Biological Chemistry,* vol. 263, pp. 19430-19432, 1988.
[31] H. Orimo, "The mechanism of mineralization and the role of alkaline phosphatase in health and disease," *Journal of Nippon Medical School,* vol. 77, pp. 4-12, 2010.
[32] G. K. Hunter and H. A. Goldberg, "Nucleation of hydroxyapatite by bone sialoprotein," *Proceedings of the National Academy of Sciences,* vol. 90, pp. 8562-8565, 1993.
[33] K. Hultenby, F. P. Reinholt, Å. Oldberg, and D. Heinegård, "Ultrastructural immunolocalization of osteopontin in metaphyseal and cortical bone," *Matrix,* vol. 11, pp. 206-213, 1991.
[34] D. E. Robinson, D. J. Buttle, R. D. Short, S. L. McArthur, D. A. Steele, and J. D. Whittle, "Glycosaminoglycan (GAG) binding surfaces for characterizing GAG-protein interactions," *Biomaterials,* vol. 33, pp. 1007-1016, 2012.

[35] K. Grande-Allen, N. Osman, M. Ballinger, H. Dadlani, S. Marasco, and P. Little, "Glycosaminoglycan synthesis and structure as targets for the prevention of calcific aortic valve disease," *Cardiovascular research,* vol. 76, pp. 19-28, 2007.
[36] H. E. Bülow and O. Hobert, "The molecular diversity of glycosaminoglycans shapes animal development," *Annu. Rev. Cell Dev. Biol.,* vol. 22, pp. 375-407, 2006.
[37] B. Yue, "Biology of the extracellular matrix: an overview," *Journal of glaucoma,* vol. 23, p. S20, 2014.
[38] A. P. Spicer, J. L. Tien, A. Joo, and R. A. Bowling Jr, "Investigation of hyaluronan function in the mouse through targeted mutagenesis," *Glycoconjugate journal,* vol. 19, pp. 341-345, 2002.
[39] T. Ulaganathan, R. Shi, D. Yao, R.-X. Gu, M.-L. Garron, M. Cherney*, et al.*, "Conformational Flexibility of PL12 family Heparinases: Structure and Substrate Specificity of Heparinase III from Bacteroides thetaiotaomicron (BT4657)," *Glycobiology,* p. cww096, 2016.
[40] R. Sasisekharan, R. Raman, and V. Prabhakar, "Glycomics approach to structure-function relationships of glycosaminoglycans," *Annu. Rev. Biomed. Eng.,* vol. 8, pp. 181-231, 2006.
[41] K. Sugahara and H. Kitagawa, "Heparin and heparan sulfate biosynthesis," *IUBMB life,* vol. 54, pp. 163-175, 2002.
[42] J. E. Silbert and G. Sugumaran, "Biosynthesis of chondroitin/dermatan sulfate," *IUBMB life,* vol. 54, pp. 177-186, 2002.
[43] J. L. Funderburgh, "Keratan sulfate biosynthesis," *IUBMB life,* vol. 54, pp. 187-194, 2002.
[44] N. Itano and K. Kimata, "Mammalian hyaluronan synthases," *IUBMB life,* vol. 54, pp. 195-199, 2002.
[45] N. S. Gandhi and R. L. Mancera, "The structure of glycosaminoglycans and their interactions with proteins," *Chemical biology & drug design,* vol. 72, pp. 455-482, 2008.
[46] R. E. Hileman, J. R. Fromm, J. M. Weiler, and R. J. Linhardt, "Glycosaminoglycan-protein interactions: definition of consensus sites in glycosaminoglycan binding proteins," *Bioessays,* vol. 20, pp. 156-167, 1998.
[47] S. Misra, V. C. Hascall, I. Atanelishvili, R. Moreno Rodriguez, R. R. Markwald, and S. Ghatak, "Utilization of glycosaminoglycans/proteoglycans as carriers for targeted therapy delivery," *International journal of cell biology,* vol. 2015, 2015.
[48] K. M. Cadigan, "Regulating morphogen gradients in the Drosophila wing," in *Seminars in cell & developmental biology*, 2002, pp. 83-90.
[49] F. Lamoureux, M. Baud'huin, L. Duplomb, D. Heymann, and F. Rédini, "Proteoglycans: key partners in bone cell biology," *Bioessays,* vol. 29, pp. 758-771, 2007.
[50] V. Devescovi, E. Leonardi, G. Ciapetti, and E. Cenni, "Growth factors in bone repair," *La Chirurgia degli organi di movimento,* vol. 92, pp. 161-168, 2008.
[51] K. N. Malizos and L. K. Papatheodorou, "The healing potential of the periosteum: molecular aspects," *Injury,* vol. 36, pp. S13-S19, 2005.
[52] W. Landis, "The strength of a calcified tissue depends in part on the molecular structure and organization of its constituent mineral crystals in their organic matrix," *Bone,* vol. 16, pp. 533-544, 1995.
[53] H. C. Anderson, "Matrix vesicles and calcification," *Current rheumatology reports,* vol. 5, pp. 222-226, 2003.

[54] J. R. Porter, T. T. Ruckh, and K. C. Popat, "Bone tissue engineering: a review in bone biomimetics and drug delivery strategies," *Biotechnology Progress,* vol. 25, pp. 1539-1560, 2009.
[55] G. F. Rogers and A. K. Greene, "Autogenous bone graft: basic science and clinical implications," *Journal of Craniofacial Surgery,* vol. 23, pp. 323-327, 2012.
[56] E. D. Arrington, W. J. Smith, H. G. Chambers, A. L. Bucknell, and N. A. Davino, "Complications of iliac crest bone graft harvesting," *Clinical orthopaedics and related research,* vol. 329, pp. 300-309, 1996.
[57] J. Nishida and T. Shimamura, "Methods of reconstruction for bone defect after tumor excision: a review of alternatives," *Medical Science Monitor,* vol. 14, pp. RA107-RA113, 2008.
[58] C.-H. Hou, R.-S. Yang, and S.-M. Hou, "Hospital-based allogenic bone bank—10-year experience," *Journal of Hospital Infection,* vol. 59, pp. 41-45, 2005.
[59] N. Shibuya and D. C. Jupiter, "Bone graft substitute: allograft and xenograft," *Clinics in podiatric medicine and surgery,* vol. 32, pp. 21-34, 2015.
[60] D. Yoo and A. Giulivi, "Xenotransplantation and the potential risk of xenogeneic transmission of porcine viruses," *Canadian Journal of Veterinary Research,* vol. 64, p. 193, 2000.
[61] C. T. Laurencin and S. F. El-Amin, "Xenotransplantation in orthopaedic surgery," *Journal of the American Academy of Orthopaedic Surgeons,* vol. 16, pp. 4-8, 2008.
[62] F. Matassi, L. Nistri, D. C. Paez, and M. Innocenti, "New biomaterials for bone regeneration," *Clinical cases in mineral and bone metabolism,* vol. 8, pp. 21-24, 2011.
[63] J. D. Kretlow and A. G. Mikos, "Review: mineralization of synthetic polymer scaffolds for bone tissue engineering," *Tissue engineering,* vol. 13, pp. 927-938, 2007.
[64] R. Langer and J. Vacanti, "Tissue engineering," *Science,* vol. 260, pp. 920-926, 1993.
[65] R. F. Service, "Tissue engineers build new bone," *Science (New York, NY),* vol. 289, p. 1498, 2000.
[66] D. Howard, L. D. Buttery, K. M. Shakesheff, and S. J. Roberts, "Tissue engineering: strategies, stem cells and scaffolds," *Journal of anatomy,* vol. 213, pp. 66-72, 2008.
[67] N. Kimelman, G. Pelled, Z. Gazit, and D. Gazit, "Applications of gene therapy and adult stem cells in bone bioengineering," 2006.
[68] D. Logeart-Avramoglou, F. Anagnostou, R. Bizios, and H. Petite, "Engineering bone: challenges and obstacles," *Journal of cellular and molecular medicine,* vol. 9, pp. 72-84, 2005.
[69] J. van den Dolder, E. Farber, P. H. Spauwen, and J. A. Jansen, "Bone tissue reconstruction using titanium fiber mesh combined with rat bone marrow stromal cells," *Biomaterials,* vol. 24, pp. 1745-1750, 2003.
[70] J. R. Mauney, V. Volloch, and D. L. Kaplan, "Role of adult mesenchymal stem cells in bone tissue engineering applications: current status and future prospects," *Tissue engineering,* vol. 11, pp. 787-802, 2005.
[71] M. Richards, B. A. Huibregtse, A. I. Caplan, J. A. Goulet, and S. A. Goldstein, "Marrow-derived progenitor cell injections enhance new bone formation during distraction," *Journal of Orthopaedic Research,* vol. 17, pp. 900-908, 1999.
[72] K. Lee, E. A. Silva, and D. J. Mooney, "Growth factor delivery-based tissue engineering: general approaches and a review of recent developments," *Journal of the Royal Society Interface,* vol. 8, pp. 153-170, 2011.

[73] Y.-D. Kim, P. Pofali, T.-E. Park, B. Singh, K. Cho, S. Maharjan*, et al.*, "Gene therapy for bone tissue engineering," *Tissue Engineering and Regenerative Medicine,* vol. 13, pp. 111-125, 2016.

[74] V. I. Sikavitsas, G. N. Bancroft, and A. G. Mikos, "Formation of three-dimensional cell/polymer constructs for bone tissue engineering in a spinner flask and a rotating wall vessel bioreactor," *Journal of biomedical materials research,* vol. 62, pp. 136-148, 2002.

[75] G. N. Bancroft, V. I. Sikavitsas, and A. G. Mikos, "Technical note: Design of a flow perfusion bioreactor system for bone tissue-engineering applications," *Tissue engineering,* vol. 9, pp. 549-554, 2003.

[76] A. Banfi, A. Muraglia, B. Dozin, M. Mastrogiacomo, R. Cancedda, and R. Quarto, "Proliferation kinetics and differentiation potential of ex vivo expanded human bone marrow stromal cells: implications for their use in cell therapy," *Experimental hematology,* vol. 28, pp. 707-715, 2000.

[77] A. Banfi, G. Bianchi, R. Notaro, L. Luzzatto, R. Cancedda, and R. Quarto, "Replicative aging and gene expression in long-term cultures of human bone marrow stromal cells," *Tissue engineering,* vol. 8, pp. 901-910, 2002.

[78] S. P. Bruder, N. Jaiswal, and S. E. Haynesworth, "Growth kinetics, self-renewal, and the osteogenic potential of purified human mesenchymal stem cells during extensive subcultivation and following cryopreservation," *Journal of cellular biochemistry,* vol. 64, pp. 278-294, 1997.

[79] T. Albrektsson and C. Johansson, "Osteoinduction, osteoconduction and osseointegration," *European Spine Journal,* vol. 10, pp. S96-S101, 2001.

[80] S. Cartmell, "Controlled release scaffolds for bone tissue engineering," *Journal of pharmaceutical sciences,* vol. 98, pp. 430-441, 2009.

[81] T. A. Holland and A. G. Mikos, "Review: biodegradable polymeric scaffolds. Improvements in bone tissue engineering through controlled drug delivery," in *Tissue Engineering I*, ed: Springer, 2005, pp. 161-185.

[82] L. L. Hench and J. M. Polak, "Third-generation biomedical materials," *Science,* vol. 295, pp. 1014-1017, 2002.

[83] E. Vögelin, N. Jones, J. Huang, J. Brekke, and J. Lieberman, "Healing of a critical-sized defect in the rat femur with use of a vascularized periosteal flap, a biodegradable matrix, and bone morphogenetic protein," *J Bone Joint Surg Am,* vol. 87, pp. 1323-1331, 2005.

[84] A. K. Burkoth, J. Burdick, and K. S. Anseth, "Surface and bulk modifications to photocrosslinked polyanhydrides to control degradation behavior," *Journal of biomedical materials research,* vol. 51, pp. 352-359, 2000.

[85] K.-W. Lee, S. Wang, L. Lu, E. Jabbari, B. L. Currier, and M. J. Yaszemski, "Fabrication and characterization of poly (propylene fumarate) scaffolds with controlled pore structures using 3-dimensional printing and injection molding," *Tissue engineering,* vol. 12, pp. 2801-2811, 2006.

[86] P. X. Ma and J.-W. Choi, "Biodegradable polymer scaffolds with well-defined interconnected spherical pore network," *Tissue engineering,* vol. 7, pp. 23-33, 2001.

[87] D. J. Mooney, D. F. Baldwin, N. P. Suh, J. P. Vacanti, and R. Langer, "Novel approach to fabricate porous sponges of poly (D, L-lactic-co-glycolic acid) without the use of organic solvents," *Biomaterials,* vol. 17, pp. 1417-1422, 1996.

[88] P. X. Ma and R. Zhang, "Synthetic nano-scale fibrous extracellular matrix," *Journal of biomedical materials research,* vol. 46, pp. 60-72, 1999.

[89] R. Zhang and P. X. Ma, "Poly (a-hydroxyl acids)/hydroxyapatite porous composites for bone-tissue engineering. I. Preparation and morphology," *Journal of biomedical materials research,* vol. 44, pp. 446-455, 1999.

[90] H. Lo, S. Kadiyala, S. Guggino, and K. Leong, "Poly (L-lactic acid) foams with cell seeding and controlled-release capacity," *Journal of biomedical materials research,* vol. 30, pp. 475-484, 1996.

[91] P. J. Ginty, D. Howard, F. R. Rose, M. J. Whitaker, J. J. Barry, P. Tighe*, et al.*, "Mammalian cell survival and processing in supercritical CO2," *Proceedings of the National Academy of Sciences,* vol. 103, pp. 7426-7431, 2006.

[92] J. K. Sherwood, S. L. Riley, R. Palazzolo, S. C. Brown, D. C. Monkhouse, M. Coates*, et al.*, "A three-dimensional osteochondral composite scaffold for articular cartilage repair," *Biomaterials,* vol. 23, pp. 4739-4751, 2002.

[93] G. Gulseren, M. Goktas, H. Ceylan, A. B. Tekinay, and M. O. Guler, "Nanomaterials for Bone Tissue Regeneration and Orthopedic Implants," in *Therapeutic Nanomaterials*, ed: John Wiley & Sons, Inc, 2016, pp. 119-151.

[94] W.-G. Koh, A. Revzin, and M. V. Pishko, "Poly (ethylene glycol) hydrogel microstructures encapsulating living cells," *Langmuir,* vol. 18, pp. 2459-2462, 2002.

[95] V. L. Tsang and S. N. Bhatia, "Three-dimensional tissue fabrication," *Advanced drug delivery reviews,* vol. 56, pp. 1635-1647, 2004.

[96] M. C. Cushing and K. S. Anseth, "Hydrogel cell cultures," *Science,* vol. 316, pp. 1133-1134, 2007.

[97] M. Lutolf, J. Lauer-Fields, H. Schmoekel, A. Metters, F. Weber, G. Fields*, et al.*, "Synthetic matrix metalloproteinase-sensitive hydrogels for the conduction of tissue regeneration: engineering cell-invasion characteristics," *Proceedings of the National Academy of Sciences,* vol. 100, pp. 5413-5418, 2003.

[98] M. P. Lutolf, F. E. Weber, H. G. Schmoekel, J. C. Schense, T. Kohler, R. Müller*, et al.*, "Repair of bone defects using synthetic mimetics of collagenous extracellular matrices," *Nature biotechnology,* vol. 21, pp. 513-518, 2003.

[99] J. Bobyn, G. Stackpool, S. Hacking, M. Tanzer, and J. Krygier, "Characteristics of bone ingrowth and interface mechanics of a new porous tantalum biomaterial," *Bone & Joint Journal,* vol. 81, pp. 907-914, 1999.

[100] H. Hahn and W. Palich, "Preliminary evaluation of porous metal surfaced titanium for orthopedic implants," *Journal of biomedical materials research,* vol. 4, pp. 571-577, 1970.

[101] H. Ceylan, S. Kocabey, H. Unal Gulsuner, O. S. Balcik, M. O. Guler, and A. B. Tekinay, "Bone-like mineral nucleating peptide nanofibers induce differentiation of human mesenchymal stem cells into mature osteoblasts," *Biomacromolecules,* vol. 15, pp. 2407-18, Jul 14 2014.

[102] A. Mata, L. Hsu, R. Capito, C. Aparicio, K. Henrikson, and S. I. Stupp, "Micropatterning of bioactive self-assembling gels," *Soft Matter,* vol. 5, pp. 1228-1236, 2009.

[103] E. Groeneveld, J. Van Den Bergh, P. Holzmann, C. Ten Bruggenkate, D. Tuinzing, and E. Burger, "Mineralization processes in demineralized bone matrix grafts in human maxillary sinus floor elevations," *Journal of biomedical materials research,* vol. 48, pp. 393-402, 1999.

[104] S. E. Paramonov, H.-W. Jun, and J. D. Hartgerink, "Self-assembly of peptide-amphiphile nanofibers: the roles of hydrogen bonding and amphiphilic packing," *Journal of the American Chemical Society,* vol. 128, pp. 7291-7298, 2006.

[105] R. N. Shah, N. A. Shah, M. M. D. R. Lim, C. Hsieh, G. Nuber, and S. I. Stupp, "Supramolecular design of self-assembling nanofibers for cartilage regeneration," *Proceedings of the National Academy of Sciences,* vol. 107, pp. 3293-3298, 2010.
[106] M. J. Webber, J. Tongers, M.-A. Renault, J. G. Roncalli, D. W. Losordo, and S. I. Stupp, "Development of bioactive peptide amphiphiles for therapeutic cell delivery," *Acta biomaterialia,* vol. 6, pp. 3-11, 2010.
[107] H. Cui, M. J. Webber, and S. I. Stupp, "Self-assembly of peptide amphiphiles: From molecules to nanostructures to biomaterials," *Peptide Science,* vol. 94, pp. 1-18, 2010.
[108] A. Accardo, D. Tesauro, G. Mangiapia, C. Pedone, and G. Morelli, "Nanostructures by self-assembling peptide amphiphile as potential selective drug carriers," *Peptide Science,* vol. 88, pp. 115-121, 2007.
[109] E. Kokkoli, A. Mardilovich, A. Wedekind, E. L. Rexeisen, A. Garg, and J. A. Craig, "Self-assembly and applications of biomimetic and bioactive peptide-amphiphiles," *Soft Matter,* vol. 2, pp. 1015-1024, 2006.
[110] I. Hamley, "Self-assembly of amphiphilic peptides," *Soft Matter,* vol. 7, pp. 4122-4138, 2011.
[111] A. Trent, R. Marullo, B. Lin, M. Black, and M. Tirrell, "Structural properties of soluble peptide amphiphile micelles," *Soft Matter,* vol. 7, pp. 9572-9582, 2011.
[112] D. W. Löwik and J. C. van Hest, "Peptide based amphiphiles," *Chemical Society Reviews,* vol. 33, pp. 234-245, 2004.
[113] R. Pytela, M. D. Pierschbacher, S. Argraves, S. Suzuki, and E. Ruoslahti, "Arginine-glycine-aspartic acid adhesion receptors," *Methods Enzymol,* vol. 144, pp. 475-89, 1987.
[114] D. A. Puleo and R. Bizios, "RGDS tetrapeptide binds to osteoblasts and inhibits fibronectin-mediated adhesion," *Bone,* vol. 12, pp. 271-6, 1991.
[115] M. O. Guler, L. Hsu, S. Soukasene, D. A. Harrington, J. F. Hulvat, and S. I. Stupp, "Presentation of RGDS epitopes on self-assembled nanofibers of branched peptide amphiphiles," *Biomacromolecules,* vol. 7, pp. 1855-63, Jun 2006.
[116] G. M. Harbers and K. E. Healy, "The effect of ligand type and density on osteoblast adhesion, proliferation, and matrix mineralization," *J Biomed Mater Res A,* vol. 75, pp. 855-69, Dec 15 2005.
[117] J. M. Anderson, J. B. Vines, J. L. Patterson, H. Chen, A. Javed, and H. W. Jun, "Osteogenic differentiation of human mesenchymal stem cells synergistically enhanced by biomimetic peptide amphiphiles combined with conditioned medium," *Acta Biomater,* vol. 7, pp. 675-82, Feb 2011.
[118] J. M. Anderson, A. Andukuri, D. J. Lim, and H. W. Jun, "Modulating the gelation properties of self-assembling peptide amphiphiles," *ACS Nano,* vol. 3, pp. 3447-54, Nov 24 2009.
[119] F. Gelain, D. Bottai, A. Vescovi, and S. Zhang, "Designer self-assembling peptide nanofiber scaffolds for adult mouse neural stem cell 3-dimensional cultures," *PLoS One,* vol. 1, p. e119, 2006.
[120] M. J. Webber, J. Tongers, M. A. Renault, J. G. Roncalli, D. W. Losordo, and S. I. Stupp, "Development of bioactive peptide amphiphiles for therapeutic cell delivery," *Acta Biomater,* vol. 6, pp. 3-11, Jan 2010.
[121] A. Horii, X. Wang, F. Gelain, and S. Zhang, "Biological designer self-assembling peptide nanofiber scaffolds significantly enhance osteoblast proliferation, differentiation and 3-D migration," *PLoS One,* vol. 2, p. e190, 2007.
[122] H. Shin, S. Jo, and A. G. Mikos, "Biomimetic materials for tissue engineering," *Biomaterials,* vol. 24, pp. 4353-4364, 2003.

[123] K. C. Dee, T. T. Andersen, and R. Bizios, "Design and function of novel osteoblast-adhesive peptides for chemical modification of biomaterials," *Journal of biomedical materials research,* vol. 40, pp. 371-377, 1998.
[124] H. Ceylan, S. Kocabey, A. B. Tekinay, and M. O. Guler, "Surface-adhesive and osteogenic self-assembled peptide nanofibers for bioinspired functionalization of titanium surfaces," *Soft Matter,* vol. 8, pp. 3929-3937, 2012.
[125] G. Tansik, E. Kilic, M. Beter, B. Demiralp, G. K. Sendur, N. Can*, et al.*, "A glycosaminoglycan mimetic peptide nanofiber gel as an osteoinductive scaffold," *Biomaterials Science,* 2016.
[126] K. Chaudhury, V. Kumar, J. Kandasamy, and S. RoyChoudhury, "Regenerative nanomedicine: current perspectives and future directions," *International journal of nanomedicine,* vol. 9, p. 4153, 2014.
[127] K. S. Griffin, K. M. Davis, T. O. McKinley, J. O. Anglen, T.-M. G. Chu, J. D. Boerckel*, et al.*, "Evolution of Bone Grafting: Bone Grafts and Tissue Engineering Strategies for Vascularized Bone Regeneration," *Clinical Reviews in Bone and Mineral Metabolism,* pp. 1-13, 2015.
[128] C. J. Damien and J. R. Parsons, "Bone graft and bone graft substitutes: a review of current technology and applications," *Journal of Applied Biomaterials,* vol. 2, pp. 187-208, 1991.
[129] L. Zhang and T. J. Webster, "Nanotechnology and nanomaterials: promises for improved tissue regeneration," *Nano Today,* vol. 4, pp. 66-80, 2009.
[130] E. Arslan, I. C. Garip, G. Gulseren, A. B. Tekinay, and M. O. Guler, "Bioactive supramolecular peptide nanofibers for regenerative medicine," *Advanced healthcare materials,* vol. 3, pp. 1357-1376, 2014.
[131] J. B. Matson and S. I. Stupp, "Self-assembling peptide scaffolds for regenerative medicine," *Chemical Communications,* vol. 48, pp. 26-33, 2012.
[132] M. Sever, B. Mammadov, M. O. Guler, and A. B. Tekinay, "Tenascin-C mimetic peptide nanofibers direct stem cell differentiation to osteogenic lineage," *Biomacromolecules,* vol. 15, pp. 4480-4487, 2014.
[133] S. Ustun Yaylaci, M. Sardan Ekiz, E. Arslan, N. Can, E. Kilic, H. Ozkan*, et al.*, "Supramolecular GAG-like Self-Assembled Glycopeptide Nanofibers Induce Chondrogenesis and Cartilage Regeneration," *Biomacromolecules,* 2015.
[134] T. Webster and J. Ying, "Advances in chemical engineering," *Nanostructured materials. California, Estados Unidos: Academic Press,* 2001.
[135] B. Basu, D. S. Katti, and A. Kumar, *Advanced biomaterials: fundamentals, processing, and applications*: John Wiley & Sons, 2010.
[136] L. C. Palmer, C. J. Newcomb, S. R. Kaltz, E. D. Spoerke, and S. I. Stupp, "Biomimetic systems for hydroxyapatite mineralization inspired by bone and enamel," *Chemical reviews,* vol. 108, pp. 4754-4783, 2008.
[137] V. M. Mania, A. G. Kallivokas, C. Malavaki, A. P. Asimakopoulou, J. Kanakis, A. D. Theocharis*, et al.*, "A comparative biochemical analysis of glycosaminoglycans and proteoglycans in human orthotopic and heterotopic bone," *IUBMB life,* vol. 61, pp. 447-452, 2009.
[138] M. R. van der Harst, P. A. Brama, C. H. van de Lest, G. H. Kiers, J. DeGroot, and P. R. van Weeren, "An integral biochemical analysis of the main constituents of articular cartilage, subchondral and trabecular bone," *Osteoarthritis and cartilage,* vol. 12, pp. 752-761, 2004.
[139] C. W. Prince and J. M. Navia, "Glycosaminoglycan alterations in rat bone due to growth and fluorosis," *The Journal of nutrition,* vol. 113, pp. 1576-1582, 1983.

[140] J. Salbach, T. D. Rachner, M. Rauner, U. Hempel, U. Anderegg, S. Franz*, et al.*, "Regenerative potential of glycosaminoglycans for skin and bone," *Journal of molecular medicine,* vol. 90, pp. 625-635, 2012.
[141] J. Taipale and J. Keski-Oja, "Growth factors in the extracellular matrix," *The FASEB Journal,* vol. 11, pp. 51-59, 1997.
[142] D. S. Benoit and K. S. Anseth, "Heparin functionalized PEG gels that modulate protein adsorption for hMSC adhesion and differentiation," *Acta biomaterialia,* vol. 1, pp. 461-470, 2005.
[143] R. Mammadov, B. Mammadov, M. O. Guler, and A. B. Tekinay, "Growth factor binding on heparin mimetic peptide nanofibers," *Biomacromolecules,* vol. 13, pp. 3311-3319, 2012.
[144] S. Kocabey, H. Ceylan, A. B. Tekinay, and M. O. Guler, "Glycosaminoglycan mimetic peptide nanofibers promote mineralization by osteogenic cells," *Acta biomaterialia,* vol. 9, pp. 9075-9085, 2013.
[145] C. M. Kolf, E. Cho, and R. S. Tuan, "Biology of adult mesenchymal stem cells: regulation of niche, self-renewal and differentiation," *Arthritis res ther,* vol. 9, p. 204, 2007.
[146] E. Luong-Van, L. Grøndahl, S. Song, V. Nurcombe, and S. Cool, "The in vivo assessment of a novel scaffold containing heparan sulfate for tissue engineering with human mesenchymal stem cells," *Journal of molecular histology,* vol. 38, pp. 459-468, 2007.
[147] C. Dombrowski, S. J. Song, P. Chuan, X. Lim, E. Susanto, A. A. Sawyer*, et al.*, "Heparan sulfate mediates the proliferation and differentiation of rat mesenchymal stem cells," *Stem cells and development,* vol. 18, pp. 661-670, 2009.
[148] I. W. Fu, C. B. Markegard, B. K. Chu, and H. D. Nguyen, "Role of hydrophobicity on self-assembly by peptide amphiphiles via molecular dynamics simulations," *Langmuir,* vol. 30, pp. 7745-7754, 2014.
[149] G. Zandomeneghi, M. R. Krebs, M. G. McCammon, and M. Fändrich, "FTIR reveals structural differences between native β-sheet proteins and amyloid fibrils," *Protein science,* vol. 13, pp. 3314-3321, 2004.
[150] Y. Jiang, C. Li, X. Nguyen, S. Muzammil, E. Towers, J. Gabrielson*, et al.*, "Qualification of FTIR spectroscopic method for protein secondary structural analysis," *Journal of pharmaceutical sciences,* vol. 100, pp. 4631-4641, 2011.
[151] J. Kong and S. Yu, "Fourier transform infrared spectroscopic analysis of protein secondary structures," *Acta biochimica et biophysica Sinica,* vol. 39, pp. 549-559, 2007.
[152] E. Alt, Y. Yan, S. Gehmert, Y. H. Song, A. Altman, S. Gehmert*, et al.*, "Fibroblasts share mesenchymal phenotypes with stem cells, but lack their differentiation and colony-forming potential," *Biology of the Cell,* vol. 103, pp. 197-208, 2011.
[153] M. C. Vemuri, L. G. Chase, and M. S. Rao, *Mesenchymal stem cell assays and applications*: Springer, 2011.
[154] Z. Huang, E. R. Nelson, R. L. Smith, and S. B. Goodman, "The sequential expression profiles of growth factors from osteroprogenitors to osteoblasts in vitro," *Tissue engineering,* vol. 13, pp. 2311-2320, 2007.
[155] J. E. Aubin, "Regulation of osteoblast formation and function," *Reviews in Endocrine and Metabolic Disorders,* vol. 2, pp. 81-94, 2001.
[156] C. Hoemann, H. El-Gabalawy, and M. McKee, "In vitro osteogenesis assays: influence of the primary cell source on alkaline phosphatase activity and mineralization," *Pathologie Biologie,* vol. 57, pp. 318-323, 2009.

[157] C. A. Gregory, W. G. Gunn, A. Peister, and D. J. Prockop, "An Alizarin red-based assay of mineralization by adherent cells in culture: comparison with cetylpyridinium chloride extraction," *Analytical biochemistry,* vol. 329, pp. 77-84, 2004.
[158] E. Birmingham, G. Niebur, and P. McHugh, "Osteogenic differentiation of mesenchymal stem cells is regulated by osteocyte and osteoblast cells in a simplified bone niche," 2012.
[159] P. Ducy, T. Schinke, and G. Karsenty, "The osteoblast: a sophisticated fibroblast under central surveillance," *Science,* vol. 289, pp. 1501-1504, 2000.
[160] S. Viguet-Carrin, P. Garnero, and P. Delmas, "The role of collagen in bone strength," *Osteoporosis International,* vol. 17, pp. 319-336, 2006.
[161] L. D. Quarles, D. A. Yohay, L. W. Lever, R. Caton, and R. J. Wenstrup, "Distinct proliferative and differentiated stages of murine MC3T3-E1 cells in culture: An in vitro model of osteoblast development," *Journal of Bone and Mineral Research,* vol. 7, pp. 683-692, 1992.
[162] J. Sodek, B. Ganss, and M. McKee, "Osteopontin," *Critical Reviews in Oral Biology & Medicine,* vol. 11, pp. 279-303, 2000.
[163] E. E. Golub, "Role of matrix vesicles in biomineralization," *Biochimica et Biophysica Acta (BBA)-General Subjects,* vol. 1790, pp. 1592-1598, 2009.
[164] A. M. Ferreira, P. Gentile, V. Chiono, and G. Ciardelli, "Collagen for bone tissue regeneration," *Acta biomaterialia,* vol. 8, pp. 3191-3200, 2012.
[165] X. Wang, K. Harimoto, S. Xie, H. Cheng, J. Liu, and Z. Wang, "Matrix protein biglycan induces osteoblast differentiation through extracellular signal-regulated kinase and Smad pathways," *Biological and Pharmaceutical Bulletin,* vol. 33, pp. 1891-1897, 2010.
[166] Y. Li, S.-K. Chen, L. Li, L. Qin, X.-L. Wang, and Y.-X. Lai, "Bone defect animal models for testing efficacy of bone substitute biomaterials," *Journal of Orthopaedic Translation,* vol. 3, pp. 95-104, 2015.
[167] J. Lim, J. Lee, H.-S. Yun, H.-I. Shin, and E. K. Park, "Comparison of bone regeneration rate in flat and long bone defects: Calvarial and tibial bone," *Tissue Engineering and Regenerative Medicine,* vol. 10, pp. 336-340, 2013.
[168] C. Balçik, T. Tokdemir, A. Şenköylü, N. Koç, M. Timuçin, S. Akin*, et al.*, "Early weight bearing of porous HA/TCP (60/40) ceramics in vivo: a longitudinal study in a segmental bone defect model of rabbit," *Acta biomaterialia,* vol. 3, pp. 985-996, 2007.
[169] J. Neyt, J. A. Buckwalter, and N. Carroll, "Use of animal models in musculoskeletal research," *The Iowa orthopaedic journal,* vol. 18, p. 118, 1998.
[170] A. Schindeler, M. M. McDonald, P. Bokko, and D. G. Little, "Bone remodeling during fracture repair: The cellular picture," in *Seminars in cell & developmental biology*, 2008, pp. 459-466.
[171] P. Leong and E. Morgan, "Measurement of fracture callus material properties via nanoindentation," *Acta biomaterialia,* vol. 4, pp. 1569-1575, 2008.
[172] L. C. Gerstenfeld, D. M. Cullinane, G. L. Barnes, D. T. Graves, and T. A. Einhorn, "Fracture healing as a post-natal developmental process: Molecular, spatial, and temporal aspects of its regulation," *Journal of cellular biochemistry,* vol. 88, pp. 873-884, 2003.
[173] M. M. Deckers, R. L. van Bezooijen, G. van der Horst, J. Hoogendam, C. van der Bent, S. E. Papapoulos*, et al.*, "Bone morphogenetic proteins stimulate angiogenesis through osteoblast-derived vascular endothelial growth factor A," *Endocrinology,* vol. 143, pp. 1545-1553, 2002.

[174] A. Sawyer, S. Song, E. Susanto, P. Chuan, C. Lam, M. Woodruff*, et al.*, "The stimulation of healing within a rat calvarial defect by mPCL–TCP/collagen scaffolds loaded with rhBMP-2," *Biomaterials,* vol. 30, pp. 2479-2488, 2009.
[175] W. Hao, L. Pang, M. Jiang, R. Lv, Z. Xiong, and Y. Y. Hu, "Skeletal repair in rabbits using a novel biomimetic composite based on adipose-derived stem cells encapsulated in collagen I gel with PLGA-β-TCP scaffold," *Journal of Orthopaedic Research,* vol. 28, pp. 252-257, 2010.
[176] P. S. Mathieu and E. G. Loboa, "Cytoskeletal and focal adhesion influences on mesenchymal stem cell shape, mechanical properties, and differentiation down osteogenic, adipogenic, and chondrogenic pathways," *Tissue Engineering Part B: Reviews,* vol. 18, pp. 436-444, 2012.
[177] S. U. Yaylaci, M. Sen, O. Bulut, E. Arslan, M. O. Guler, and A. B. Tekinay, "Chondrogenic differentiation of mesenchymal stem cells on glycosaminoglycan-mimetic peptide nanofibers," *ACS Biomaterials Science & Engineering,* vol. 2, pp. 871-878, 2016.
[178] T. D. Schmittgen and K. J. Livak, "Analyzing real-time PCR data by the comparative CT method," *Nature protocols,* vol. 3, pp. 1101-1108, 2008.
[179] H. Ceylan, S. Kocabey, H. Unal Gulsuner, O. S. Balcik, M. O. Guler, and A. B. Tekinay, "Bone-like mineral nucleating peptide nanofibers induce differentiation of human mesenchymal stem cells into mature osteoblasts," *Biomacromolecules,* vol. 15, pp. 2407-2418, 2014.
[180] S. I. Stupp, J. J. Donners, G. A. Silva, H. A. Behanna, and S. G. Anthony, "Self-assembling peptide amphiphiles and related methods for growth factor delivery," ed: Google Patents, 2013.
[181] C. Ge, W. P. Cawthorn, Y. Li, G. Zhao, O. A. MacDougald, and R. T. Franceschi, "Reciprocal control of osteogenic and adipogenic differentiation by ERK/MAP kinase phosphorylation of Runx2 and PPARγ transcription factors," *Journal of cellular physiology,* vol. 231, pp. 587-596, 2016.
[182] F. Otto, A. P. Thornell, T. Crompton, A. Denzel, K. C. Gilmour, I. R. Rosewell*, et al.*, "Cbfa1, a candidate gene for cleidocranial dysplasia syndrome, is essential for osteoblast differentiation and bone development," *Cell,* vol. 89, pp. 765-771, 1997.
[183] E. Birmingham, G. Niebur, P. McHugh, G. Shaw, F. Barry, and L. McNamara, "Osteogenic differentiation of mesenchymal stem cells is regulated by osteocyte and osteoblast cells in a simplified bone niche," *European cells & materials,* vol. 23, p. 13, 2012.
[184] J. E. Aubin, "Advances in the osteoblast lineage," *Biochemistry and Cell Biology,* vol. 76, pp. 899-910, 1998.
[185] F. Nudelman and N. A. Sommerdijk, "Biomineralization as an inspiration for materials chemistry," *Angewandte Chemie International Edition,* vol. 51, pp. 6582-6596, 2012.
[186] K. Naka and H. Cölfen, *Biomineralization II: Mineralization Using Synthetic Polymers and Templates* vol. 2: Springer Science & Business Media, 2007.
[187] C. Carney, M. Fricke, S. Harry, H. Imai, R. Kniep, K. Sato*, et al.*, *Biomineralization I: Crystallization and Self-Organization Process* vol. 270: Springer, 2006.
[188] T. D. Sargeant, C. Aparicio, J. E. Goldberger, H. Cui, and S. I. Stupp, "Mineralization of peptide amphiphile nanofibers and its effect on the differentiation of human mesenchymal stem cells," *Acta biomaterialia,* vol. 8, pp. 2456-2465, 2012.
[189] J. D. Hartgerink, E. Beniash, and S. I. Stupp, "Self-assembly and mineralization of peptide-amphiphile nanofibers," *Science,* vol. 294, pp. 1684-1688, 2001.

[190] M. Gungormus, M. Branco, H. Fong, J. P. Schneider, C. Tamerler, and M. Sarikaya, "Self assembled bi-functional peptide hydrogels with biomineralization-directing peptides," *Biomaterials,* vol. 31, pp. 7266-7274, 2010.
[191] S. Hosseini, H. Naderi-Manesh, D. Mountassif, M. Cerruti, H. Vali, and S. Faghihi, "C-terminal amidation of an osteocalcin-derived peptide promotes hydroxyapatite crystallization," *Journal of Biological Chemistry,* vol. 288, pp. 7885-7893, 2013.
[192] H. Yuan, Z. Yang, Y. Li, X. Zhang, J. De Bruijn, and K. De Groot, "Osteoinduction by calcium phosphate biomaterials," *Journal of Materials Science: Materials in Medicine,* vol. 9, pp. 723-726, 1998.
[193] T. Mygind, M. Stiehler, A. Baatrup, H. Li, X. Zou, A. Flyvbjerg*, et al.*, "Mesenchymal stem cell ingrowth and differentiation on coralline hydroxyapatite scaffolds," *Biomaterials,* vol. 28, pp. 1036-1047, 2007.
[194] P. Müller, U. Bulnheim, A. Diener, F. Lüthen, M. Teller, E. D. Klinkenberg*, et al.*, "Calcium phosphate surfaces promote osteogenic differentiation of mesenchymal stem cells," *Journal of cellular and molecular medicine,* vol. 12, pp. 281-291, 2008.
[195] R. Z. LeGeros, "Calcium phosphate-based osteoinductive materials," *Chemical reviews,* vol. 108, pp. 4742-4753, 2008.
[196] J. Toquet, R. Rohanizadeh, J. Guicheux, S. Couillaud, N. Passuti, G. Daculsi*, et al.*, "Osteogenic potential in vitro of human bone marrow cells cultured on macroporous biphasic calcium phosphate ceramic," *Journal of biomedical materials research,* vol. 44, pp. 98-108, 1999.
[197] A. Phadke, Y. R. V. Shih, and S. Varghese, "Mineralized synthetic matrices as an instructive microenvironment for osteogenic differentiation of human mesenchymal stem cells," *Macromolecular bioscience,* vol. 12, pp. 1022-1032, 2012.
[198] S. Bhumiratana, W. L. Grayson, A. Castaneda, D. N. Rockwood, E. S. Gil, D. L. Kaplan*, et al.*, "Nucleation and growth of mineralized bone matrix on silk-hydroxyapatite composite scaffolds," *Biomaterials,* vol. 32, pp. 2812-2820, 2011.
[199] S. Choi and W. L. Murphy, "A screening approach reveals the influence of mineral coating morphology on human mesenchymal stem cell differentiation," *Biotechnology journal,* vol. 8, pp. 496-501, 2013.
[200] Y. C. Chai, S. J. Roberts, E. Desmet, G. Kerckhofs, N. van Gastel, L. Geris*, et al.*, "Mechanisms of ectopic bone formation by human osteoprogenitor cells on CaP biomaterial carriers," *Biomaterials,* vol. 33, pp. 3127-3142, 2012.
[201] G. K. Hunter, J. O'Young, B. Grohe, M. Karttunen, and H. A. Goldberg, "The flexible polyelectrolyte hypothesis of protein− biomineral interaction," *Langmuir,* vol. 26, pp. 18639-18646, 2010.
[202] J. P. Gorski, "Biomineralization of bone: a fresh view of the roles of non-collagenous proteins," *Frontiers in bioscience (Landmark edition),* vol. 16, p. 2598, 2011.
[203] L. Addadi and S. Weiner, "Control and design principles in biological mineralization," *Angewandte Chemie International Edition in English,* vol. 31, pp. 153-169, 1992.
[204] G. K. Hunter, P. V. Hauschka, R. A. POOLE, L. C. Rosenberg, and H. A. Goldberg, "Nucleation and inhibition of hydroxyapatite formation by mineralized tissue proteins," *Biochemical Journal,* vol. 317, pp. 59-64, 1996.
[205] S. Weiner and L. Addadi, "Design strategies in mineralized biological materials," *Journal of Materials Chemistry,* vol. 7, pp. 689-702, 1997.
[206] G. K. Hunter and H. A. Goldberg, "Modulation of crystal formation by bone phosphoproteins: role of glutamic acid-rich sequences in the nucleation of

hydroxyapatite by bone sialoprotein," *Biochemical Journal,* vol. 302, pp. 175-179, 1994.
[207] E. D. Spoerke, S. G. Anthony, and S. I. Stupp, "Enzyme directed templating of artificial bone mineral," *Advanced Materials,* vol. 21, pp. 425-430, 2009.
[208] W. Zhang, S. Liao, and F. Cui, "Hierarchical self-assembly of nano-fibrils in mineralized collagen," *Chemistry of Materials,* vol. 15, pp. 3221-3226, 2003.
[209] L. Ghasemi-Mobarakeh, M. P. Prabhakaran, L. Tian, E. Shamirzaei-Jeshvaghani, L. Dehghani, and S. Ramakrishna, "Structural properties of scaffolds: Crucial parameters towards stem cells differentiation," *World journal of stem cells,* vol. 7, p. 728, 2015.
[210] E. Czekanska, M. Stoddart, R. Richards, and J. Hayes, "In search of an osteoblast cell model for in vitro research," *Eur Cell Mater,* vol. 24, pp. 1-17, 2012.
[211] M. Marzia, N. A. Sims, S. Voit, S. Migliaccio, A. Taranta, S. Bernardini*, et al.*, "Decreased c-Src expression enhances osteoblast differentiation and bone formation," *The Journal of cell biology,* vol. 151, pp. 311-320, 2000.
[212] L. Gilbert, X. He, P. Farmer, J. Rubin, H. Drissi, A. J. Van Wijnen*, et al.*, "Expression of the osteoblast differentiation factor RUNX2 (Cbfa1/AML3/Pebp2αA) is inhibited by tumor necrosis factor-α," *Journal of Biological Chemistry,* vol. 277, pp. 2695-2701, 2002.
[213] F. Nudelman, A. J. Lausch, N. A. Sommerdijk, and E. D. Sone, "In vitro models of collagen biomineralization," *Journal of structural biology,* vol. 183, pp. 258-269, 2013.
[214] E. Villarreal-Ramirez, D. Eliezer, R. Garduño-Juarez, A. Gericke, J. M. Perez-Aguilar, and A. Boskey, "Phosphorylation regulates the secondary structure and function of dentin phosphoprotein peptides," *Bone,* vol. 95, pp. 65-75, 2017.
[215] A. S. Deshpande and E. Beniash, "Bioinspired synthesis of mineralized collagen fibrils," *Crystal Growth and Design,* vol. 8, pp. 3084-3090, 2008.
[216] M. Goldberg, A. B. Kulkarni, M. Young, and A. Boskey, "Dentin: Structure, Composition and Mineralization: The role of dentin ECM in dentin formation and mineralization," *Frontiers in bioscience (Elite edition),* vol. 3, p. 711, 2011.
[217] L. Fisher, D. Torchia, B. Fohr, M. Young, and N. Fedarko, "Flexible structures of SIBLING proteins, bone sialoprotein, and osteopontin," *Biochemical and biophysical research communications,* vol. 280, pp. 460-465, 2001.
[218] M. Prasad, W. T. Butler, and C. Qin, "Dentin sialophosphoprotein in biomineralization," *Connective tissue research,* vol. 51, pp. 404-417, 2010.
[219] C. Qin, J. Brunn, E. Cadena, A. Ridall, H. Tsujigiwa, H. Nagatsuka*, et al.*, "The expression of dentin sialophosphoprotein gene in bone," *Journal of Dental Research,* vol. 81, pp. 392-394, 2002.
[220] O. Baba, C. Qin, J. C. Brunn, J. E. Jones, J. N. Wygant, B. W. McIntyre*, et al.*, "Detection of dentin sialoprotein in rat periodontium," *European journal of oral sciences,* vol. 112, pp. 163-170, 2004.
[221] K. Alvares, Y. S. Kanwar, and A. Veis, "Expression and potential role of dentin phosphophoryn (DPP) in mouse embryonic tissues involved in epithelial–mesenchymal interactions and branching morphogenesis," *Developmental dynamics,* vol. 235, pp. 2980-2990, 2006.
[222] K. U. Ogbureke and L. W. Fisher, "SIBLING expression patterns in duct epithelia reflect the degree of metabolic activity," *Journal of Histochemistry & Cytochemistry,* vol. 55, pp. 403-409, 2007.

[223] S. Xiao, C. Yu, X. Chou, W. Yuan, Y. Wang, L. Bu*, et al.*, "Dentinogenesis imperfecta 1 with or without progressive hearing loss is associated with distinct mutations in DSPP," *Nature genetics,* vol. 27, pp. 201-204, 2001.
[224] X. Zhang, J. Zhao, C. Li, S. Gao, C. Qiu, P. Liu*, et al.*, "DSPP mutation in dentinogenesis imperfecta Shields type II," *Nature genetics,* vol. 27, 2001.
[225] T. Sreenath, T. Thyagarajan, B. Hall, G. Longenecker, R. D'Souza, S. Hong*, et al.*, "Dentin sialophosphoprotein knockout mouse teeth display widened predentin zone and develop defective dentin mineralization similar to human dentinogenesis imperfecta type III," *Journal of Biological Chemistry,* vol. 278, pp. 24874-24880, 2003.
[226] K. Verdelis, Y. Ling, T. Sreenath, N. Haruyama, M. MacDougall, M. C. van der Meulen*, et al.*, "DSPP effects on in vivo bone mineralization," *Bone,* vol. 43, pp. 983-990, 2008.
[227] Y. Yamakoshi, "Dentin sialophosphoprotein (DSPP) and dentin," *Journal of Oral Biosciences,* vol. 50, pp. 33-44, 2008.
[228] R. Fujisawa and M. Tamura, "Acidic bone matrix proteins and their roles in calcification," *Frontiers in bioscience (Landmark edition),* vol. 17, pp. 1891-1903, 2011.
[229] S. Suzuki, T. Sreenath, N. Haruyama, C. Honeycutt, A. Terse, A. Cho*, et al.*, "Dentin sialoprotein and dentin phosphoprotein have distinct roles in dentin mineralization," *Matrix Biology,* vol. 28, pp. 221-229, 2009.
[230] Y. Yamakoshi, J. C.-C. Hu, M. Fukae, H. Zhang, and J. P. Simmer, "Dentin Glycoprotein The Protein in the middle of the dentin sialophosphoprotein chimera," *Journal of Biological Chemistry,* vol. 280, pp. 17472-17479, 2005.
[231] M. ZANETTI, B. BERNARD, M. JONTELL, and A. LINDE, "Ca2+-Binding Studies of the Phosphoprotein from Rat-Incisor Dentine," *European Journal of Biochemistry,* vol. 113, pp. 541-545, 1981.
[232] M. E. Marsh, "Binding of calcium and phosphate ions to dentin phosphophoryn," *Biochemistry,* vol. 28, pp. 346-352, 1989.
[233] A. S. Deshpande, P.-A. Fang, X. Zhang, T. Jayaraman, C. Sfeir, and E. Beniash, "Primary structure and phosphorylation of dentin matrix protein 1 (DMP1) and dentin phosphophoryn (DPP) uniquely determine their role in biomineralization," *Biomacromolecules,* vol. 12, pp. 2933-2945, 2011.
[234] Y. S. Choi, J. Y. Lee, J. S. Suh, G. Lee, C. P. Chung, and Y. J. Park, "The mineralization inducing peptide derived from dentin sialophosphoprotein for bone regeneration," *Journal of Biomedical Materials Research Part A,* vol. 101, pp. 590-598, 2013.
[235] Y. Sun, Y. Lu, S. Chen, M. Prasad, X. Wang, Q. Zhu*, et al.*, "Key proteolytic cleavage site and full-length form of DSPP," *Journal of dental research,* vol. 89, pp. 498-503, 2010.
[236] A. Dey, P. H. Bomans, F. A. Müller, J. Will, P. M. Frederik, G. de With*, et al.*, "The role of prenucleation clusters in surface-induced calcium phosphate crystallization," *Nature materials,* vol. 9, pp. 1010-1014, 2010.
[237] W. Huang, S. Yang, J. Shao, and Y.-P. Li, "Signaling and transcriptional regulation in osteoblast commitment and differentiation," *Frontiers in bioscience: a journal and virtual library,* vol. 12, p. 3068, 2007.
[238] J. Feng, H. Huang, Y. Lu, L. Ye, Y. Xie, T. Tsutsui*, et al.*, "The Dentin matrix protein 1 (Dmp1) is specifically expressed in mineralized, but not soft, tissues during development," *Journal of dental research,* vol. 82, pp. 776-780, 2003.

[239] A. George, R. Silberstein, and A. Veis, "In situ hybridization shows Dmp1 (AG1) to be a developmentally regulated dentin-specific protein produced by mature odontoblasts," *Connective tissue research,* vol. 33, pp. 67-72, 1995.

[240] R. D'souza, A. Cavender, G. Sunavala, J. Alvarez, T. Ohshima, A. Kulkarni*, et al.*, "Gene expression patterns of murine dentin matrix protein 1 (Dmp1) and dentin sialophosphoprotein (DSPP) suggest distinct developmental functions in vivo," *Journal of Bone and Mineral Research,* vol. 12, pp. 2040-2049, 1997.